

國立臺灣大學理學院天文物理所  
博士論文

Department of Computer Science and Information Engineering  
College of Electrical Engineering and Computer Science  
National Taiwan University  
Doctoral Thesis

應用於狹義相對論性流體力學的保守量與原始量的新  
轉換法並實現於高速圖形顯示卡於自適性網格  
An adaptive mesh, GPU-accelerated, and error minimized  
special relativistic hydrodynamics code

曾柏勳

Po-Hsun Tseng

指導教授：闕志鴻 博士  
Advisor: Tzihong Chiueh, Ph.D.

中華民國 111 年 6 月

June, 2022



國立臺灣大學博士學位論文  
口試委員會審定書

應用於狹義相對論性流體力學的保守量與原始量  
的新轉換法並實現於高速圖形顯示卡於自適性網  
格

An adaptive mesh, GPU-accelerated, and error  
minimized special relativistic hydrodynamics code

本論文係曾柏勳君 (D05244001) 在國立臺灣大學天文物理所  
完成之博士學位論文，於民國 111 年 6 月 28 日承下列考試委員審  
查通過及口試及格，特此證明

口試委員：

---

---

---

---

---

---

---

---

所 長：

---

# 誌謝

感謝...



# **Acknowledgements**

I'm glad to thank . . .



# 摘要

本論文提出了一影像中使用者感興趣區域 (region of interest) 偵測之資料集 (benchmark)。使用者感興趣區域偵測在許多應用中極為有用，過去雖然有許多使用者感興趣區域之自動偵測演算法被提出，然而由於缺乏公開資料集，這些方法往往只測試了各自的小量資料而難以互相比較。從其它領域可以發現，基於公開資料集的可重製實驗與該領域突飛猛進密切相關，因此本論文填補了此領域之不足，我們提出名為「Photoshoot」的遊戲來蒐集人們對於感興趣區域的標記，並以這些標記來建立資料集。透過這個遊戲，我們已蒐集大量使用者對於感興趣區域的標記，並結合這些資料成為使用者感興趣區域模型。我們利用這些模型來量化評估五個使用者感興趣區域偵測演算法，此資料集也可更進一步作為基於學習理論演算法的測試資料，因此使基於學習理論的偵測演算法成為可能。

**關鍵字：** 相對論性流體演算法、費米氣泡、義羅西塔氣泡



# Abstract

We present a new special relativistic hydrodynamics (SRHD) code capable of handling coexisting ultra-relativistically hot and non-relativistically cold gases. We achieve this by designing a new algorithm for conversion between primitive and conserved variables in the SRHD solver, which incorporates a realistic ideal-gas equation of state covering both the relativistic and non-relativistic regimes. The code can handle problems involving a Lorentz factor as high as  $10^6$  and optimally avoid the catastrophic cancellation. In addition, we have integrated this new SRHD solver into the code `GAMER` (<https://github.com/gamer-project/gamer>) to support adaptive mesh refinement and hybrid OpenMP/MPI/GPU parallelization. It achieves a peak performance of  $7 \times 10^7$  cell updates per second on a single Tesla P100 GPU and scales well to 2048 GPUs. We apply this code to two interesting astrophysical applications: (a) an asymmetric explosion source on the relativistic blast wave and (b) the flow acceleration and limb-brightening of relativistic jets.

**Keywords:** relativistic jets, numerical method



# Contents

口試委員會審定書	iii
誌謝	v
Acknowledgements	vii
摘要	ix
Abstract	xi
<b>1 Introduction</b>	<b>1</b>
<b>Part I</b>	<b>3</b>
<b>2 Special relativistic hydrodynamics</b>	<b>5</b>
2.1 Relativistic hydrodynamics . . . . .	5
2.2 Equations of state . . . . .	7
2.3 Conversion between primitive and conserved variables . . . . .	10
<b>3 Numerical methods</b>	<b>15</b>
3.1 A GAMER Primer . . . . .	15
3.2 Flexible Time-step . . . . .	16
3.3 Handling unphysical results . . . . .	18
<b>4 Test problems</b>	<b>21</b>
4.1 Convergence test for sinusoidal waves . . . . .	21

4.2	1-D relativistic Riemann problems . . . . .	22
4.3	Ultra-relativistic limit . . . . .	24
4.4	Mixed limits . . . . .	26
4.5	Multi-dimensional grid effects for high- $\mathcal{M}$ flows . . . . .	28
<b>5</b>	<b>Performance scaling</b>	<b>33</b>
<b>6</b>	<b>Astrophysical applications</b>	<b>37</b>
6.1	Triaxial blast wave . . . . .	37
6.2	Limb-brightened jet . . . . .	38
<b>7</b>	<b>Conclusions for part 1</b>	<b>43</b>
<b>8</b>	<b>Appendix</b>	<b>45</b>
8.1	Initial guess for Newton-Raphson iteration . . . . .	45
8.2	Numerical error analysis for root-finding . . . . .	46
8.3	Exact solutions of relativistic Riemann problems with the TM equation of state . . . . .	49
<b>Part II</b>		<b>53</b>
<b>9</b>	<b>Brief review of the <i>Fermi</i>/eROSITA bubbles</b>	<b>55</b>
<b>10</b>	<b>Methodology</b>	<b>57</b>
10.1	The Galactic and Disk Models . . . . .	59
10.2	The Clumpy Multiphase Interstellar Medium . . . . .	62
10.3	Oblique jets . . . . .	65
<b>11</b>	<b>Results</b>	<b>67</b>
11.1	Morphology and properties of Galactic bubbles . . . . .	67
11.2	Morphology and Profiles in X-ray . . . . .	69
11.3	Gamma-ray and microwave spectra: constraint on the CRe spectral index .	72
<b>12</b>	<b>Discussion</b>	<b>81</b>

<b>13 Conclusions for part 2</b>	<b>83</b>
<b>14 Appendix for part 2</b>	<b>85</b>
<b>Bibliography</b>	<b>87</b>



# List of Figures

- 4.1 Convergence test for sinusoidal waves. The L1 errors of the new scheme in both the high- $T$  limit (yellow squares) and low- $T$  limit (blue pluses) decrease as  $N^{-2}$ , consistent with the second-order accuracy of the MUSCL-Hancock scheme with PLM data reconstruction. However, the L1 error of the original scheme in the low- $T$  limit (brown circles) is much larger and roughly equal to a constant of  $2 \times 10^{-6}$ . This is expected because the error in the original scheme can be estimated from Equation (4.2). For the original scheme in the opposite high- $T$  limit (darkred diamond), the discretization error, however, completely overwhelms the error ( $\sim 4 \times 10^{-16}$ ) estimated from Equation (2.21) in the high- $T$  limit when  $\gamma \sim 1$ , thus dominating the L1 error.

- 4.2 Riemann problem in the UR limit with a head-on collision of two identical gases with  $\beta\gamma = 10^6$  and  $k_B T / mc^2 = 10^5$  at  $t = 1.0$ . The left column shows the entire simulation domain, while the right column shows the zoom-in image of the post-shock region. From top to bottom: pressure, proper mass density, four-velocity, and temperature. Note that we plot the Mach number in the zoom-in image (right column) of four-velocity so as to readily compare the amplitude of velocity oscillation with sound speed. The new scheme (blue circles) fully agrees with the original scheme (olive crosses) not only on the large-scale profiles but also on the small-scale errors, meaning that the new scheme (blue circles) does not sacrifice (or improve) the numerical accuracy in the UR limit for that in the NR limit. . 25

4.3 Riemann problem in the mixed UR and NR limits at  $t = 80$ . The second row in Table 4.1 shows the initial condition. Clock-wise from top-left: pressure, 4-velocity, temperature, and proper mass density. We find not only that the shock front at  $x = 26$  is well resolved by 3–4 cells but also that the new scheme (red crosses) agrees well with the exact solution of the TM EoS (yellow lines), as shown in all insets. The L1 error of the density profile from the original scheme (black circles) is 23 per cent within the region between the head of rarefaction wave and initial discontinuity (i.e.  $2.67 \times 10^{-2} < x < 5 \times 10^{-2}$ ), consistent with the 20 per cent error estimated by Equation (4.2) with  $k_B T/mc^2 = 8 \times 10^{-6}$ . However, in the region  $5 \times 10^{-2} < x < 0.3$  swept by the right-traveling contact discontinuity, errors of the original scheme are much larger than the estimate, which requires further investigation. The TM profiles match well with both the  $\Gamma = 5/3$  profiles (blue dashed lines) in the NR region ( $x < 0.21$ ) and the  $\Gamma = 4/3$  profiles (green dashed lines) in the UR region ( $x > 0.27$ ). . . . . 27

4.4 Ultra-relativistic flows propagating along different spatial directions with respect to the grids. In all subsrhd-figures (a)–(d), the left and right columns are the longitudinal and transverse slices, respectively. Longitudinal slices are taken through the flow source while the transverse slices are taken through the label ‘A’. The flow diameter is resolved by 28 cells in (a) and (b) and by 56 cells in (c) and (d). The flow has an extremely high Mach number ( $\mathcal{M} \sim 10^6$ ) leaving any instability short of time to develop, and one expects a smooth flow-ambient interface. However, the fuzzy-looking cross-sections in the transverse slices of the oblique flow (right columns in (b) and (d)) suggest that the high-speed flow induces false instability when the flow travels obliquely across Cartesian grids. Increasing the spatial and temporal resolution does not help the numerical solution of an oblique flow to converge to that of a parallel flow. . . . . 30

4.5	Close-up view of the rectangular region in Figure 4.4(c) with longitudinal (first column from the left) and transverse (other columns) slices passing through ‘B’ and ‘C’, respectively. Compared with Figure 4.4(c), it clearly shows that the finger pattern consists of 2-D flat sheets along the flow. . . . .	31
5.1	Temperature slice through the centre of blast waves at $t = 0.5L/c$ , with the grid patches overlaid in the case of 8 nodes in the weak scaling test. . . . .	34
5.2	Strong scaling of the relativistic jet simulation with five AMR levels and 16–2048 GPU nodes (left panel: cell updates per second; right panel: parallel efficiency). The maximum total number of cells, excluding ghost cells, is $7.9 \times 10^9$ . The deviation from the ideal scaling is mainly due to MPI communication, the time fraction of which increases by a factor of 10 when increasing the number of nodes from 64 to 2048. . . . .	35
5.3	Weak scaling of the multi-blast waves simulation with three AMR levels and 1–2048 GPU nodes (left panel: cell updates per second; right panel: parallel efficiency). The maximum total number of cells, excluding ghost cells, is $6.9 \times 10^7$ per node. The parallel efficiency drops from 0.90 to 0.78 when $N_{\text{node}}$ increases from 64 to 2048 mainly because the MPI communication time fraction increases from 10.3 to 18.8 per cent. . . . .	36
6.1	Triaxial blast wave test. The middle ( $t = 0.05L/c$ ) and right ( $t = 0.3L/c$ ) columns show the slices passing through the triaxial source at the mid-plane of its intermediate axis (i.e. the horizontal and vertical axes are along the major and minor axes, respectively). The left column shows the profiles along the minor-axis (i.e. the white dotted-dashed line in the $\gamma$ map). . . . .	39
6.2	Damping of the triaxiality in the triaxial blast wave test, where $R_L$ and $R_S$ are the radii of the triaxial blast wave along the semi-major ( $r_L$ ) and semi-minor axes ( $r_S$ ) of the initial source. . . . .	40



10.2 The volume filling factor as a function of initial number density within the disk without the jet source. The vertical bands from left to right depict the allowable number densities (Ferrière, 2001) for hot ionized, warm neutral (WNM), warm ionized (WIM), cold neutral mediums (CNM), and molecular clouds. . . . .	63
10.3 Close-up view of the initial pressure (top), temperature (middle), and number density (bottom) slices in the $y - z$ plane through the center of the disk. . . . .	64
11.1 . . . . .	70
11.2 . . . . .	70
11.3 . . . . .	70
11.4 . . . . .	70
11.5 The slices of pressure (top), temperature (middle), and number density (bottom) at the end of simulation $t = 12.39$ Myr. The slices pass through a bipolar jet source injecting along $z = -y$ direction for a duration $t = 0 - 1.2$ Myr. Comparison between the clumpy (Fig. 11.1) and the smooth disks (Fig. 11.2) in a stratified atmosphere shows that the initial density distribution of the dense disk has an insignificant effect on the overall dynamics of bubbles. However, the outermost bubbles arising from the smooth disk in an uniform atmosphere (Fig. 11.3) is nearly spherical, suggesting that the stratification facilitates the elongation of the outermost bubbles significantly. Fig. 11.3 and 11.4 reveal that the development of the innermost bubbles is always associated with the disk. Also, without the disk (Fig. 11.4), the outermost bubbles and the turbulent plasma would be oblique, indicating that the dense disk is crucial for the production of symmetric Galactic bubbles. . . . .	70

11.6 Left: the profiles of pressure (top), temperature (middle), and number density (bottom) along the positive $z$ -axis in Fig. 11.5. Right: the close-up view of the profiles in the yellow band. The sharp pressure jump at $z = 3.62$ kpc indicates that the innermost bubbles (dashed box in the top panel in Fig. 11.1) are an expanding reverse shock. . . . .	71
11.7 Zoom-in images of the density (left) and pressure (right) slices of the innermost bubbles. The high density upstream of the reverse shock requires an even higher density downstream. Continuing outward, the higher density must match with low density further downstream; thus there exists a dense shell (the turbulent region outside the black dashed line in the left panel). . . . .	71
11.8 Simulated (top) and observed (bottom; Predehl et al. 2020) count rate (photons $s^{-1}$ $deg^{-2}$ ) in the 0.6–1.0 keV range. Throughout this paper we show sky maps in Galactic coordinates centered on the Galactic center using a Hammer-Aitoff projection. The red arrow at the center of the top panel depicts the direction of the bipolar jets, constantly ejecting at an angle of $45^\circ$ to the disk normal for the first 1.2 Myr. . . . .	73
11.9 Comparison of the simulated (red) and observed (black; Predehl et al. 2020) one-dimensional photon count-rate profiles in the same energy band as in Fig. 11.8, cut at various Galactic latitudes (as labelled). . . . .	73
11.10 . . . . .	73

11.11 Simulated microwave spectra (colored lines in left) averaged over  $20^\circ < |b| < 30^\circ$ ,  $|l| < 10^\circ$ . The data point represents the *WMAP* data in the 23 GHz K band and the shaded bow-tie area indicates the range of synchrotron spectral indices allowed for the *WMAP* haze (Dobler & Finkbeiner, 2008). Simulated gamma-ray spectra (colored lines in right column) of the *Fermi* bubbles calculated for a longitude range of  $|l| < 10^\circ$  for different latitude bins. The gray band represents the observational data of Ackermann et al. (2014). The row from top to bottom shows the microwave (left) and gamma-ray (right) spectra with CRe spectral index 2.2, 2.4 and 2.6, respectively. The CRe cutoff energy is 562.1 GeV in all cases. . . . . 77

11.12 The observed (left; Selig et al. 2015) and simulated (right) photon flux in the energy bin 76.8 – 153.6 GeV. Note that the left panel is the photon flux of the diffuse component reconstructed by the D<sup>3</sup>PO algorithm (Selig et al., 2015) that analyzes the photon data from the *Fermi* Large Area Telescope (Atwood et al., 2009) and removes the contribution from point-like component. The red arrow at the center of the right panel depicts the direction of the bipolar jet, constantly ejecting at an angle of  $45^\circ$  to the disk normal in 1.2 Myr. . . . . 78

11.13 The CR pressure slice passing through the jet source at 12.39 Myr. Comparison between gas pressure (Fig. 11.5) and cosmic ray pressure shows that the CR pressure is around  $5 \times 10^{-15}$ – $8 \times 10^{-15}$  erg/cm<sup>3</sup>, bringing the CR-to-gas pressure ratio is 0.1–0.2, similar to 0.18 at the beginning of the simulation. We therefore stress that ignoring the contribution of CR pressure gradient to the momentum of the gas in Eq. 10.1 is reasonable. . . 79

14.1 Simulation results based on the jets parameters in Table. 14.1. . . . . 86

# List of Tables

4.1 The left and right initial states of the Riemann problems in Section 4.2. We denote the left/right states by the subscript $L/R$ .	24
8.1 Exact solution of a relativistic Riemann problem with the TM EoS at $t = 80.0$ . Columns from left to right give $x$ -coordinate, proper mass density, four-velocity, and pressure. The initial condition is given in the last row of Table 4.1, with the initial discontinuity at $x = 5 \times 10^{-2}$ . The blue solid line in Figure 4.3 plots the solution. The exact solution is calculated with double precision and shown in 16 digits to reach machine accuracy. The data are available in the supplement.	52
10.1 Parameters of the disk, atmosphere, and gravitational potential in the simulations.	63
14.1 The list of runs showing different injected jet parameters. The fiducial run (C) has been pointed out by an asterisk in the list.	86



# Chapter 1

## Introduction

Many high energy astrophysical problems involve relativistic flows. The problems include, for example, collimated jets in active galactic nuclei (AGN) (Chiueh et al. 1991; Li et al. 1992; Blandford et al. 2019), collapsar models of long-duration gamma-ray bursts (Woosley, 1993), magnetized relativistic winds and nebulae from pulsars (Kennel & Coroniti 1984a; Kennel & Coroniti 1984b; Chiueh 1989; Chiueh et al. 1998), and mildly relativistic wide-angle outflows in neutron star mergers (Mooley et al. 2018b; Mooley et al. 2018a; Ghirlanda et al. 2019; Fong et al. 2019). The full scope of these problems generally involves substantial temperature changes between jets (winds) and ambient gases. For this reason, the pioneering works of Taub (1948), Mathews (1971), and Mignone et al. (2005) suggested Taub-Mathews equation of state (TM EoS) that approximates the exact EoS (Synge, 1957) for ultra-relativistically hot (high- $T$  hereafter) gases coexisting with non-relativistically cold (low- $T$  hereafter) gases.

In addition, Noble et al. (2006) first compared the accuracy of several schemes for recovering primitive variables in the Riemann problems by means of self-checking tests (see Appendix 8.2 for details). Mignone & McKinney (2007) further proposed an inversion scheme for an arbitrary EoS and suggested that directly evolving the reduced energy density (i.e. the energy density subtracting the rest mass energy density from the total energy density) can avoid catastrophic cancellation in the non-relativistic limit. However, very few studies have systematically investigated how serious the catastrophic cancellation bears upon simulation results. This is partially due to the lack of exact solutions with which

numerical results can be compared.

In this paper, we propose a new numerical scheme for conversion between primitive and conserved variables in the presence of both high- $T$  and low- $T$  gases. The new scheme is carefully tailored to avoid catastrophic cancellation. To verify its accuracy, we numerically derive the exact solutions of two relativistic Riemann problems with the TM EoS and compare with the simulation results. It demonstrates that our new special relativistic hydrodynamics (SRHD) code can minimize numerical errors compared with conventional methods.

We have integrated this new SRHD solver into the code `GAMER` (Schive et al. 2010; Schive et al. 2018) to facilitate GPU acceleration and adaptive mesh refinement (AMR). This new code, `GAMER-SR`, yields good weak and strong scalings using up to 2048 GPUs on `Piz-Daint`, the supercomputer at the Swiss National Supercomputing Centre (CSCS). Finally, we present two astrophysical applications, an asymmetric explosion and self-accelerating jets, to demonstrate the capability of this new code in extreme conditions. All simulation data are analysed and visualized using the package `yt` (Turk et al., 2011).

This paper is organized as follows. We introduce the equation of state and our new scheme for conversion between primitive and conserved variables in Chapter 2. In Chapter 3, we describe numerical methods, including the AMR structure, GPU acceleration, flexible time-steps, and correction of unphysical results. In Chapter 4 and 5, we conduct numerical experiments to demonstrate the accuracy in both the non-relativistic (NR) and ultra-relativistic (UR) limits, the performance scalability, as well as the limitation of `GAMER-SR`. Finally, we present two astrophysical applications in Chapter 6 and draw the conclusion in Chapter 7.

Note that the speed of light and the Boltzmann constant are hard-coded to 1 in `GAMER-SR`. However, these physical constants are retained in this paper, except in Appendices, for dimensional consistency.

# **Part I**

## Special relativistic hydrodynamics



# Chapter 2

## Special relativistic hydrodynamics

### 2.1 Relativistic hydrodynamics

Mass and energy-momentum conservation laws of a special relativistic ideal fluid follow

$$\partial_\nu (\rho U^\nu) = 0, \quad (2.1a)$$

$$\partial_\nu T^{\mu\nu} = 0, \quad (2.1b)$$

where

$$T^{\mu\nu} = \rho h U^\mu U^\nu / c^2 + p \eta^{\mu\nu}. \quad (2.2)$$

$\rho$  and  $p$  are the proper mass density and the pressure,  $U^\mu$  the four-velocity,  $\eta^{\mu\nu}$  the metric tensor of Minkowski space, and  $c$  the speed of light.  $h$  is the specific enthalpy, related to the specific thermal energy  $\epsilon$  by

$$h = c^2 + \epsilon + \frac{p}{\rho}. \quad (2.3)$$

An equation of state,  $h(\rho, p)$ , is required to close Equation (2.1) and will be discussed in Section 2.2. Throughout this paper, lower-case Greek indices run from 0 to 3, Latin ones from 1 to 3, and the Einstein summation convention is used, except when stated otherwise.

Equation (2.1) can be rewritten into a convenient conservative form for numerical

integration:

$$\partial_t D + \partial_j (D U^j / \gamma) = 0, \quad (2.4a)$$

$$\partial_t M^i + \partial_j (M^i U^j / \gamma + p \delta^{ij}) = 0, \quad (2.4b)$$

$$\partial_t E + \partial_j (M^j c^2) = 0, \quad (2.4c)$$

where  $\gamma$  is the Lorentz factor, and  $\delta^{ij}$  is the Kronecker delta notation.

The five conserved quantities  $D$ ,  $M^i$ , and  $E$  are the mass density, the momentum densities, and the total energy density, respectively. All conserved variables are related to primitive variables  $(\rho, U^i, p)$  through

$$D = \rho \gamma, \quad (2.5a)$$

$$M^i = D h U^i / c^2, \quad (2.5b)$$

$$E = D h \gamma - p. \quad (2.5c)$$

Nevertheless, Mignone & McKinney (2007) suggest evolving the reduced energy density,

$$\tilde{E} := E - D c^2, \quad (2.6)$$

instead of the total energy density; otherwise, extraction of a tiny thermal energy for a cold gas from the total energy will lead to catastrophic cancellation. An intuitive approach is to subtract Equation (10.1a) from Equation (10.1c) so that we can obtain a new energy equation. However, the new energy flux,  $(M^j - D U^j / \gamma) c^2$ , also suffers from catastrophic cancellation in the NR limit. An appropriate new energy flux avoiding such a problem is  $(\tilde{E} + p) U^j / \gamma$ , which is mathematically equivalent to  $(M^j - D U^j / \gamma) c^2$ . The reduced energy equation for numerical integration can thus be cast into

$$\partial_t \tilde{E} + \partial_j [(\tilde{E} + p) U^j / \gamma] = 0, \quad (2.7)$$

which is to replace Equation (10.1c).

Moreover, solving the Lorentz factor  $\gamma$  as three-velocity ( $v = \sqrt{v^i v_i}$ ) approaches  $c$  can seriously suffer from catastrophic cancellation when using  $\gamma = 1/\sqrt{1 - v^i v_i/c^2}$ . Therefore, we explicitly adopt four-velocities ( $U^i$ ) instead of three-velocity ( $v^i$ ) for numerical computations and solve the Lorentz factor in terms of four-velocities as

$$\gamma = \sqrt{1 + U^i U_i / c^2}, \quad (2.8)$$

by which significant digits in  $\gamma$  can be kept when  $\gamma \gg 1$ .

In addition, unlike the three-velocity bounded by  $c$ , four-velocity  $U^i$  has no upper limit and therefore can greatly reduce the risk of having  $v > c$  due to numerical errors.

## 2.2 Equations of state

GAMER-SR supports two kinds of EoS, the Taub-Mathews EoS (TM; Taub 1948, Mathews 1971, Mignone et al. 2005) and the polytropic EoS with a constant ratio of specific heats  $\Gamma$ . Assuming an ideal fluid in local thermal equilibrium and obeying the non-degenerate Maxwell-Jüttner statistics (Jüttner, 1911), the exact EoS (Synge, 1957) derived from the kinetic theory of relativistic gases is given by

$$\frac{h_{\text{exact}}}{c^2} = \frac{K_3 (mc^2/k_B T)}{K_2 (mc^2/k_B T)}, \quad (2.9)$$

where  $k_B$  and  $T$  are the Boltzmann constant and temperature, respectively, and  $K_n$  the  $n$ -th order modified Bessel function of the second kind. However, direct use of Equation (2.9) is computationally inefficient because the evaluation of Bessel function is numerically expensive.

Alternatively, the TM EoS is an approximation of Equation (2.9) and given by

$$\frac{h_{\text{TM}}}{c^2} = 2.5 \left( \frac{k_B T}{mc^2} \right) + \sqrt{2.25 \left( \frac{k_B T}{mc^2} \right)^2 + 1}. \quad (2.10)$$

The effective  $\Gamma$  can be found by equating Equation (2.9) or Equation (2.10) to the

polytropic EoS,

$$\frac{h_\Gamma}{c^2} = 1 + \frac{\Gamma}{\Gamma - 1} \left( \frac{k_B T}{mc^2} \right), \quad (2.11)$$

and solving  $\Gamma$  for the exact or TM EoS, respectively. As depicted in Figure 2.1, the maximum relative errors  $1 - \Gamma_{\text{TM}}/\Gamma_{\text{exact}}$  and  $1 - \tilde{h}_{\text{TM}}/\tilde{h}_{\text{exact}}$  are found to be only 1.9 and 2.0 per cent, respectively. In addition, Equation (2.10) approaches Equation (2.9) in both high- and low- $T$  limits. Detailed comparisons between Equation (2.9) and Equation (2.10) have been presented previously (Mignone et al. 2005; Ryu et al. 2006; Mignone & McKinney 2007) and we do not repeat here.

On the other hand, the polytropic EoS has the advantage of simplicity and therefore has been used in many SRHD codes, such as `FLASH` (Fryxell et al., 2000), `CAFE` (Lora-Clavijo et al., 2015), and `XTREEM-FV` (Núñez-de la Rosa & Munz, 2016). However, the polytropic EoS cannot handle the case where relativistic gases and non-relativistic gases coexist, primarily because the ratio of specific heats depends sensitively on temperature when  $k_B T \sim mc^2$  (see the upper left panel in Figure 2.1). Moreover, the polytropic EoS with a non-relativistic  $\Gamma = 5/3$  and a relativistic  $\Gamma = 4/3$  does not satisfy the Taub's fundamental inequality for ideal gases (Taub, 1948)

$$\left[ \frac{h}{c^2} - \left( \frac{k_B T}{mc^2} \right) \right] \left[ \frac{h}{c^2} - 4 \left( \frac{k_B T}{mc^2} \right) \right] \geq 1, \quad (2.12)$$

implying that  $\Gamma$  must lie between 4/3 and 5/3 for any positive and finite value of temperature. Although the polytropic EoS is physically incorrect, we still reserve this feature in GAMER-SR for fast computation of a pure non-relativistic or relativistic gas.

The other two important quantities are the Mach number ( $\mathcal{M}$ ) and the sound speed ( $c_s$ ), given by

$$\mathcal{M} = \frac{\sqrt{U^i U_i}}{U_s}, \quad (2.13)$$

and

$$\frac{c_s}{c} = \sqrt{\frac{k_B T / mc^2}{3h/c^2} \left( \frac{5h/c^2 - 8k_B T / mc^2}{h/c^2 - k_B T / mc^2} \right)}, \quad (2.14)$$

for the TM EoS, where  $U_s = c_s / \sqrt{1 - (c_s/c)^2}$ . The sound speed approaches  $c/\sqrt{3}$  at

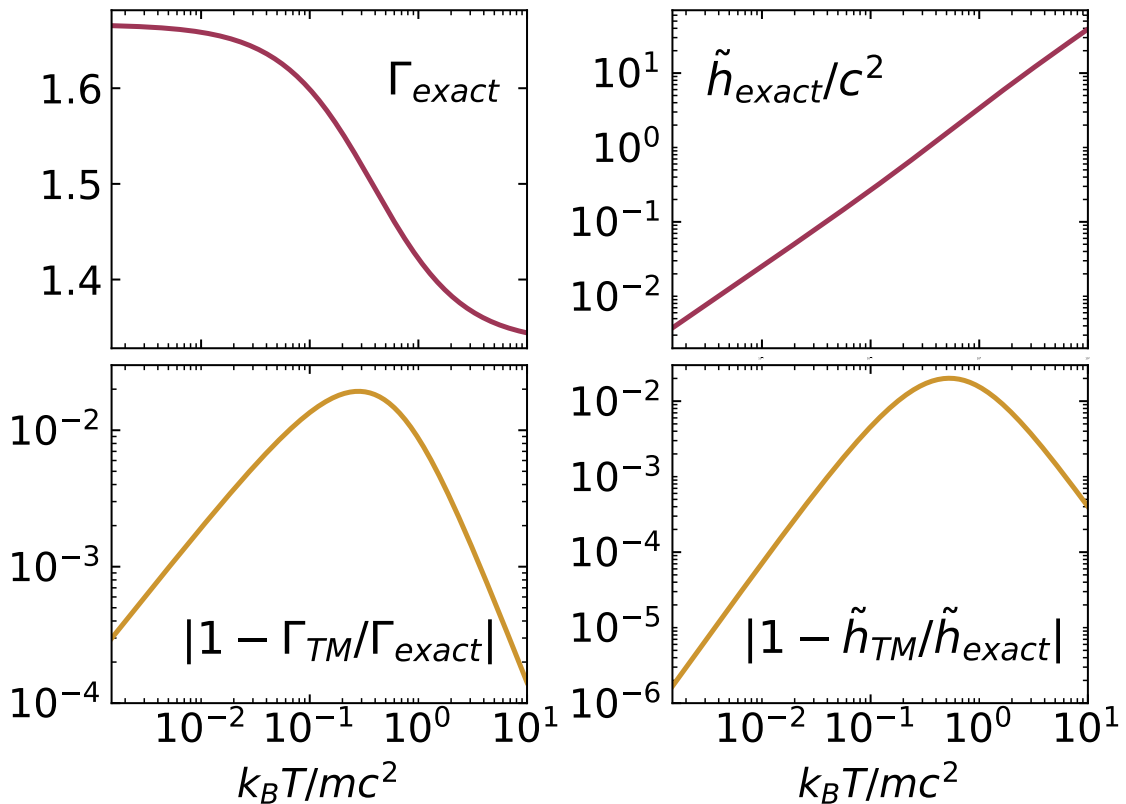


Figure 2.1: The effective adiabatic index  $\Gamma$  (top left), the reduced enthalpy  $\tilde{h}/c^2 := h/c^2 - 1$  (top right) as a function of temperature. Bottom panels show that Equation (2.10) approaches Equation (2.9) in both high- and low- $T$  limits, where the maximum relative errors  $1 - \Gamma_{TM}/\Gamma_{exact}$  and  $1 - \tilde{h}_{TM}/\tilde{h}_{exact}$ , are only 1.9 and 2.0 per cent, respectively.

ultra-relativistic temperature and will be used in the Riemann solver.

## 2.3 Conversion between primitive and conserved variables

In standard Riemann-type numerical schemes, conversion between conserved and primitive variables is a common procedure for data reconstructions and flux computations. For non-relativistic hydrodynamics, this conversion can be carried out in a straightforward and analytical manner. However, designing an accurate and efficient conversion algorithm for a relativistic problem in the presence of NR gases, which involves root-finding, is challenging. This is because catastrophic cancellations may arise in the non-relativistic gas.

Here we propose a new conversion scheme to solve this problem based on the TM EoS. The reduced energy density (Equation 2.6) and the momentum density (Equation 2.5b) satisfy the relation

$$\begin{aligned} & \left( \frac{\tilde{E}}{Dc^2} \right)^2 + 2 \left( \frac{\tilde{E}}{Dc^2} \right) - \left( \frac{\mathbf{M}}{Dc} \right)^2 \\ &= \frac{\tilde{h}^2}{c^4} + \frac{2\tilde{h}}{c^2} - 2 \left( \frac{k_B T}{mc^2} \right) \left( \frac{\tilde{h}}{c^2} + 1 \right) + \frac{(k_B T/mc^2)^2 (\tilde{h} + c^2)^2}{(\tilde{h} + c^2)^2 + \left( \frac{\mathbf{M}c}{D} \right)^2} \\ &:= f(\tilde{h}), \end{aligned} \quad (2.15)$$

where  $f$  is positive definite,  $\tilde{h} := h - c^2$  is the reduced enthalpy, and the temperature  $k_B T/mc^2$  is related to  $\tilde{h}$  by inverting Equation (2.10):

$$\frac{k_B T}{mc^2} = \frac{2(\tilde{h}/c^2)^2 + 4(\tilde{h}/c^2)}{5(\tilde{h}/c^2) + 5 + \sqrt{9(\tilde{h}/c^2)^2 + 18(\tilde{h}/c^2) + 25}}. \quad (2.16)$$

The conserved variables  $\tilde{E}$ ,  $M^j$ , and  $D$  on the left-hand side are known quantities updated at every time step, from which one can solve for  $\tilde{h}$ .

We adopt  $\tilde{h} = h - c^2$  instead of  $h$  as the root because the latter is dominated by rest mass energy density in the low- $T$  limit and thus will suffer from catastrophic cancellation when numerically extracting temperature from trailing digits.

Equation (2.15) is suitable for the Newton-Raphson iteration method as it is a monotonically increasing function of  $\tilde{h}$ . That is, Equation (2.15) has no zero derivative of  $\tilde{h}$  that might otherwise lead to a divergence of the iterative procedure. The Newton-Raphson method requires an initial guess of  $\tilde{h}$  and the derivative of Equation (2.15) for iteration, both of which are presented in Appendix 8.1. We adopt the convergence criterion  $1 - \tilde{h}_i/\tilde{h}_{i+1} \leq \epsilon_{\text{machine}}$ , where  $\tilde{h}_i$  is the approximate root at the  $i$ th iteration and  $\epsilon_{\text{machine}}$  is the machine precision ( $10^{-7}$  and  $10^{-16}$  for single and double precision, respectively).

After obtaining  $\tilde{h}$ , we substitute it into Equation (2.5b) to get four-velocity:

$$U^i = \frac{M^i c^2}{D(c^2 + \tilde{h})}. \quad (2.17)$$

Next, we compute the Lorentz factor and proper mass density from Equation (2.8) and Equation (2.5a) and then use Equation (2.16) to obtain temperature. Finally, the pressure is given by

$$p = \rho c^2 \left( \frac{k_B T}{mc^2} \right). \quad (2.18)$$

Justifying the superiority of our new conversion scheme using  $\tilde{E}$ , we estimate the relative error of computing  $a - b$  by (Higham, 2002)

$$\frac{|a| + |b|}{|a - b|} \epsilon_{\text{machine}}. \quad (2.19)$$

Thus, the error of the new conversion scheme can be estimated by substituting  $\left[ (\tilde{E}/Dc^2)^2 + 2(\tilde{E}/Dc^2) \right]$  and  $(M/Dc)^2$  for  $a$  and  $b$ , respectively, in Equation (2.19). The error in terms of primitive variables reads

$$\begin{aligned} & \left[ \frac{\gamma^2 (\tilde{h}+1)^2 (1+\beta^2) + \frac{T^2}{\gamma^2} - 2(\tilde{h}+1)T - 1}{(\tilde{h}+1)^2 + \frac{T^2}{\gamma^2} - 2(\tilde{h}+1)T - 1} \right] \epsilon_{\text{machine}} \\ & \approx (1 + \mathcal{M}^2) \epsilon_{\text{machine}}, \end{aligned} \quad (2.20)$$

where  $\beta = \sqrt{v^i v_i}/c$ . The approximate equality in Equation (2.20) holds for all finite temperature.

According to Equation (2.13) and Equation (2.20), we can decide whether to adopt single or double precision before simulations. Taking ultra-relativistic pulsar wind ( $\mathcal{M}_{\text{wind}} \approx 10^6$ ) as an example, we must use double precision to suppress the error to  $10^{-4}$ . But for mild-relativistic AGN jets ( $\mathcal{M}_{\text{jet jet}} < 10$ ), single precision is sufficient to reduce the error to  $10^{-5}$ .

For the original scheme using the total energy density  $E$  instead of  $\tilde{E}$ , a similar error estimation can be performed by replacing  $\tilde{E}$  with  $E - Dc^2$  on the left-hand side of Equation (2.15), which gives

$$\left[ \frac{2\gamma^2 (\tilde{h}+1)^2 + \frac{T^2}{\gamma^2} - 2(\tilde{h}+1)T + (\tilde{h}+1)^2 + 1}{(\tilde{h}+2)\tilde{h} + \frac{T^2}{\gamma^2} - 2(\tilde{h}+1)T} \right] \epsilon_{\text{machine}}. \quad (2.21)$$

Figure 2.2 shows the contour plots of Equation (2.20) for the new scheme (top panel) and Equation (2.21) for the original scheme (middle panel) as a function of  $\mathcal{M}$  and temperature. The bottom panel shows the ratio of Equation (2.21) to Equation (2.20). It demonstrates the advantage of using  $\tilde{E}$ . The top panel shows that using  $\tilde{E}$  in the conversion scheme is almost error-free when dealing with subsonic flows at any finite temperature, including the low- $T$  limit. In supersonic flows, the numerical errors proportional to  $\mathcal{M}^2$  are common and caused by finite digits of floating numbers. In comparison, the middle panel shows the error using  $E$ , which severely suffers from catastrophic cancellation in the low- $T$  limit even when  $\mathcal{M} \ll 1$ . See also Figure 8.3 in Appendix 8.2.

On the other hand, conversion from primitive to conserved variables is also needed in the Riemann solver. This procedure involves straightforward substitution without the need of root-finding. We use

$$\frac{\tilde{h}}{c^2} = 2.5 \left( \frac{k_B T}{mc^2} \right) + \frac{2.25 (k_B T / mc^2)^2}{1 + \sqrt{2.25 (k_B T / mc^2)^2 + 1}}, \quad (2.22)$$

and

$$\frac{\tilde{E}}{Dc^2} = \frac{\left( \frac{\mathbf{M}}{Dc} \right)^2 + f(\tilde{h})}{1 + \sqrt{1 + \left( \frac{\mathbf{M}}{Dc} \right)^2 + f(\tilde{h})}}, \quad (2.23)$$

to compute  $\tilde{h}$  and  $\tilde{E}$ , where  $f(\tilde{h})$  can be computed from Equation (2.15) with known  $\mathbf{M}/Dc$ . Note that Equation (2.22) and Equation (2.23), following directly from Equation (2.10) and Equation (2.15) without any approximation, are written in a form without any subtraction to avoid catastrophic cancellation. In contrast, using Equation (2.5c) and Equation (2.6) to compute the reduced energy density  $\tilde{E}$  can suffer from catastrophic cancellation in the NR limit.

We close this section by providing a flowchart of the new conversion scheme in Figure 8.2 in Appendix 8.2 and by summarizing the equations actually solved by **GAMER-SR**. Other mathematically equivalent forms are unrecommended as they may suffer from catastrophic cancellation in the UR or NR limit.

- Evolution equations: Equation (10.1a, 10.1b, 2.7).

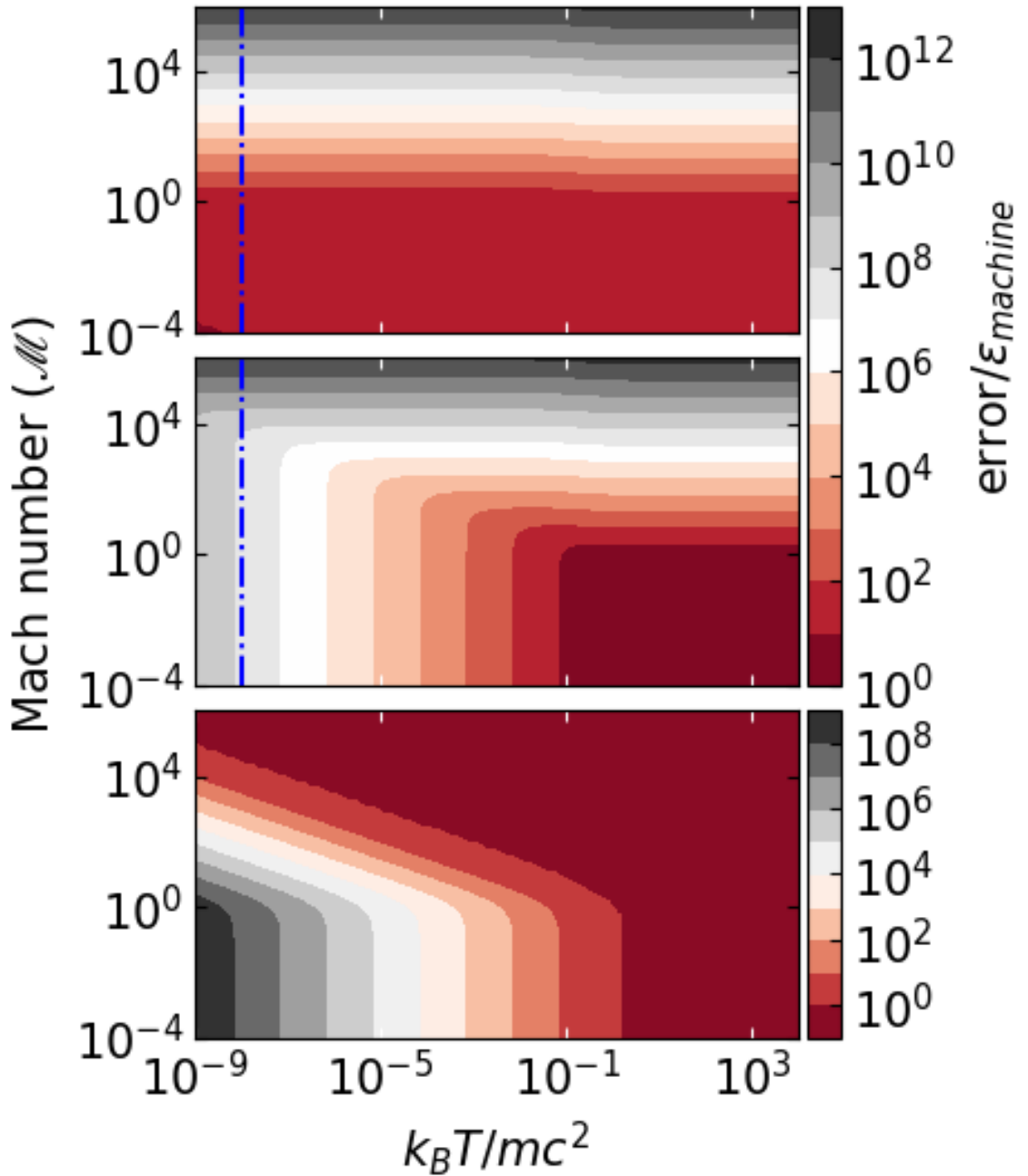


Figure 2.2: Numerical errors of the conversion from conserved to primitive variables as a function of  $\mathcal{M}$  and  $k_B T / mc^2$ . The top and middle panel show the errors of the new and original schemes estimated by Equation (2.20) and Equation (2.21), respectively. The bottom panel shows the ratio of Equation (2.21) to Equation (2.20). Figure 8.3 in Appendix 8.2 provides numerical evidences showing a remarkable consistency with the predicted values at  $k_B T / mc^2 = 10^{-8}$  (blue dashed-dotted line).

- Lorentz factor: Equation (2.8).
- Four-velocities: Equation (2.17).
- Temperature: Equation (2.16).
- Pressure: Equation (2.18).
- Reduced enthalpy: Equation (2.22).
- Reduced energy density: Equation (2.23).

# Chapter 3

## Numerical methods

### 3.1 A GAMER Primer

Due to the flexibility and extensibility of `GAMER` (Schive et al. 2010; Schive et al. 2018), the SRHD module directly inherits the AMR structure and the MPI/OpenMP/GPU parallelization framework of hydrodynamics, and therefore we only provide a summary here. We define the base grid resolution as level-0 and the  $\ell$ th refinement as level- $\ell$ , where level- $\ell$  has a spatial resolution  $2^\ell$  times higher than that of the base level. Data in `GAMER` are always decomposed into patches, each of which consists of  $8^3$  cells, and the AMR implementation is realized by constructing a hierarchy of patches in an octree structure. According to user-defined refinement criteria, we can create or remove fine patches under the proper-nesting constraint.

In addition to the refinement criteria provided by the hydrodynamics module, we also implement two refinement criteria for SRHD: the gradient of the Lorentz factor and the magnitude of  $|\mathbf{M}|/D$ . The former aims to capture the thin and high- $\gamma$  shell in the Sedov-Taylor blast wave, while the latter ensures that the spine region in an over-pressured jet (cf. Figure 6.3) can be fully resolved. For all refinement criteria, the refinement thresholds on different levels can be set independently as run-time parameters.

We port the routines involving massive floating-point operations to GPUs such as the SRHD solvers and time-step calculations. On the other hand, we use CPUs to perform ghost-zone interpolation and patch refinement. As a result, we recommend using the

refinement criteria only involving conserved variable for better performance because conserved variables are readily available from memory. By contrast, primitive variables can only be obtained by root-finding iteration, which is computationally expensive.

For enhancing software portability and reusability, GAMER not only supports both CPU-only and GPU modes but also allows the same physics modules to be shared by both CPU and GPU computations. Specifically, in the CPU-only mode, we compute different grid patches in the same MPI process in parallel with OpenMP. In the GPU mode, we replace these OpenMP parallel clauses with CUDA thread blocks and then use threads within the same thread block to update all cells within the same grid patch. This scheme maximizes the reuse of physics routines, avoids redundant code development and maintenance, and significantly lowers the barrier of code extension, especially for developers not acquainted with GPU programming. We have utilized this CPU/GPU integration infrastructure in the SRHD implementation.

GAMER-SR supports the MUSCL-Hancock (Toro, 2011) and VL (Falle 1991; van Leer 2006) schemes for numerical integrations and both piece-wise linear method (PLM; van Leer 1979) and piecewise parabolic method (PPM; Woodward & Colella 1984) for data reconstruction. For the Riemann solver, it supports both relativistic HLLC and HLLE solvers (Mignone & Bodo 2005; Mignone & Bodo 2006), which have been adapted not only to be compatible with the TM EoS by using the corresponding sound speed, Equation (2.14), but also to evolve the reduced energy density (i.e. replacing  $E$  with  $\tilde{E} + Dc^2$ ).

## 3.2 Flexible Time-step

GAMER-SR provides two Courant-Friedrichs-Lowy (CFL) conditions for time-step determination. The first one is based on the local signal propagation speed,  $S_{\max}$ , which gives maximum allowed time-steps in a wide dynamical range. Thus, it can significantly improve performance when the maximum  $v/c$  is not close to unity. The other is based on the speed of light, where we simply replace  $S_{\max}$  by  $c$ . It gives the most conservative estimation of time-steps and is more time-consuming when the flow speed is far less than

$c$ , although it is simple to implement and requires less computation.

To calculate  $S_{\max}$ , we first define  $\hat{\mathbf{u}}_s$  to be a spatial unit vector in the direction of sound propagation, we then apply the Lorentz boost with velocity  $-\boldsymbol{\beta}$  to the four-velocity of sound speed  $(\gamma_s, U_s \hat{\mathbf{u}}_s)$  from local rest frame to laboratory frame. We finally obtain the four-velocity of signal that travels in laboratory frame as follows:

$$\left( \gamma \gamma_s + \gamma U_s (\boldsymbol{\beta} \cdot \hat{\mathbf{u}}_s), U_s \hat{\mathbf{u}}_s + (\gamma - 1) U_s (\hat{\boldsymbol{\beta}} \cdot \hat{\mathbf{u}}_s) \hat{\boldsymbol{\beta}} + \boldsymbol{\beta} \gamma \gamma_s \right), \quad (3.1)$$

where  $\gamma$  and  $\gamma_s$  are the Lorentz factor of flow and of sound speed.  $U_s$  is the four-velocity of sound speed defined by  $c_s / \sqrt{1 - c_s^2}$ . Since the direction of the fastest signal propagation is in general parallel to flow velocity, we assume that both sound and flow propagate in the same direction (i.e.  $\hat{\mathbf{u}}_s = \hat{\boldsymbol{\beta}}$ ). The spatial components of Equation (3.1) then reduce to

$$(\beta \gamma \gamma_s + \gamma U_s) \hat{\boldsymbol{\beta}}. \quad (3.2)$$

Motivated by Equation (3.2), we simply choose  $U^i \gamma_s + \gamma U_s$  as the bound of each spatial component and sum over  $U^i \gamma_s + \gamma U_s$  for each spatial component to obtain

$$U_{\max} = \gamma_s (U_x + U_y + U_z) + 3\gamma U_s, \quad (3.3)$$

where  $U_{x/y/z}$  is the  $x/y/z$ -component of the four-velocities of flow.

Note that Equation (3.3) is essentially the addition of flow speed and sound speed in special relativity theory. Converting Equation (3.3) back to three-velocity

$$S_{\max} = U_{\max} / \sqrt{1 + (U_{\max}/c)^2}, \quad (3.4)$$

and substituting Equation (3.4) into the CFL condition, we finally obtain the flexible time-step based on the local signal propagation speed for SRHD:

$$\Delta t = C_{\text{CFL}} \left( \frac{\Delta h}{S_{\max}} \right), \quad (3.5)$$

where  $\Delta h$  is the cell spacing and  $C_{\text{CFL}}$  the safety factor with a typical value of  $\sim 0.5$  for MUSCL-Hancock and VL schemes.

Note that Equation (3.5) can be reduced to its non-relativistic counterpart,

$$\Delta t = C_{\text{CFL}} \left( \frac{\Delta h}{v_x + v_y + v_z + 3c_s} \right), \quad (3.6)$$

when  $\gamma \sim 1$  and to  $\Delta t = C_{\text{CFL}} \Delta h / c$  when  $\gamma \gg 1$ .

### 3.3 Handling unphysical results

Unphysical results, for example, negative pressure, negative density and superluminal motion, can stem from the failure of the following criterion:

$$\left( \frac{\tilde{E}}{Dc^2} \right)^2 + 2 \left( \frac{\tilde{E}}{Dc^2} \right) - \left( \frac{\mathbf{M}}{Dc} \right)^2 > \epsilon_{\text{machine}}, \quad (3.7)$$

where the left-hand side involves the numerically updated quantities and  $\epsilon_{\text{machine}}$  is the machine epsilon – typically,  $2 \times 10^{-16}$  for double precision and  $1 \times 10^{-7}$  for single precision. The failure may take place in one of the following four steps:

#### (1) SRHD solver

SRHD solver is responsible for updating the conserved variables by a given time-step. If unphysical result occurs in a cell, we redo data reconstruction by reducing the original minmod coefficient by a factor of 0.75. If the failure still occurs, we further reduce the minmod coefficient repeatedly until Equation (3.7) passes or the reduced minmod coefficient vanishes. Note that interpolating with a vanished minmod coefficient is essentially equivalent to the piece-wise constant spatial reconstruction.

#### (2) Grid refinement

Unphysical results may occur during grid refinement when performing interpolations on parent patches. The remedy here is the same as that in the SRHD solver. We repeat the interpolation process with a reduced minmod coefficient on the conserved variables until Equation (3.7) passes or the minmod coefficient vanishes. A vanished minmod

coefficient is essentially equivalent to directly copying data from the parent patch without interpolation.

### *(3) Ghost-zone interpolation*

To preserve conservation, where the volume-weighted average of child patch data are equal to its parent patch data, we normally fill the ghost zones of the patches on level  $\ell + 1$  by interpolating the conserved variables on level  $\ell$  when the ghost zones lie on level  $\ell$ . However, if unphysical results occur, we interpolate primitive variables instead. Interpolating primitive variables is more robust than interpolating conserved variables since Equation (3.7) is always satisfied. After interpolation, we fill the ghost zones with the conserved variables derived from the interpolated primitive variables. Note that this procedure still preserves conservation because ghost zones do not affect conservation.

### *(4) Flux correction operation*

For a leaf coarse patch adjacent to a coarse-fine interface, the flux difference between the coarse and fine patches on the interface will be used to correct the coarse-patch conserved variables adjacent to this interface. If unphysical results are found after this flux correction, we simply ignore the correction on the failed cells. Skipping the correction will break the strict conservation but it only occurs rarely.



# Chapter 4

## Test problems

To understand how evolving the total energy density may deteriorate simulation results and to demonstrate how much the new scheme improves, we compare the results from evolving  $E$  by the flux  $M$  (original scheme) with that from evolving  $\tilde{E}$  by the flux  $(\tilde{E} + p)U_x/\gamma$  (new scheme). Since catastrophic cancellation is likely to occur in UR and NR limits, we will conduct several test problems in these two limits. All simulations throughout this paper adopt the HLLC Riemann solver and PLM data reconstruction unless otherwise specified.

### 4.1 Convergence test for sinusoidal waves

We perturb proper mass density in the high- and low- $T$  limits to compare the accuracy of both schemes over a wide dynamical range. We construct the initial conditions as follows. All cases share homogeneous and static background with proper mass density  $\rho_0 = 1$  on uniform grids, whereas the ambient temperatures are set to  $k_B T/mc^2 = 10^{10}$  and  $10^{-10}$  for the high- and low- $T$  limits, respectively. We then sinusoidally perturb the background with a tiny amplitude,  $\delta\rho/\rho_0 = 10^{-6}$ .

To monitor how errors in the numerical solution decrease as a function of increasing spatial resolution in the three-dimensional space, we adopt a propagating wave along the diagonal direction of the simulation cubic box with the periodic boundary condition. Thus, the analytical solution is  $\rho(\mathbf{x}, t) = \rho_0 + \delta\rho \sin \left[ (x + y + z)/\sqrt{3} - c_s t \right]$ , where  $c_s$  is the sound speed given by Equation (2.14).

We define the L1-norm error as

$$L1(Q) = \frac{1}{N} \sum_{i=1}^N 1 - \frac{Q_{\text{numerical}}(\mathbf{x}_i)}{Q_{\text{analytical}}(\mathbf{x}_i)}, \quad (4.1)$$

where  $Q_{\text{numerical}}(\mathbf{x}_i)$  is the numerical solution of  $i$ -th cell at  $\mathbf{x}_i$  and  $Q_{\text{analytical}}(\mathbf{x}_i)$  is the corresponding analytical solution. We then calculate the L1 error of the proper mass density along the wave propagating direction. As shown in Figure 4.1, the L1 errors of the new scheme in both the high- $T$  limit (■) and low- $T$  limit (✚) decrease as  $N^{-2}$ , consistent with the second-order accuracy of the MUSCL-Hancock scheme with PLM data reconstruction. However, the error of the original scheme in the low- $T$  limit (●) is much larger and roughly equal to a constant of  $2 \times 10^{-6}$ . This is expected because the error arising from the original scheme can be estimated from Equation (2.21) in the NR limit:

$$\frac{4}{3 \left( \frac{k_B T}{mc^2} \right)} \epsilon_{\text{machine}}, \quad (4.2)$$

where  $k_B T / mc^2 = 10^{-10}$  and  $\epsilon_{\text{machine}} \sim 10^{-16}$  for double precision.

We thus conclude that for the original scheme in the NR limit, the cancellation between  $(E/Dc^2)^2$  and  $[(\mathbf{M}/Dc)^2 + 1]$  leads to an error of  $\sim 10^{-6}$  when computing primitive variables, roughly consistent with the L1 error (●). For the opposite high- $T$  limit (◆), the discretization error, however, completely overwhelms the error ( $\sim 4\epsilon_{\text{machine}} \sim 4 \times 10^{-16}$ ) estimated from Equation (2.21) in the high- $T$  limit, thus dominating the L1 error. The error arising from the cancellation in the new scheme,  $(\tilde{E}/Dc^2)^2 + 2(\tilde{E}/Dc^2) - (\mathbf{M}/Dc)^2$ , on the left side of Equation (2.15), is close to  $\epsilon_{\text{machine}}$  in both the high- and low- $T$  limits when  $\mathcal{M} < 1$  (see Section 2.3 and Appendix 8.2 for details).

## 4.2 1-D relativistic Riemann problems

The 1-D Riemann problem (Sod, 1978) has played an important role by providing exact nonlinear solutions against which (relativistic) hydrodynamic codes can be tested. Riemann problem is an initial-value problem with a piece-wise constant initial data that has

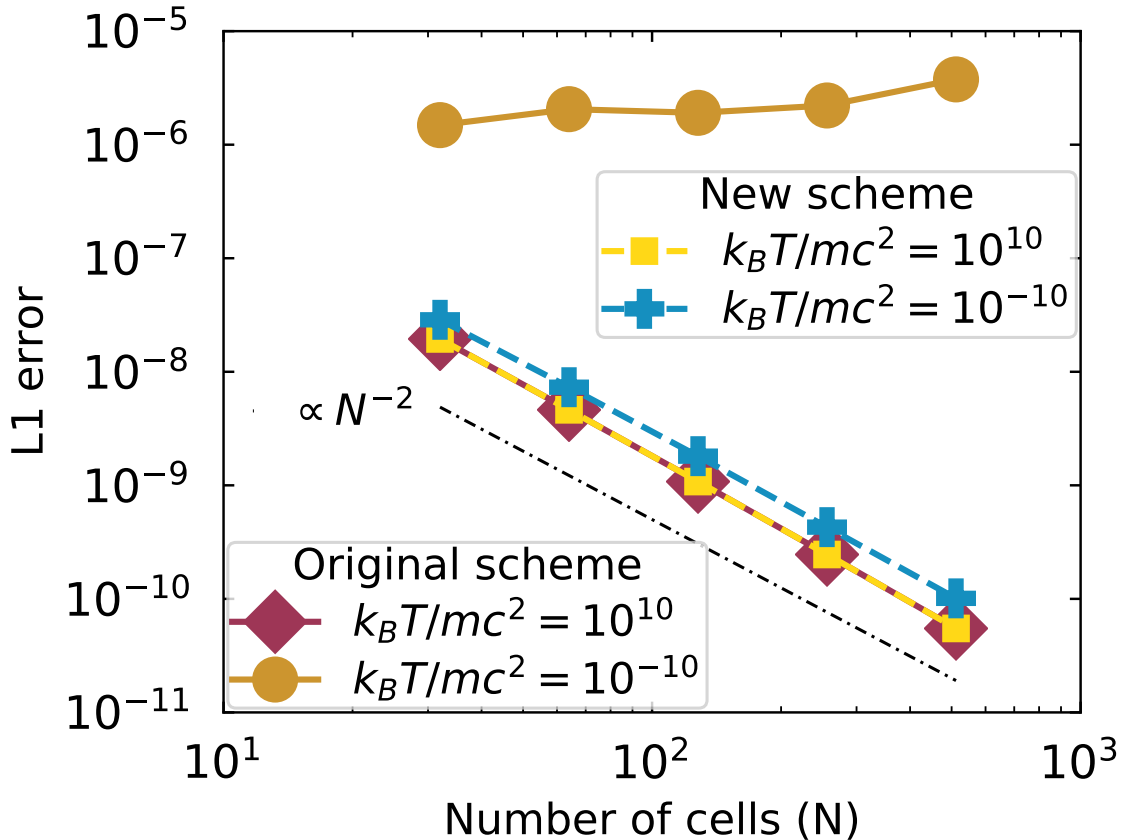


Figure 4.1: Convergence test for sinusoidal waves. The L1 errors of the new scheme in both the high- $T$  limit (yellow squares) and low- $T$  limit (blue pluses) decrease as  $N^{-2}$ , consistent with the second-order accuracy of the MUSCL-Hancock scheme with PLM data reconstruction. However, the L1 error of the original scheme in the low- $T$  limit (brown circles) is much larger and roughly equal to a constant of  $2 \times 10^{-6}$ . This is expected because the error in the original scheme can be estimated from Equation (4.2). For the original scheme in the opposite high- $T$  limit (darkred diamond), the discretization error, however, completely overwhelms the error ( $\sim 4 \times 10^{-16}$ ) estimated from Equation (2.21) in the high- $T$  limit when  $\gamma \sim 1$ , thus dominating the L1 error.

Table 4.1: The left and right initial states of the Riemann problems in Section 4.2. We denote the left/right states by the subscript  $L/R$ .

	$p_L$	$\rho_L$	$U_L$	$p_R$	$\rho_R$	$U_R$	Floating-point format
Ultra-relativistic limit	1.0	$10^{-5}$	$10^6$	1.0	$10^{-5}$	$-10^6$	Double precision
Mixed limits	$10^{-4}$	$10^2$	$10^{-3}$	$10^{-10}$	$10^{-12}$	$-10^2$	Single precision

a single discontinuity in the domain of interest. In this section, we directly compare the new and original schemes by simulating two relativistic Riemann problems. We then demonstrate that the new scheme handles both the UR and NR limits very well. By contrast, the original scheme severely suffers from numerical errors in the NR limit. Both schemes share the same numerical setup, e.g., MUSCL-Hancock integration, PLM data reconstruction, hybrid van-Leer, generalized minmod slope limiter, and uniform grids with the outflow boundary condition. In addition, we have numerically derived the exact solution of a nontrivial relativistic Riemann problem with the TM EoS (see Appendix 8.3 for details) in order to verify the numerical results.

### 4.3 Ultra-relativistic limit

We simulate a head-on collision of two identical gases with  $\gamma = 10^6$  and  $k_B T/mc^2 = 10^5$  with uniform 512 grids. The computational domain is in the interval  $[0, 1]$ . The initial discontinuity is located at  $x = 0.5$ . The first row of Table 4.1 presents the initial right and left states. Figure 4.2 shows the results at  $t = 1.0$ . The left panels show the entire simulation domain, while the right panels show the zoom-in image of the post-shock region, which has been violently heated up to ultra-relativistically hot temperature ( $k_B T/mc^2 \sim 10^{11}$ ) by the extremely high- $\gamma$  gases flowing inwards from both sides. As can be seen, the new scheme (○) fully agrees with the original scheme (★) on the large-scale profile but also on the small-scale errors, meaning that the new scheme does not sacrifice the numerical accuracy in the UR limit. In addition, we notice that the non-negligible and spurious waves occur in the post-shock region, which are not due to root-finding iterations but to spatial discretization errors as the spurious waves can be reduced by increasing spatial resolution.

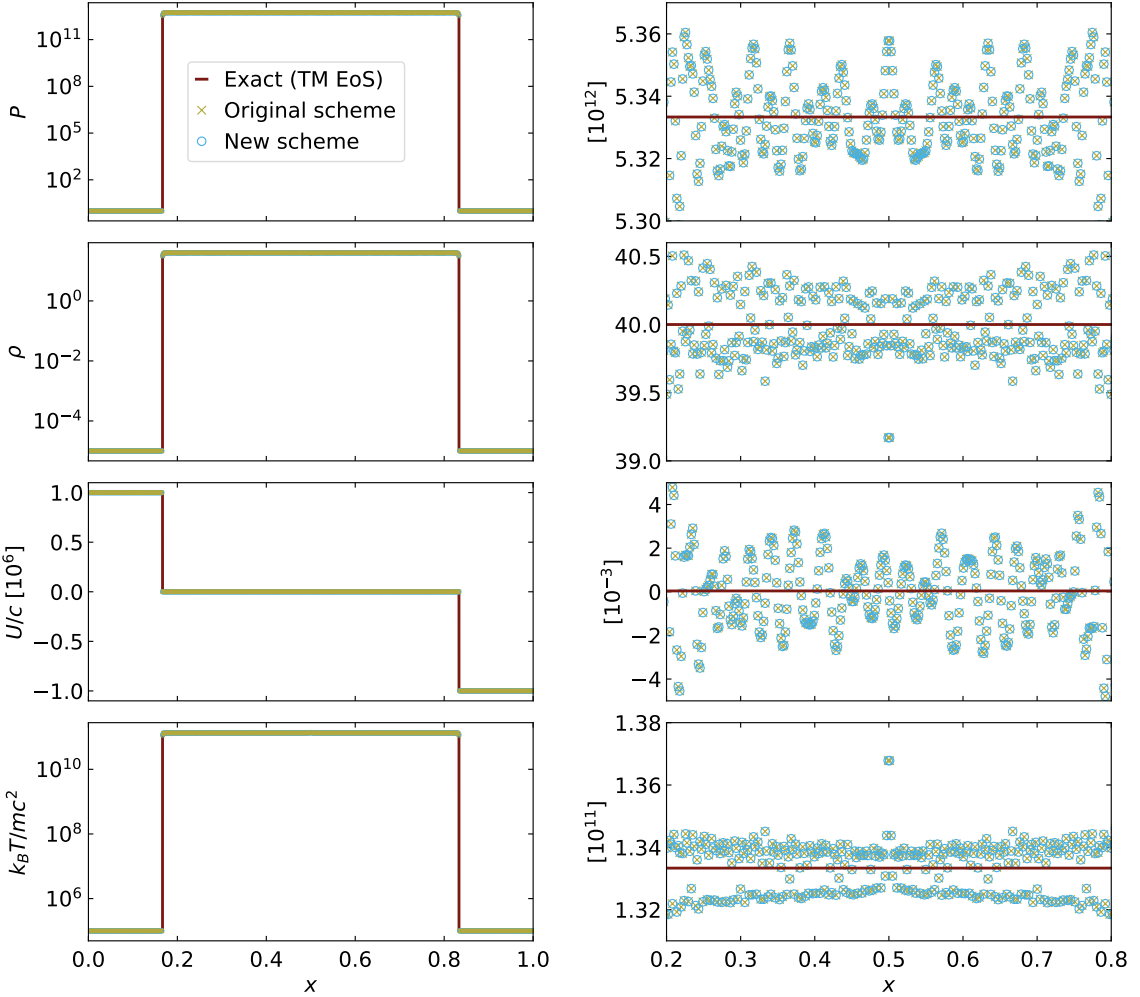


Figure 4.2: Riemann problem in the UR limit with a head-on collision of two identical gases with  $\beta\gamma = 10^6$  and  $k_B T/mc^2 = 10^5$  at  $t = 1.0$ . The left column shows the entire simulation domain, while the right column shows the zoom-in image of the post-shock region. From top to bottom: pressure, proper mass density, four-velocity, and temperature. Note that we plot the Mach number in the zoom-in image (right column) of four-velocity so as to readily compare the amplitude of velocity oscillation with sound speed. The new scheme (blue circles) fully agrees with the original scheme (olive crosses) not only on the large-scale profiles but also on the small-scale errors, meaning that the new scheme (blue circles) does not sacrifice (or improve) the numerical accuracy in the UR limit for that in the NR limit.

## 4.4 Mixed limits

To demonstrate that the new scheme can handle a large dynamical range covering both extremely hot and extremely cold gases, we simulate a nontrivial Riemann problem where the temperature straddles between the high- and low- $T$  limits. This initial condition evolves into a cold left-traveling rarefaction wave separated by a contact discontinuity to match an extremely hot downstream of an ultra-relativistic shock traveling toward the right. Also, we have numerically derived the exact solution of this particular Riemann problem with the TM EoS (see Appendix 8.3). The second row in Table 4.1 shows the initial left and right states. The simulation adopts a computational domain [0,100] with 102,400 cells. Since the speed of the right-traveling shock is 276 times faster than that of the left-traveling rarefaction wave, we put the initial discontinuity at  $x = 5 \times 10^{-2}$  to provide an ample space for the right-traveling shock.

Figure 4.3 shows the results at  $t = 80$ , where there are three points to be emphasized. First, we find not only that the shock front at  $x = 26$  is well resolved by 3–4 cells but also that the new scheme (✖) agrees well with the exact solution of the TM EoS (—), as shown in all insets. Second, the L1 error, defined by Equation (4.1), of the density profile from the original scheme (○) is 23 per cent within the region between the head of rarefaction wave ( $x = 2.67 \times 10^{-2}$ , the third number from top in the leftmost column of Table 8.1 in Appendix 8.3) and initial discontinuity ( $x = 5 \times 10^{-2}$ ), consistent with the 20 per cent error estimated by Equation (4.2) with  $k_B T/mc^2 = 8 \times 10^{-6}$ . Similar conclusions can be drawn for other physical quantities. However, in the region  $5 \times 10^{-2} < x < 0.3$  swept by the right-traveling contact discontinuity, errors of the original scheme are much larger than the estimate, which requires further investigation. Third, the solutions of the TM EoS (—) match well with both  $\Gamma = 5/3$  (·····) in the NR region ( $x < 0.21$ ) and  $\Gamma = 4/3$  (·····) in the UR region ( $x > 0.27$ ). It demonstrates the capability of capturing the transition from  $\Gamma = 5/3$  (for  $k_B T/mc^2 \rightarrow 0$ ) to  $\Gamma = 4/3$  (for  $k_B T/mc^2 \rightarrow \infty$ ) for the new scheme. The exact solutions of this test are shown in Table 8.1 in Appendix 8.3.

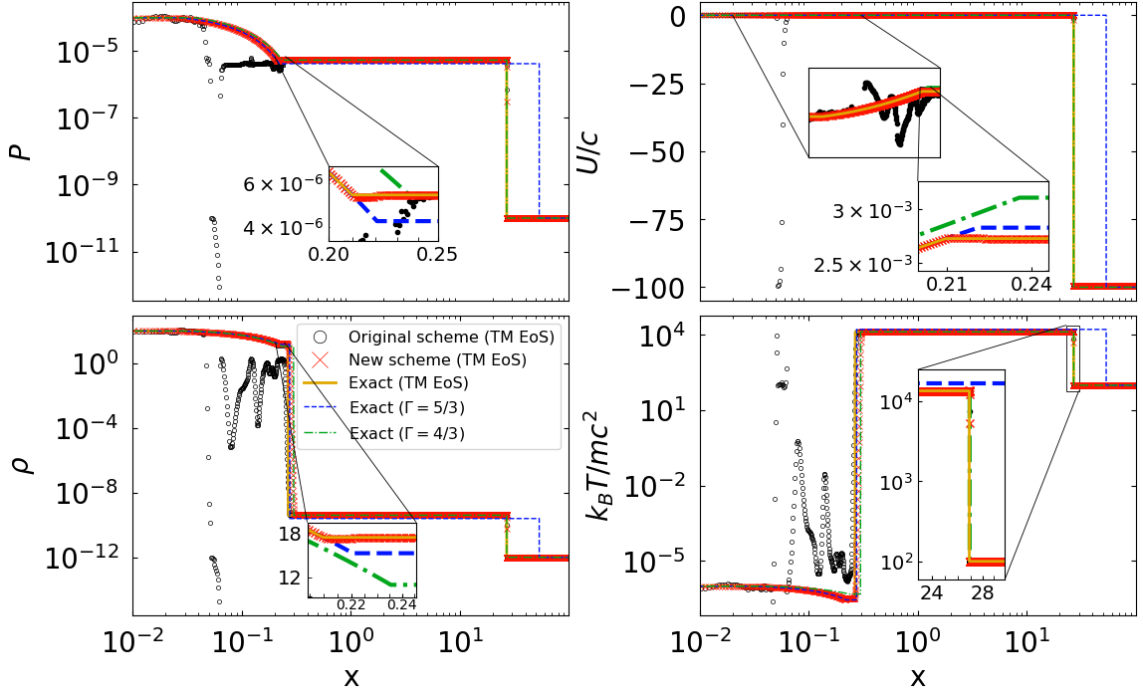


Figure 4.3: Riemann problem in the mixed UR and NR limits at  $t = 80$ . The second row in Table 4.1 shows the initial condition. Clock-wise from top-left: pressure, 4-velocity, temperature, and proper mass density. We find not only that the shock front at  $x = 26$  is well resolved by 3–4 cells but also that the new scheme (red crosses) agrees well with the exact solution of the TM EoS (yellow lines), as shown in all insets. The L1 error of the density profile from the original scheme (black circles) is 23 per cent within the region between the head of rarefaction wave and initial discontinuity (i.e.  $2.67 \times 10^{-2} < x < 5 \times 10^{-2}$ ), consistent with the 20 per cent error estimated by Equation (4.2) with  $k_B T / mc^2 = 8 \times 10^{-6}$ . However, in the region  $5 \times 10^{-2} < x < 0.3$  swept by the right-traveling contact discontinuity, errors of the original scheme are much larger than the estimate, which requires further investigation. The TM profiles match well with both the  $\Gamma = 5/3$  profiles (blue dashed lines) in the NR region ( $x < 0.21$ ) and the  $\Gamma = 4/3$  profiles (green dashed lines) in the UR region ( $x > 0.27$ ).

## 4.5 Multi-dimensional grid effects for high- $\mathcal{M}$ flows

To investigate the detrimental impact of grid effects on the evolution of ultra-relativistic and high Mach number hydrodynamic problems, we separately simulate two identical three-dimensional mono-direction flow with different flow directions. One flow is along the diagonal direction of the simulation box and the other is parallel to the grid direction. Both simulations share the same numerical set-up as follows. Flows are initially represented by cylinders extending to the boundaries of a periodic cubic box with a width  $L$ . The cylinder diameter is  $D = 0.028L$ . The proper mass density ratio of the flow and the ambient is  $\rho_{\text{flow}}/\rho_{\text{amb}} = 10^{-5}$ . The temperatures of the flows and the ambient are  $k_B T_{\text{flow}}/mc^2 = 1.0$  and  $10^{-5}$ , respectively. The four-velocity ( $\gamma\beta$ ) profile inside the flow source is  $10^6(1 + \cos(2\pi r/D))$ , where  $r$  is the distance from the flow axis inside the source. Other physical quantities are uniformly distributed inside the source.

The AMR base level is covered by  $64^3$  cells in all cases. We adopt the gradient of the proper mass density and the magnitude of  $\mathbf{M}/D$  as the two inclusive refinement criteria. We refine a patch if the gradient of a cell satisfies

$$\frac{\Delta h_\ell}{Q} \left( \frac{\partial Q}{\partial x} + \frac{\partial Q}{\partial y} + \frac{\partial Q}{\partial z} \right) > C_Q, \quad (4.3)$$

where  $Q = \rho$ ,  $C_Q = 0.3$ , and  $\Delta h_\ell$  is the cell size at refinement level  $\ell$ . This criterion aims to capture the finger structure due to instabilities at the interface between the flow and the ambient gases. Also, a patch will be refined when any cell satisfies  $\mathbf{M}/D > 10^4$  so that the high-speed region is refined to the finest level.

Figure 4.4 shows the simulation results at  $t = 0.4L/c$ . In Figures 4.4(a) and 4.4(b), we adopt four AMR levels to ensure that the flow diameter can be resolved by 28 cells. The extremely high Mach number ( $\mathcal{M} \sim 10^6$ ) flow leaves any instability short of time to develop, and one expects a smooth flow-ambient interface. However, the interface of the oblique flow turns out to be subject to severe dissipation. The fuzzy-looking cross-sections in the transverse slices of the oblique flow (right column in Figure 4.4(b)) suggest that the dissipation is caused by numerical instabilities when high Mach number flow travels

obliquely across Cartesian grids. This numerical problem is not limited to relativistic high Mach number flows but also occurs in non-relativistic high Mach number flows.

To examine this issue further, we increase the spatial resolution by a factor of 2 and decrease the time-step by a factor of 0.3 from the standard Courant condition. The results (Figures 4.4(c) and 4.4(d)) indicate that increasing spatial and temporal resolution can neither significantly ameliorate the dissipation nor help the oblique flow converge to the horizontal flow. This artificial grid effect can adversely influence the study of high-speed jets, especially for hydrodynamical instabilities near the jet boundaries.

An example of this boundary instability is the finger-like pattern observed immediately outside the parallel flow (right column in Figure 4.4(a)), which we believe to arise from a genuine instability seeded by discretization noise. The finger-like pattern has a higher temperature than the ambient, and in fact consists of two-dimensional flat sheets along the flow. This is demonstrated in Figure 4.5 with transverse slices cut through ‘B’ and ‘C’. The patterns are identical to that cut through ‘A’ in Figure 4.4(c). These 2-D sheet pattern persists even after adding 1 per cent level of white noise into the background density, illustrating that the coherence of sheets along the flow direction is genuinely generated by the high-speed flow boundaries. This finger pattern is similar, but not identical, to the curvature-driven fingers of a knotted jets reported recently (Gourgouliatos & Komissarov, 2017). Our flow has a smooth and parallel boundary without any curvature to drive the fingers.

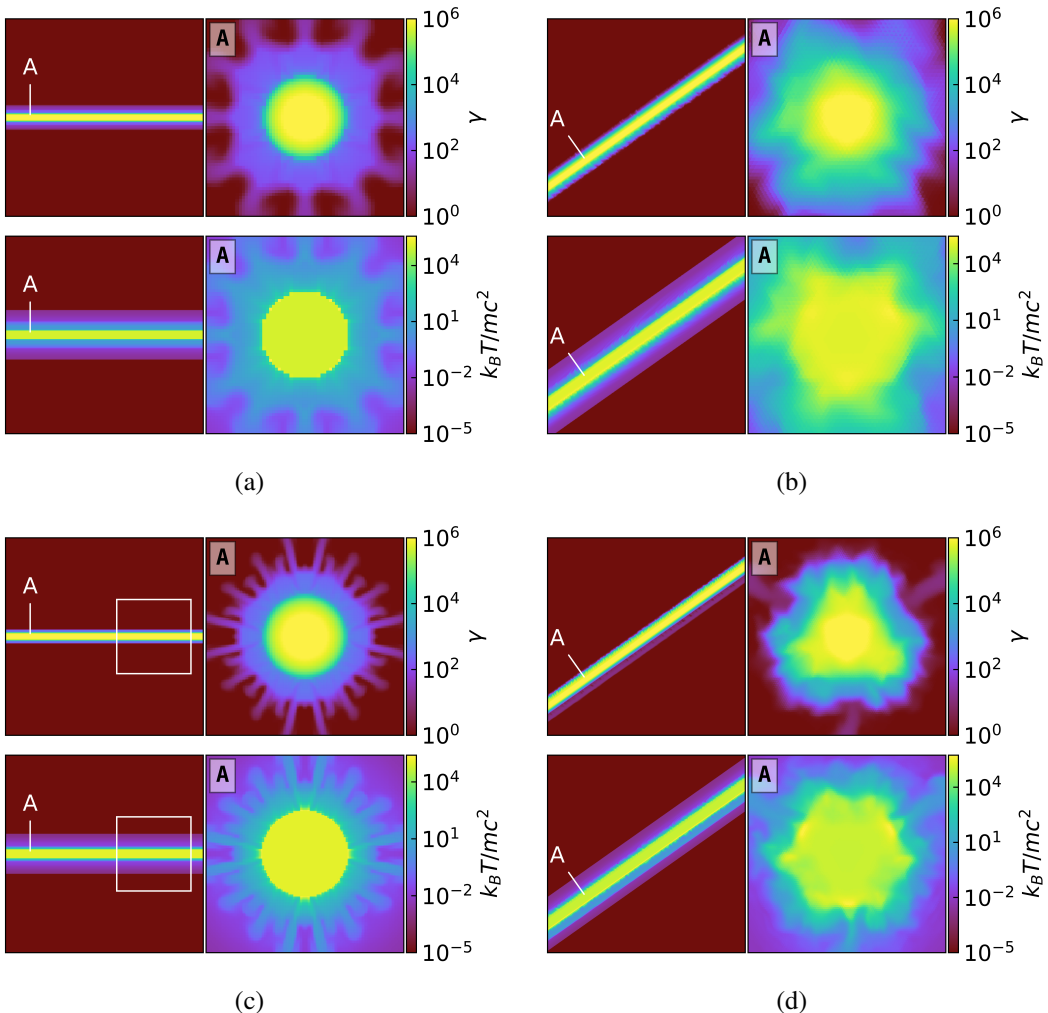


Figure 4.4: Ultra-relativistic flows propagating along different spatial directions with respect to the grids. In all subsrhd-figures (a)–(d), the left and right columns are the longitudinal and transverse slices, respectively. Longitudinal slices are taken through the flow source while the transverse slices are taken through the label ‘A’. The flow diameter is resolved by 28 cells in (a) and (b) and by 56 cells in (c) and (d). The flow has an extremely high Mach number ( $\mathcal{M} \sim 10^6$ ) leaving any instability short of time to develop, and one expects a smooth flow-ambient interface. However, the fuzzy-looking cross-sections in the transverse slices of the oblique flow (right columns in (b) and (d)) suggest that the high-speed flow induces false instability when the flow travels obliquely across Cartesian grids. Increasing the spatial and temporal resolution does not help the numerical solution of an oblique flow to converge to that of a parallel flow.

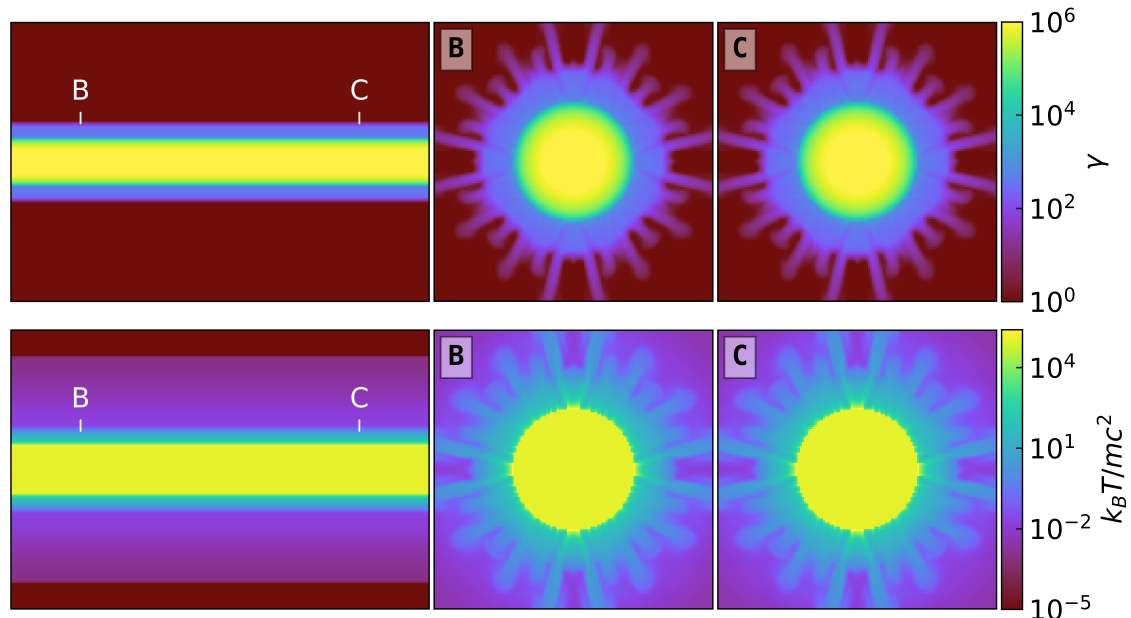


Figure 4.5: Close-up view of the rectangular region in Figure 4.4(c) with longitudinal (first column from the left) and transverse (other columns) slices passing through ‘B’ and ‘C’, respectively. Compared with Figure 4.4(c), it clearly shows that the finger pattern consists of 2-D flat sheets along the flow.



# Chapter 5

## Performance scaling

We measure both strong and weak scalings of GAMER-SR with AMR and hybrid MPI/OpenMP/GPU parallelization. The simulations were conducted on the **Piz-Daint** supercomputer that provides a 12-core Intel Xeon E5-2690 CPU and a Tesla P100 GPU on each computing node. Strong and weak scalings are defined as how the simulation wall time varies with the number of computing nodes for a fixed total problem size and for a fixed problem size per node, respectively. We launch one MPI process with 12 OpenMP threads per node and enable GPU acceleration with single precision.

We divide this section into two parts. First, we measure the strong scaling of a relativistic jet simulation. The simulation set-up, such as initial condition, boundary condition, and grid refinement, follows those described in Section 6.2. Second, we present the weak scaling for periodic and spherical multi-blast waves test (see Figure 5.1). Note that the overall performance (i.e. total cell updates per second) in both tests have excluded ghost zones in the cell number counts.

### (1) Strong scaling:

Figure 5.2 shows the strong scaling results. The parallel efficiency for strong scaling is defined by  $[T(N_{\text{ref}})/T(N_{\text{node}})]/(N_{\text{node}}/N_{\text{ref}})$ , where  $T(N_{\text{node}})$  is the simulation wall time using  $N_{\text{node}}$  nodes.  $N_{\text{ref}}$  is the number of nodes for reference and is fixed to 16 in our test. The overall performance reaches  $5 \times 10^{10}$  cell updates per second with 2048 GPU nodes, corresponding to a parallel efficiency of  $\sim 45$  per cent. The deviation from the ideal scaling is mainly due to MPI communication as (1) the load-imbalance in the EoS

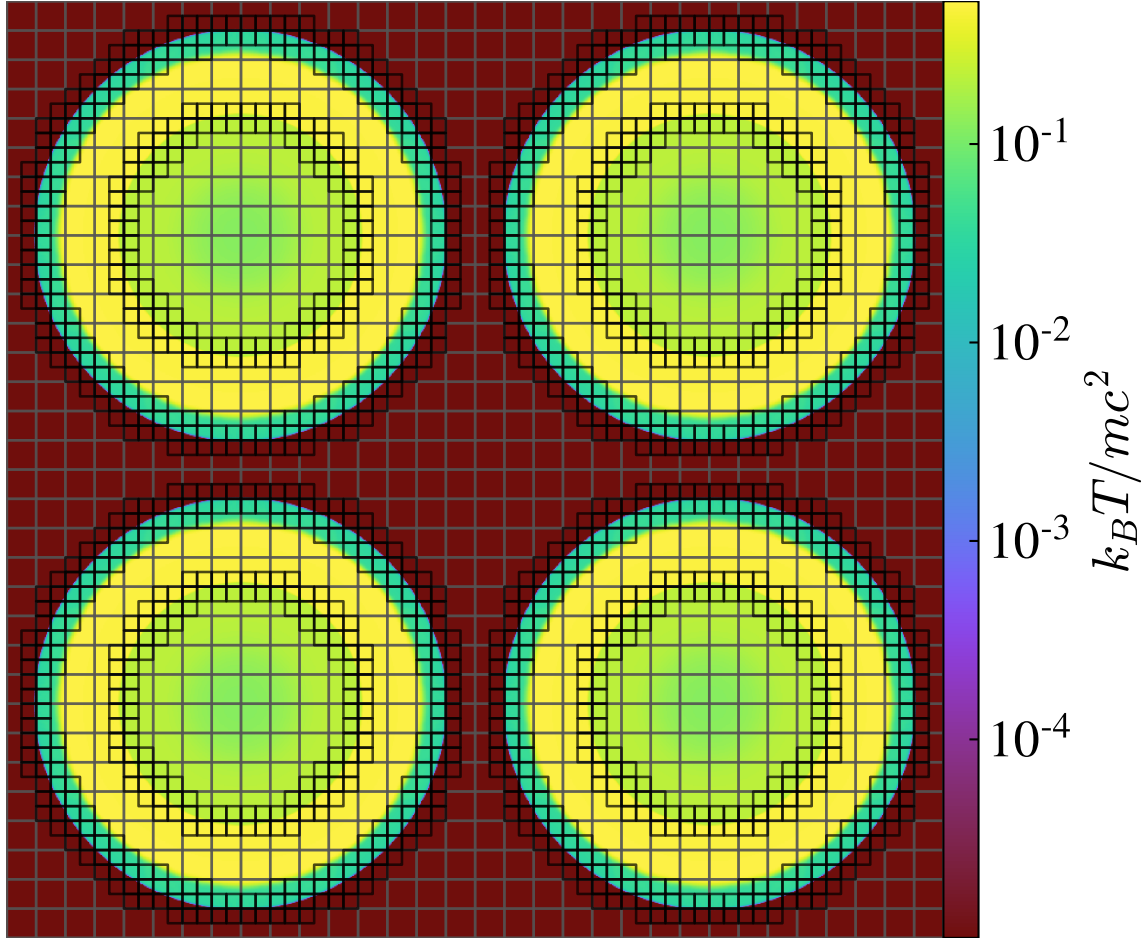


Figure 5.1: Temperature slice through the centre of blast waves at  $t = 0.5L/c$ , with the grid patches overlaid in the case of 8 nodes in the weak scaling test.

iteration is found to be only subdominant, and (2) the MPI communication time accounts for 45 per cent of the wall time with 2048 nodes. Thus, the parallel efficiency would increase from  $0.45$  to  $0.45/(1 - 45\%) \sim 0.82$  if excluding MPI communication.

### (2) Weak scaling:

The periodic computational domain is composed of identical cubic subdomain, each of which has a volume of  $L^3$  and has an explosion source at its own centre with a radius of  $r_{\text{src}} = 0.4L$  and an ultra-relativistic temperature of  $k_B T_{\text{src}}/mc^2 = 10^5$ . The uniform ambient gas has a non-relativistic temperature of  $k_B T_{\text{amb}}/mc^2 = 10^{-5}$  and a density of  $\rho_{\text{src}} = \rho_{\text{amb}} = 1.0$ . Each subdomain is composed of a  $64^3$  base-level grid with three refinement levels, where we refine patches based on the gradient of the reduced energy density. All blast waves evolve from  $t = 0$  to  $t = 0.5L/c$ . We measure the overall performance and parallel efficiency using 1 – 2048 nodes, where each node computes one

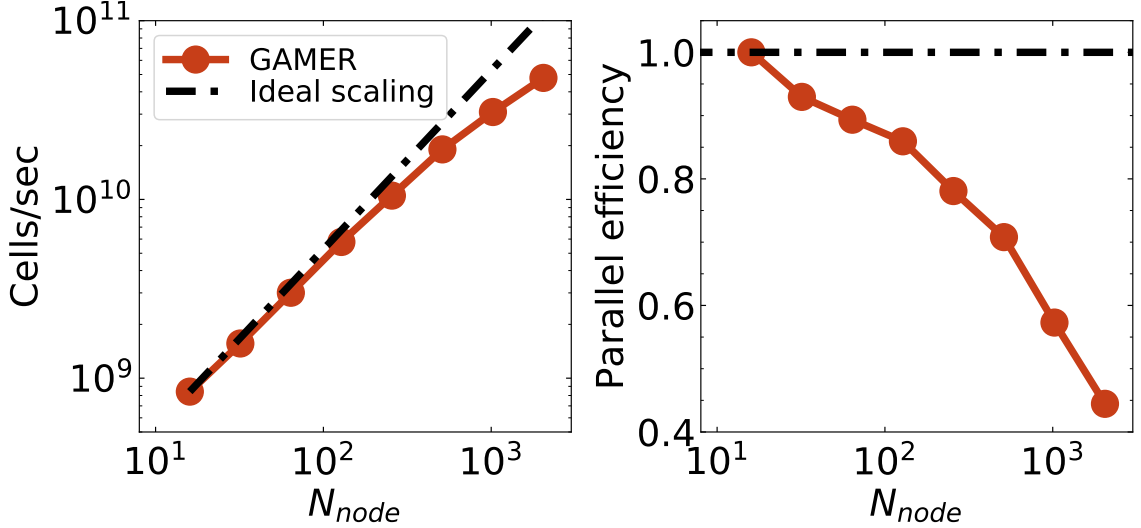


Figure 5.2: Strong scaling of the relativistic jet simulation with five AMR levels and 16–2048 GPU nodes (left panel: cell updates per second; right panel: parallel efficiency). The maximum total number of cells, excluding ghost cells, is  $7.9 \times 10^9$ . The deviation from the ideal scaling is mainly due to MPI communication, the time fraction of which increases by a factor of 10 when increasing the number of nodes from 64 to 2048.

subdomain. Figure 5.1 shows a temperature slice ( $z = 1.5L$ ) through the centre of four blast waves at  $t = 0.5L/c$ , with the grid patches overlaid.

Figure 5.3 shows the weak scaling results. The parallel efficiency for weak scaling is defined by  $T(1)/T(N_{node})$ , where  $T(N_{node})$  is defined the same as the strong scaling. The parallel efficiency is measured to be 90 per cent with 64 nodes and 78 per cent with 2048 nodes, achieving a peak overall performance of  $1.3 \times 10^{11}$  cell updates per second with 2048 nodes. The drop of parallel efficiency is mainly due to MPI communication, the time fraction of which increases from 10.3 ( $N_{node} = 64$ ) to 18.8 per cent ( $N_{node} = 2048$ ).

We remark that the strong and weak scaling tests demonstrate 55 and 80 per cent parallel efficiencies, respectively, with 1024 nodes on the Piz-Daint supercomputer. Moreover, the peak performance on a single Tesla P100 GPU achieves  $7 \times 10^7$  cell updates per second, which is about one-third of the peak performance of non-relativistic hydrodynamics (Schive et al., 2018).

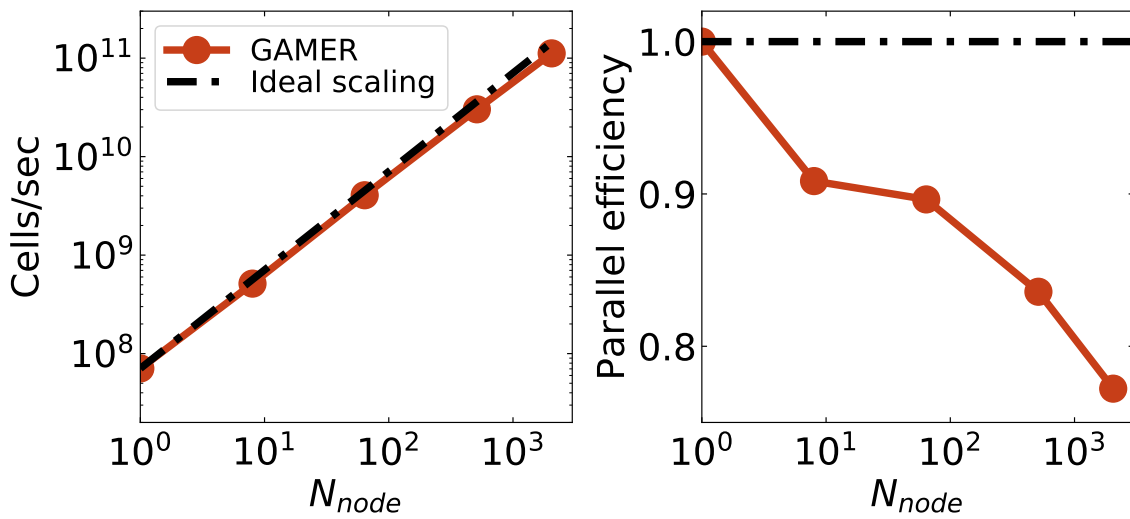


Figure 5.3: Weak scaling of the multi-blast waves simulation with three AMR levels and 1–2048 GPU nodes (left panel: cell updates per second; right panel: parallel efficiency). The maximum total number of cells, excluding ghost cells, is  $6.9 \times 10^7$  per node. The parallel efficiency drops from 0.90 to 0.78 when  $N_{node}$  increases from 64 to 2048 mainly because the MPI communication time fraction increases from 10.3 to 18.8 per cent.

# Chapter 6

## Astrophysical applications

### 6.1 Triaxial blast wave

This triaxial relativistic blast wave problem models a hypothetical astrophysical mega-explosion driven by an ultra-relativistically hot plasma source absent of particular symmetry. It is an atypical test for which we verify the code's ability to deal with strong 3D shocks. The simulation evolves a blast wave from a triaxial source in a homogeneous medium. The triaxial source has aspect ratios  $1 : 1.5 : 2$  with a semi-major axis  $0.01L$  aligned with the diagonal direction, where  $L$  is the width of a cubic computational box. The source is filled with a uniform ultra-relativistic ( $k_B T_{\text{src}}/mc^2 = 10^6$ ) plasma and the ambient is filled with a uniform non-relativistic ( $k_B T_{\text{amb}}/mc^2 = 10^{-9}$ ) HII gas. The density is homogeneous throughout the entire domain with  $\rho_{\text{src}} = \rho_{\text{amb}} = 1.0$ . After the system quickly relaxes, the hot plasma rapidly expands driving a forward shock traveling almost at the speed of light.

The AMR base level is covered by  $32^3$  cells with the periodic boundary condition. The highest refinement level is 9 so that the initial source can be adequately resolved by approximately 82 cells along the minor axis. To refine both the initial source and the thin shell of the blast wave shock, we adopt the gradient of the reduced energy density as the refinement criterion, with  $Q = \tilde{E}$  and  $C_Q = 1.0$  in Equation (4.3).

For comparison, we also simulate a spherical blast wave to understand how the initially triaxial shape affects the evolution of the ultra-relativistic blast wave. Both the spherical

and triaxial cases have the same simulation set-up and the same source volume, i.e.  $r/L = \sqrt[3]{0.01 \times 0.0075 \times 0.005}$ , where  $r$  is the radius of the spherical source.

Figure 6.1 shows the results. We observe that the interior hot plasma pushes out a contact discontinuity immediately inward of the shock and that the thickness of the shell between the contact discontinuity and the shock diminishes in time. In early time, the triaxial profiles (green) at  $t = 0.05L/c$  deviate from the spherical counterparts (red), especially in the pressure and proper mass density, although the shock positions almost coincide. However, at a later time, the profiles at  $t = 0.3L/c$  show no significant difference between the triaxial (yellow) and spherical (blue) blast waves, indicating the initial shape of the source does not have a great impact on the asymptotic evolution of ultra-relativistic blast waves.

To further investigate how the triaxial blast wave evolves into a spherical one, we extract the radii  $R_L(t)$  and  $R_S(t)$  of the triaxial blast wave along the semi-major ( $r_L$ ) and semi-minor axes ( $r_S$ ) of the initial source from simulation data. As shown in Figure 6.2, we find that the dimensionless quantity  $\left(\ln\left(\left(\frac{R_L - R_S}{\sqrt{R_L R_S}}\right) / \left(\frac{r_L - r_S}{\sqrt{r_L r_S}}\right)\right)\right)^2$  is approximately equal to  $0.66 (\sqrt{R_L R_S} / \sqrt{r_L r_S} - 1)$ . This dependence suggests that the triaxiality is damped out with the blast wave propagation by the relation:

$$\frac{R_L(t) - R_S(t)}{\sqrt{R_L(t)R_S(t)}} = \left(\frac{r_L - r_S}{\sqrt{r_L r_S}}\right) \exp\left[-0.81\left(\frac{\sqrt{R_L(t)R_S(t)}}{\sqrt{r_L r_S}} - 1\right)^{1/2}\right]. \quad (6.1)$$

We remark that this test problem also demonstrates that `GAMER-SR` can successfully handle ultra-relativistic gases embedded in a cold HII region, which can be difficult for conventional SRHD codes.

## 6.2 Limb-brightened jet

Most active galactic nuclei (AGN) jets in VLBI observations appear ridge-brightened, while limb-brightened jets are rare and have been reported only in a few nearby radio

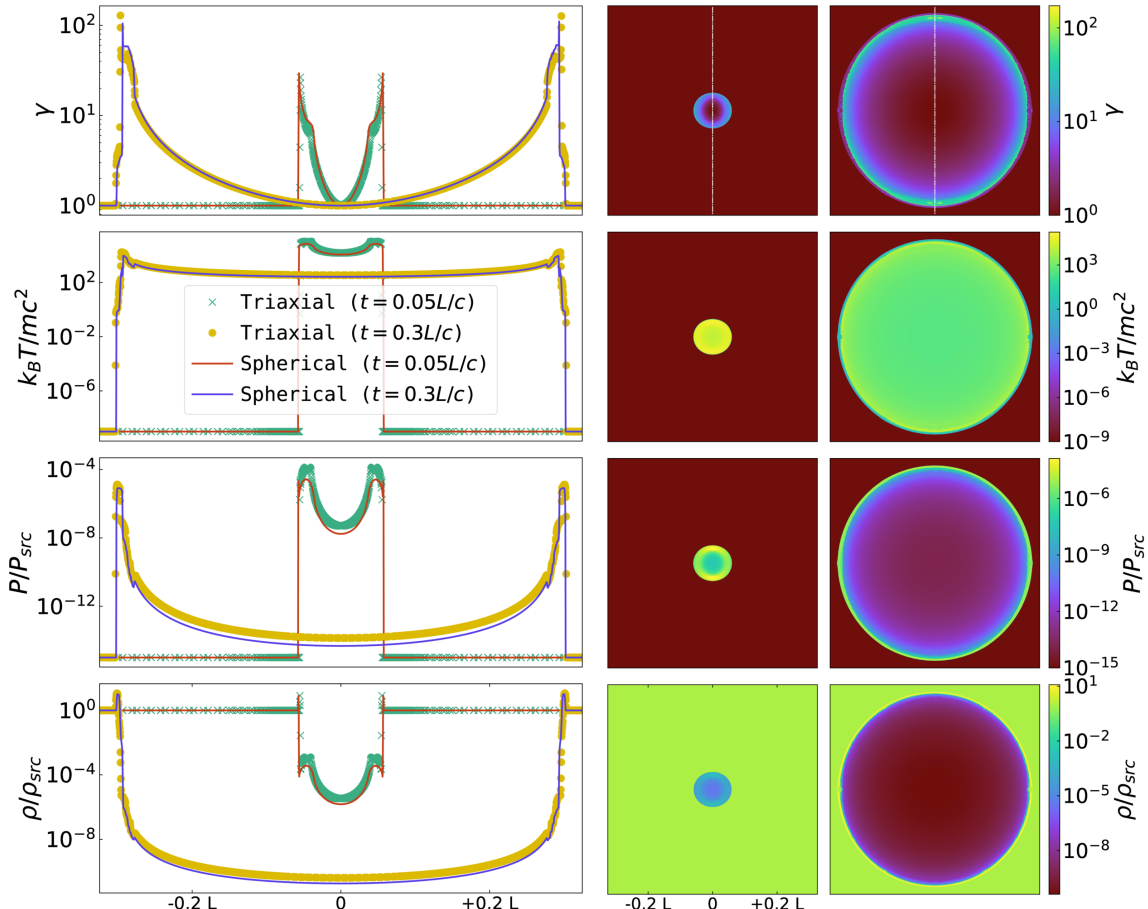


Figure 6.1: Triaxial blast wave test. The middle ( $t = 0.05L/c$ ) and right ( $t = 0.3L/c$ ) columns show the slices passing through the triaxial source at the mid-plane of its intermediate axis (i.e. the horizontal and vertical axes are along the major and minor axes, respectively). The left column shows the profiles along the minor-axis (i.e. the white dotted-dashed line in the  $\gamma$  map).

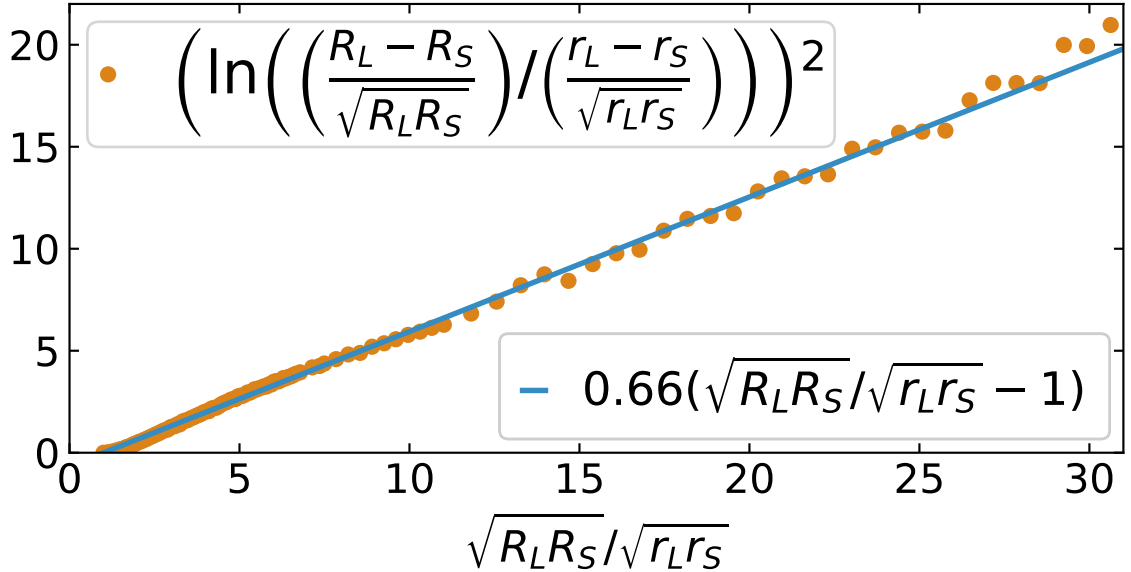


Figure 6.2: Damping of the triaxiality in the triaxial blast wave test, where  $R_L$  and  $R_S$  are the radii of the triaxial blast wave along the semi-major ( $r_L$ ) and semi-minor axes ( $r_S$ ) of the initial source.

galaxies, such as Mrk 501 (Giroletti et al., 2004), M87 (Asada & Nakamura 2012; Kim et al. 2018), Cygnus A (Boccardi et al., 2015), and 3C84 (Nagai et al. 2014; Giovannini et al. 2018). Motivated by these observations, we simulate a three-dimensional SRHD jet using `GAMER-SR` to study its acceleration and collimation in the hope to shed light on the limb-brightened jets.

We adopt the gradient of the reduced energy density and the magnitude of  $\mathbf{M}/D$  as the two inclusive refinement criteria. A patch is refined if any cell satisfies either Equation (4.3) with  $Q = \tilde{E}$  and  $C_Q = 0.1$  or  $\mathbf{M}/D > 20$ . The first criterion aims to capture the strong terminal shock and the cocoon, while the second one ensures that the central ‘spine’ region of the jet can be properly resolved.

The jet is continuously ejected from a cylindrical source with four-velocity  $\beta\gamma = 10.0$  ( $\gamma \sim 10.05$ ). The proper mass density ratio between the jet source and the ambient gases is set to 1.0. The temperature ( $k_B T/mc^2$ ) of the source and the ambient gases are set to 0.5 and  $10^{-5}$ , respectively. The outflow is thus an extremely under-pressured jet. Both the diameter and the length of the cylindrical source are well resolved by 32 cells.

Figure 6.3 shows the simulation results. It demonstrates that the jet flow is entirely confined by a turbulent cocoon at all time. Two points are worth noting from these

longitudinal slices. First, the Lorentz factor (first row) rises from 10 to 26, and meanwhile the temperature (second row) drops from 0.5 to 0.01 along the jet. Second, the relativistic Bernoulli number minus  $c^2$  (fifth row), defined as  $h\gamma - c^2$ , remains nearly constant within the spine region. According to the de Laval nozzle effect, these suggest that thermal energy is converted to kinetic energy by the expansion of a supersonic flow. Surprisingly, the gases are still accelerated in the region between the label ‘C’ and the confinement point close to ‘D’. These images seem to suggest acceleration during flow convergence, which in fact does not contradict the de Laval nozzle effect. The gases still expand away from the jet axis after passing ‘C’, which can be confirmed by examining the transverse slice of the radial component of the Mach number (the last row),

$$\mathcal{M}_{\text{radial}} = (\hat{\mathbf{r}} \cdot \mathbf{U}) / (c_s \gamma_s), \quad (6.2)$$

where  $\hat{\mathbf{r}}$  is the cylindrical unit radial vector,  $\mathbf{U}$  is the four-velocity of flow, and  $\gamma_s = c_s / \sqrt{1 - c_s^2}$ . The definition of the radial Mach number given by Equation (6.2) is Lorentz invariant when the transforming direction is along the jet. Obviously, gases expand not only between the jet source and ‘C’, but also inside the entire central spine region. Thus, the flow convergence in between ‘C’ and ‘D’ is a false impression.

Associated with this expanding jet flow is the limb-brightened phenomenon. Confined by the cocoon, the radial flow of the cooler jet imparts onto the cocoon with a boundary shock, as signified by the edge  $\mathcal{M}_{\text{radial}} \gg 1$ . Hot gases in the post-shock region then diffuse into the cocoon transverse to the jet through some instabilities composed of high-density and low-temperature fingers. This finger pattern is similar to that reported in Section 4.5.

Certainly the boundary shock can generate particle acceleration and produce extra synchrotron brightness at the jet edge, thus yielding limb brightening. Since the boundary shock is relatively weak, the extra synchrotron brightness cannot be immense. This may explain why limb brightening is mostly observed in nearby AGN jets.

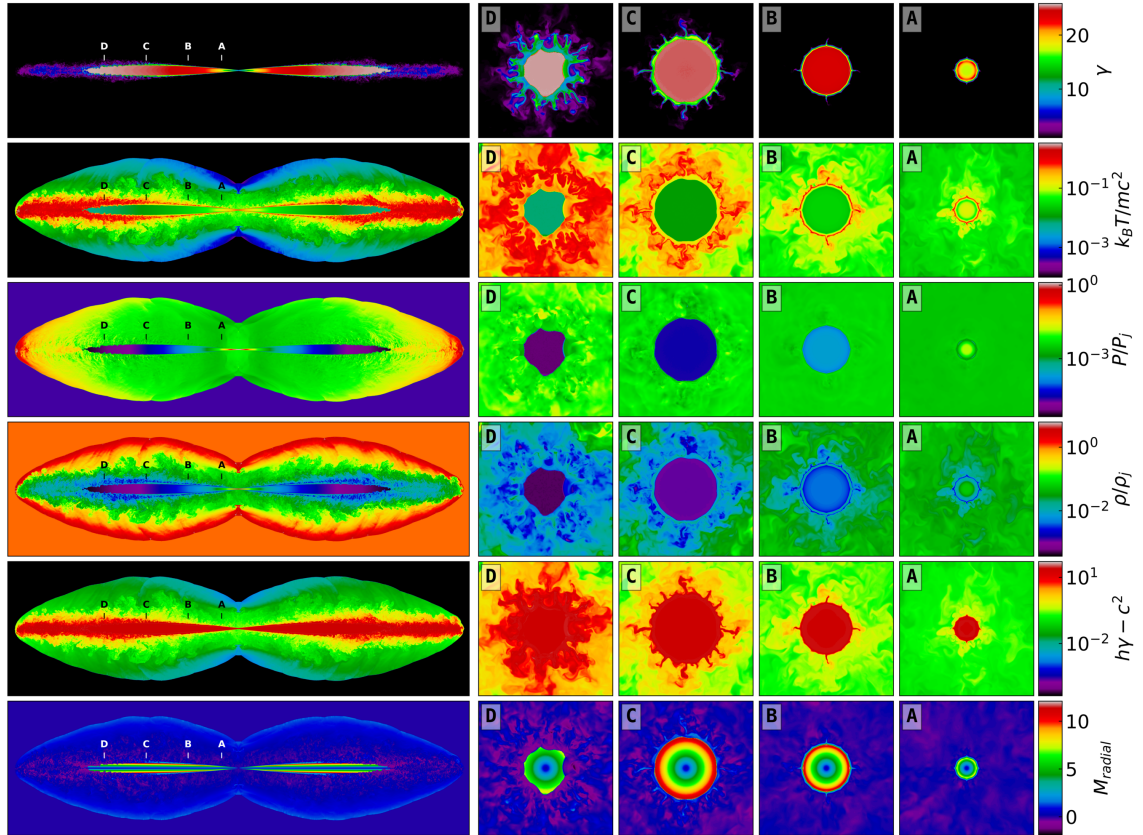


Figure 6.3: From top to bottom: Lorentz factor, temperature, pressure (normalized by the jet source pressure  $p_j$ ), proper mass density (normalized by the jet source density  $\rho_j$ ), relativistic Bernoulli number minus  $c^2$  (i.e.  $h\gamma - c^2$ ), and radial component of Mach number defined by Equation (6.2) at  $t = 0.73L/c$ . Left column: longitudinal slices passing through the jet source. Right four columns: transverse slices passing through the locations labelled by A, B, C, and D.

# Chapter 7

## Conclusions for part 1

In this paper, we have presented a novel special relativistic hydrodynamics code, `GAMER-SR`, which incorporates a new, well-tailored conversion scheme (cf. Figure 8.2) between primitive and conserved variables, together with the Taub-Mathews equation of state (TM EoS) covering both the ultra-relativistic and non-relativistic limits. The new scheme adopts the four-velocity  $U^j$ , the reduced energy density  $\tilde{E}$ , and the reduced enthalpy  $\tilde{h}$  to effectively avoid the catastrophic cancellation in subsonic flows at all finite temperature, including the particularly challenging low-temperature regime, with errors decreasing as  $\mathcal{M}^2 \epsilon_{\text{machine}}$  when  $\mathcal{M} \gg 1$ .

We have numerically derived the exact solution of a Riemann problem covering both extreme cold and ultra-relativistically hot gases with the TM EoS. Simulation results using our new scheme are in very good agreement with the exact solution in both the ultra-relativistic and non-relativistic regimes. (cf. Figure 4.3). In comparison, the catastrophic cancellation arising from the original (unoptimized) scheme can be much more severe than the truncation error in the non-relativistic limit, especially in the region swept by a traveling contact discontinuity.

The new scheme has been integrated into the code `GAMER` to facilitate the hybrid OpenMP/MPI/GPU parallelization and adaptive mesh refinement. Thanks to that, the performance of the root-finding iterations in the TM EoS can be significantly improved by GPU. The parallel efficiency using 2048 computing nodes is measured to be  $\sim 45$  per cent for strong scaling (cf. Figure 5.2) and  $\sim 75$  per cent for weak scaling (cf. Figure 5.3)

on the Piz-Daint supercomputer.

GAMER-SR has been demonstrated to be able to handle ultra-relativistic flow with a Lorentz factor as high as  $10^6$ . However, we also find that the Cartesian grids can lead to artificial dissipation when the direction of a high Mach number flow is not aligned with grids. This problem cannot be mitigated by increasing spatial and temporal resolution.

We have examined two astrophysical problems with coexisting relativistically hot and cold gases to demonstrate the power of GAMER-SR. The first problem deals with a relativistic blast wave with a triaxial source. Not only do we find that the code is able to capture the ultra-relativistic strong shock very well, but we also discover a simple rule governing how the triaxiality of the blast wave diminishes as a function of the blast wave radius.

The second problem addresses the flow acceleration and limb-brightening of a relativistic AGN jet. We find that the jet, from its head to its source, is always enclosed inside a turbulent cocoon. The jet is accelerated all the way up to the first confinement point, where an internal shock appears. We attribute such flow acceleration to the relativistic Bernoulli's law. In addition, the synchrotron limb-brightening is found to be caused by the jet transverse boundary shock, outside which the post-shock cosmic-ray particles are mixed with the turbulent cocoon and give out extra synchrotron emission.

GAMER-SR does not implement explicit grid derefinement criteria, dual-energy formalism, and magnetic fields (e.g., Stone et al. 2020). The magnetic fields play a critical role in many high energy astrophysical problems, such as the evolution of accretion discs (e.g., Blandford & Payne 1982), and the interaction between cosmic rays and thermal gases in the Fermi bubbles (e.g., Yang & Ruszkowski 2017). We leave them to future work.

# Chapter 8

## Appendix

Note that the speed of light, the particle mass, and the Boltzmann constant are set to unity in Appendix for simplicity.

### 8.1 Initial guess for Newton-Raphson iteration

We use the Newton-Raphson iteration to find the root  $\tilde{h}$  of Equation (2.15). The iteration requires the derivative of Equation (2.15) with respect to  $\tilde{h}$ :

$$\frac{df}{d\tilde{h}} = 2\tilde{h} + 2 - 2T - 2(\tilde{h} + 1) \frac{dT}{d\tilde{h}} + \frac{2T(\tilde{h} + 1)^4 \frac{dT}{d\tilde{h}} + 2T(\tilde{h} + 1) \left(\frac{\mathbf{M}}{D}\right)^2 \left[(\tilde{h} + 1) \frac{dT}{d\tilde{h}} + T\right]}{\left[(\tilde{h} + 1)^2 + \left(\frac{\mathbf{M}}{D}\right)^2\right]^2}, \quad (8.1)$$

where

$$\frac{dT}{d\tilde{h}} = \frac{4\tilde{h} + 4}{5\tilde{h} + 5 + \sqrt{9\tilde{h}^2 + 18\tilde{h} + 25}} - \frac{(2\tilde{h}^2 + 4\tilde{h}) \left( \frac{9\tilde{h} + 9}{\sqrt{9\tilde{h}^2 + 18\tilde{h} + 25}} + 5 \right)}{\left(5\tilde{h} + 5 + \sqrt{9\tilde{h}^2 + 18\tilde{h} + 25}\right)^2}, \quad (8.2)$$

follows from Equation (2.16).

The root-finding iteration also requires an initial guess of  $\tilde{h}_{\text{guess}}$ , for which we suggest the following procedure. In the low- $T$  limit, we Taylor expand Equation (2.15) in powers

of  $\tilde{h}$  and keep the first- and second-order terms:

$$\left(\frac{\tilde{E}}{D}\right)^2 + 2\left(\frac{\tilde{E}}{D}\right) - \left(\frac{\mathbf{M}}{D}\right)^2 = \frac{6}{5}\tilde{h} + \left\{ \frac{43}{125} + \frac{4}{25\left[1+\left(\frac{\mathbf{M}}{D}\right)^2\right]} \right\} \tilde{h}^2. \quad (8.3)$$

Solving Equation (8.3) for the unknown  $\tilde{h}$  gives the positive solution:

$$\tilde{h}_{\text{guess}} = \frac{\sqrt{125\left[1+\left(\frac{\mathbf{M}}{D}\right)^2\right]\left[43\left(\frac{\mathbf{M}}{D}\right)^2+63\right]\left[\left(\frac{\tilde{E}}{D}\right)^2+2\left(\frac{\tilde{E}}{D}\right)-\left(\frac{\mathbf{M}}{D}\right)^2\right]}}{\left[43\left(\frac{\mathbf{M}}{D}\right)^2+63\right]\left\{75\left[1+\left(\frac{\mathbf{M}}{D}\right)^2\right]+\sqrt{125\left[1+\left(\frac{\mathbf{M}}{D}\right)^2\right]\left[43\left(\frac{\mathbf{M}}{D}\right)^2+63\right]\left[\left(\frac{\tilde{E}}{D}\right)^2+2\left(\frac{\tilde{E}}{D}\right)-\left(\frac{\mathbf{M}}{D}\right)^2\right]+75^2\left[1+\left(\frac{\mathbf{M}}{D}\right)^2\right]^2}\right\}}. \quad (8.4)$$

In the opposite high- $T$  limit, Equation (2.15) can be reduced to

$$\left(\frac{\tilde{E}}{D}\right)^2 + 2\left(\frac{\tilde{E}}{D}\right) - \left(\frac{\mathbf{M}}{D}\right)^2 = \frac{9}{16}\tilde{h}^2, \quad (8.5)$$

which leads to

$$\tilde{h}_{\text{guess}} = \frac{4}{3}\sqrt{\left(\frac{\tilde{E}}{D}\right)^2 + 2\left(\frac{\tilde{E}}{D}\right) - \left(\frac{\mathbf{M}}{D}\right)^2}. \quad (8.6)$$

Equation (8.4) and Equation (8.6) provide two initial guesses for ‘cold’ and ‘hot’ gases, respectively. The threshold to distinguish between ‘cold’ gases and ‘hot’ gases is given by

$$\left\{ \frac{1800\left[1+\left(\frac{\mathbf{M}}{D}\right)^2\right]^2}{437\left(\frac{\mathbf{M}}{D}\right)^2+117} \right\}, \quad (8.7)$$

which is obtained by equating Equations (8.4) and (8.6) (see Figure 8.1). If  $(\tilde{E}/D)^2 + 2(\tilde{E}/D) - (\mathbf{M}/D)^2$  is greater than Equation (8.7), we choose Equation (8.6) as an initial guess for the Newton-Raphson iteration (hot gases); otherwise, we choose Equation (8.4) (cold gases).

## 8.2 Numerical error analysis for root-finding

Figure 8.2 provides a detailed flowchart of the conversion between primitive and conserved variables. Figure 8.3 demonstrates that the numerical errors of root-finding arising from

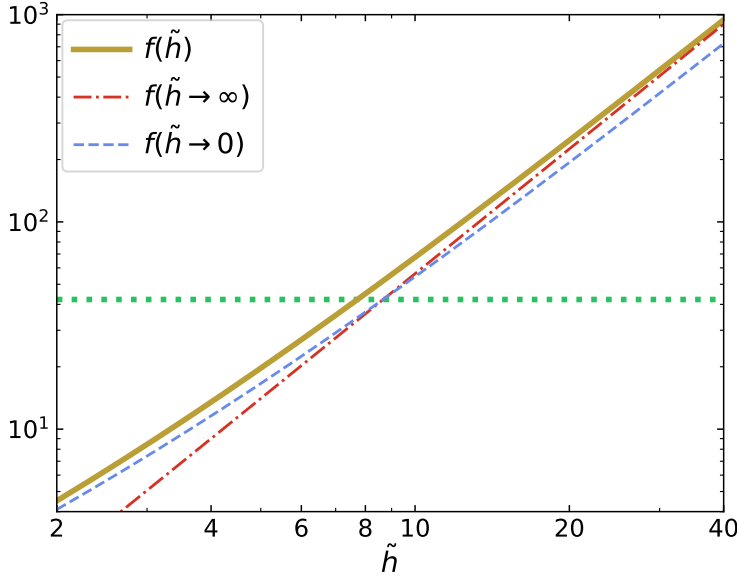


Figure 8.1:  $f(\tilde{h}; \mathbf{M}/D = 1)$  (brown solid line) and its asymptotes when  $\tilde{h} \rightarrow \infty$  (red dashed line) and  $\tilde{h} \rightarrow 0$  (blue dashed line). The horizontal line (green dashed line) is given by Equation 8.7, which passes through the intersection of two asymptotes and provides a threshold to distinguish between ‘cold’ and ‘hot’ gases for the initial guess of  $\tilde{h}$  in the Newton-Raphson iteration.

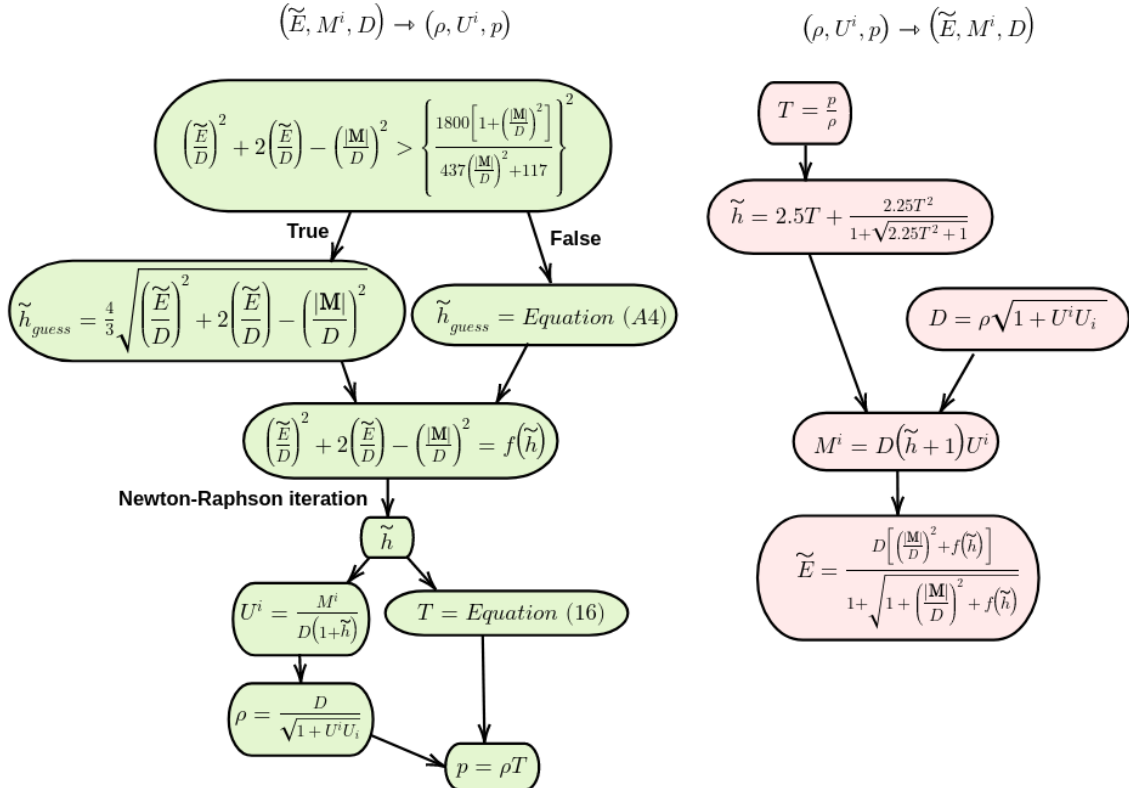


Figure 8.2: Flowchart of converting conserved variables to primitive variables (left) and the opposite (right).

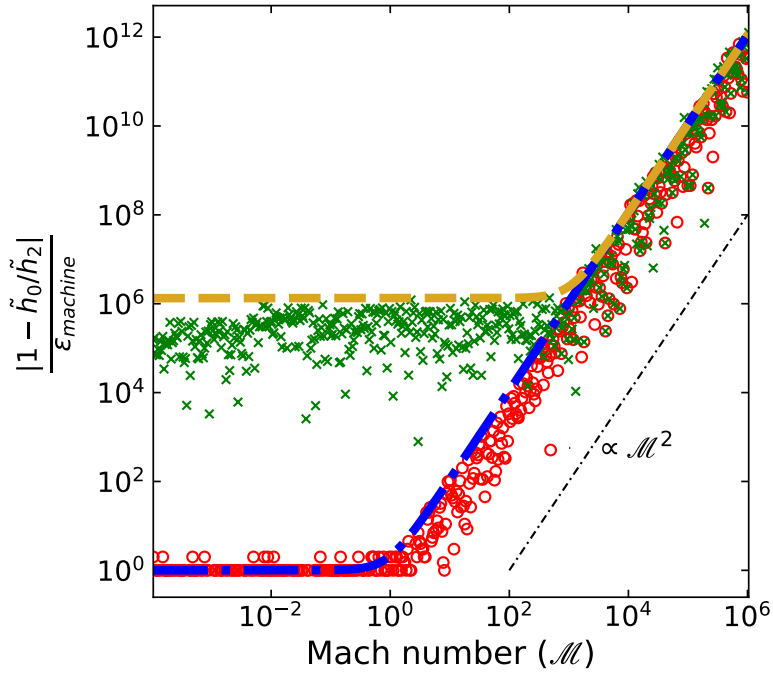


Figure 8.3: Numerical errors of the conversion between primitive and conserved variables. It shows the relative error  $|1 - \tilde{h}_0/\tilde{h}_2|$  as a function of Mach number with a given non-relativistic temperature ( $k_B T/mc^2 = 10^{-8}$ ) for the new scheme (red circles) and the original scheme (green crosses). These errors are mainly caused by the cancellation in  $(\tilde{E}/D)^2 + 2(\tilde{E}/D) - (\mathbf{M}/D)^2$  and  $(E/D)^2 - (\mathbf{M}/D)^2 - 1$ , which are inevitably introduced during the root-finding iteration and consistent with the predicted values given by Equation (2.20) (blue dashed-dotted line) and Equation (2.21) (brown dashed line).

the new and original conversion schemes are consistent with the predicted values given by Equation (2.20) and Equation (2.21). We measure this conversion error by first converting the input primitive variables  $(\rho_0, U_0^i, p_0)$  into conserved variables  $(D_1, M_1^i, \tilde{E}_1)$ . Next, we convert  $(D_1, M_1^i, \tilde{E}_1)$  back to  $(\rho_2, U_2^i, p_2)$  and then measure the relative error between  $\tilde{h}(p_0/\rho_0) := \tilde{h}_0$  and  $\tilde{h}(p_2/\rho_2) := \tilde{h}_2$ . Since the catastrophic cancellation is more prominent in the low- $T$  limit, we measure the error  $1 - \tilde{h}_0/\tilde{h}_2$  as a function of Mach number from  $10^{-4}$  to  $10^6$  with a fixed non-relativistic temperature  $k_B T/mc^2 = 10^{-8}$  (i.e. the blue dashed-dotted line in Figure 2.2). To verify the accuracy in three-dimensional space, we choose the direction of four-velocity to be parallel to the line  $x = y = z$  (i.e.  $U_0^i = \mathbf{U}_0/\sqrt{3}$  for all  $i$ ). Double precision is adopted to handle the large dynamic range. Figure 8.3 confirms that the numerical errors of the new and original schemes are mainly caused by round-off errors in the calculation of  $(\tilde{E}/D)^2 + 2(\tilde{E}/D) - (\mathbf{M}/D)^2$  and  $(E/D)^2 - (\mathbf{M}/D)^2 - 1$ , respectively.

## 8.3 Exact solutions of relativistic Riemann problems with the TM equation of state

To derive the exact solutions of relativistic Riemann problems with the TM EoS, we have generalized the previous framework of a constant polytropic EoS (Martí & Müller 1994; Rezzolla et al. 2001) to the TM EoS. More precisely, this approach can be applied to any EoS once we know the relationship between enthalpy and temperature. Here we only summarize the important equations and highlight salient differences from the polytropic EoS. We use the subscripts  $L/C_L/C_R/R$  to refer to the left/left-contact/right-contact/right regions and define the relative four-velocity of  $U_1$  with respect to  $U_2$  as  $\text{Relative}(U_1, U_2)$ . Note that we have replaced three-velocity with four-velocity again to avoid catastrophic cancellation in the ultra-relativistic limit.

The exact solution of a relativistic Riemann problem with the TM EoS can be obtained through the following three steps:

1. For a given initial condition, we can determine the wave pattern by comparing the relative velocity between the two unperturbed initial states with the three limiting values. These values mark the transition from one wave pattern to another and can be directly computed from the initial condition. See Rezzolla et al. (2001) for details.
2. We determine the unknown pressure  $p^*$  between the left and right waves by numerically solving

$$U_{LR} = \text{Relative}(U_{LC_L}(p^*), U_{RC_R}(p^*)), \quad (8.8)$$

where  $U_{LR} = \text{Relative}(U_L, U_R)$ ,  $U_{LC_L}(p^*) = \text{Relative}(U_L, U_{C_L}(p^*))$ , and  $U_{RC_R}(p^*) = \text{Relative}(U_R, U_{C_R}(p^*))$ . Note that the four-velocity in the left-/right-contact region,  $U_{C_{L/R}}$ , is different for each of the three possible wave patterns. For example, if the left wave is rarefaction and the right wave is shock, then  $U_{C_L} = U_{\mathcal{R}}(p^*)$  and  $U_{C_R} = U_{\mathcal{S}}(p^*)$  where  $U_{\mathcal{R}}(p^*)$  and  $U_{\mathcal{S}}(p^*)$  are defined as follows.

- (a)  $U_{\mathcal{R}}(p^*)$  represents the relation between pressure and flow four-velocity behind

the *rarefaction* wave:

Given the pressure behind the rarefaction wave (i.e.  $p^*$ ) during the Newton-Raphson iteration for solving Equation (8.8), we can determine  $U_{\mathcal{R}}(p^*)$  by numerically solving the system of equations (2.10), (2.14), (2.18), (8.9a), and (8.9b):

$$\frac{dU}{d\rho} = \pm \frac{c_s \gamma}{\rho}, \quad (8.9a)$$

$$\frac{p}{\rho^{5/3}}(h - T) = \text{constant}. \quad (8.9b)$$

Hereafter, the upper/lower sign applies to the right/left wave. The ordinary differential equation (8.9a), known as the Riemann invariant (Rezzolla & Zanotti, 2018), relates the dynamical ( $U$ ) and thermal ( $c_s$ ) quantities. Equation (8.9b), derived from Equation (2.10) and the second law of thermodynamics, results from the fact that entropy is constant through the rarefaction wave. The ‘constant’ in Equation (8.9b) is a function of entropy and can be determined by the thermal quantities in the region unperturbed by the rarefaction wave. In the case of the constant polytropic EoS, Equation (8.9b) reduces to a familiar form:  $p/\rho^\Gamma = \text{const.}$

- (b)  $U_{\mathcal{S}}(p^*)$  represents the relation between pressure and flow four-velocity behind the *shock* wave:

Let ‘up/down’ denote the upstream/downstream state of the shock wave. Under the condition that  $p_{\text{down}}$  ( $p_{\text{down}} = p^*$  in this case) is given during the Newton-Raphson iteration for solving Equation (8.8), we can compute  $h_{\text{down}}$  by numerically solving the jump condition of the enthalpy:

$$h_{\text{up}}^2 - h_{\text{down}}^2 = \left( \frac{h_{\text{down}}}{\rho_{\text{down}}} + \frac{h_{\text{up}}}{\rho_{\text{up}}} \right) (p_{\text{up}} - p_{\text{down}}). \quad (8.10)$$

Equation (8.10) is known as the Taub adiabat (Taub, 1948), where  $\rho_{\text{down}}$  can be eliminated using Equations (2.16) and (2.18). After determining  $h_{\text{down}}$  by

a root-finding routine, the mass flux across the shock can be calculated by

$$J = \left( \frac{p_{\text{down}} - p_{\text{up}}}{h_{\text{up}}/\rho_{\text{up}} - h_{\text{down}}/\rho_{\text{down}}} \right)^{0.5}. \quad (8.11)$$

The four-velocities of shock and post-shock then follow from

$$U_{\text{shock}} = \pm \left( \frac{J}{\rho_{\text{up}}} \right) \sqrt{1 + U_{\text{up}}^2} \pm U_{\text{up}} \sqrt{1 + \left( \frac{J}{\rho_{\text{up}}} \right)^2}, \quad (8.12)$$

and

$$U_{\mathcal{S}}(p^*) = \mp \left( \frac{J}{\rho_{\text{down}}} \right) \sqrt{1 + U_{\text{shock}}^2} + U_{\text{shock}} \sqrt{1 + \left( \frac{J}{\rho_{\text{down}}} \right)^2}, \quad (8.13)$$

respectively. Equations (8.12) and (8.13) are essentially the Lorentz boost that takes four-velocity from the shock rest frame to the lab frame. Note that the mass flux  $J$  is an invariant under the Lorentz boost in the flow direction.

3. Once  $p^*$  is known,  $\rho_{\text{down}}$  follows from Equations (2.16) and (2.18), which in turn allows for computing  $U_{\text{down}}$  and  $U_{\text{shock}}$  through Equation (8.12) and Equation (8.13). On the other hand,  $\rho$  behind the rarefaction wave follows from solving the system of equations (2.10), (2.18), and (8.9b). Finally, given the self-similar and isentropic character of the rarefaction wave,  $\rho$  and  $U$  within the rarefaction fan can be computed by solving the system of equations (8.9a) and  $U(\xi) = \text{Relative}(\xi/\sqrt{1-\xi^2}, \pm c_s/\sqrt{1-c_s^2})$ , where  $\xi = x/t$ .

On the basis of above procedure, we show in Table 8.1 the exact solution of the relativistic Riemann problem given in the last row of Table 4.1 with the TM EoS at  $t = 80.0$ . The source code is available at

(<https://github.com/zengbs/ExactSolutionRelativisticRiemannProblem>).

Table 8.1: Exact solution of a relativistic Riemann problem with the TM EoS at  $t = 80.0$ . Columns from left to right give  $x$ -coordinate, proper mass density, four-velocity, and pressure. The initial condition is given in the last row of Table 4.1, with the initial discontinuity at  $x = 5 \times 10^{-2}$ . The blue solid line in Figure 4.3 plots the solution. The exact solution is calculated with double precision and shown in 16 digits to reach machine accuracy. The data are available in the supplement.

$x$	$\rho$	$U_x$	$p$
0.00000000000000e+00	1.00000000000000e+02	+1.00000000000000e-03	1.00000000000000e-04
2.5743971630613077e-02	1.00000000000000e+02	+1.00000000000000e-03	1.00000000000000e-04
2.6720534130613077e-02	9.99999999999998e+01	+1.00000000000000e-03	1.00000000000000e-04
2.8673659130613080e-02	9.8588362795909134e+01	+1.0183105709873300e-03	9.7658360819209613e-05
3.1603346630613080e-02	9.6495914226915929e+01	+1.0457764274335814e-03	9.4228343648087098e-05
3.6486159130613087e-02	9.3074657510006034e+01	+1.0915528549894106e-03	8.8726314406083176e-05
4.2345534130613087e-02	8.9077088828567909e+01	+1.1464845688462534e-03	8.2466343818876140e-05
5.2111159130613087e-02	8.2671707042031258e+01	+1.2380374291888151e-03	7.2821829638494934e-05
6.4806471630613094e-02	7.4813960019366874e+01	+1.3570561601099081e-03	6.1655409508574801e-05
8.4337721630613108e-02	6.3723430244968533e+01	+1.5401619444173906e-03	4.7188055213551995e-05
1.1168147163061304e-01	5.0121316453652021e+01	+1.7965101817141935e-03	3.1625521037347636e-05
1.5172053413061287e-01	3.3922515604881056e+01	+2.1718776864619303e-03	1.6499866085321606e-05
2.0836115913061276e-01	1.7591444669719621e+01	+2.7028867092515813e-03	5.5229310921865207e-06
2.0933772163061276e-01	1.7369735883307754e+01	+2.7120420544404751e-03	5.4074080094554571e-06
2.0972078270771960e-01	1.7283280852025452e+01	+2.7156332803617649e-03	5.3626249948767070e-06
2.6627329885804002e-01	1.7283280852025452e+01	+2.7156332803617649e-03	5.3626249948767070e-06
2.6724986145813656e-01	4.0108528993879889e-10	+2.7156332816129858e-03	5.3626249948767070e-06
2.6909288248391281e+01	4.0108528993879889e-10	+2.7156332816129858e-03	5.3626249948767070e-06
2.6910264810891281e+01	9.999999999999998e-13	-1.000000000000000e+02	1.000000000000000e-10
1.00000000000000e+02	9.999999999999998e-13	-1.000000000000000e+02	1.000000000000000e-10

## **Part II**

The *Fermi* and eROSITA bubbles



# Chapter 9

## Brief review of the *Fermi*/eROSITA bubbles

The detection of the *Fermi* bubbles (Su & Finkbeiner, 2012; Ackermann et al., 2014; Narayanan & Slatyer, 2017), two large bubbles symmetrically extending about 50 degrees above and below the Galactic plane, is one of the great discoveries of the *Fermi* Large Area Telescope (Atwood et al., 2009). The gamma-ray emission of the *Fermi* bubbles is observed in the energy range of  $\sim$ 1–100 GeV and has an almost spatially uniform hard spectrum, sharp edges and an approximately flat brightness distribution (see Yang et al. 2018 for a review). Recently, the newly launched eROSITA (Predehl et al., 2021) conducted an all-sky X-ray survey with high-spatial resolution and revealed two gigantic bubbles (eROSITA bubbles hereafter) extending to  $\sim$  80 degrees in Galactic latitudes, corresponding to an intrinsic size of 14 kpc across (Predehl et al., 2020). The remarkable resemblance between the eROSITA and *Fermi* bubbles suggest that they likely share the same origin (Yang et al., 2022). Their symmetry about the GC further suggests that these Galactic bubbles may be generated by powerful energy injections from the GC, possibly related to nuclear star formation (Crocker & Aharonian, 2011; Carretti et al., 2013; Crocker et al., 2015; Sarkar et al., 2015) or past AGN activity (Guo & Mathews, 2012; Guo et al., 2012; Yang et al., 2012, 2013; Mou et al., 2014; Yang & Ruszkowski, 2017). The latter scenario is what we will focus on in this work.

Previous attempts (Guo & Mathews, 2012; Yang et al., 2012; Zhang & Guo, 2020) to model the formation of the symmetric Galactic bubbles by AGN jets have typically assumed that the jets are vertical to the Galactic plane. While there are some observational indications of pc-scale jets from Sgr A\* that are found to be perpendicular to the Galactic plane (Li et al., 2013; Zhu et al., 2019), generally speaking, the AGN jet orientation is determined by the black hole spin and the accretion disk in the black-hole vicinity and does not need to align with the rotational axis of the host galaxy. Indeed, observationally there is a lack of evidence for the alignment between AGN jets and the disk normal (e.g., Gallimore et al., 2006). The jets are often oblique to the disk normal (e.g. NGC 3079, Cecil et al. 2001; NGC 1052, Dopita et al. 2015), and there are even cases in which the jets lie in the plane of the disk (e.g. IC 5063, Morganti et al. 2015).

To this end, the aim of this work is to remove the assumption on jet orientations in the AGN jet models by introducing a dense, thin ISM disk that can interact with the central oblique jet, in an attempt to resolve the symmetry problem of the Galactic bubbles. More specifically, we use 3D SRHD simulations involving CR jet injections from the central supermassive black hole (SMBH) in the Galaxy to investigate whether the *oblique* jet scenario is able to produce the *symmetric* Galactic bubbles. We will verify whether the oblique jet model is consistent with the observed features of the Galactic bubbles, including the shape, surface brightness, and spectra of the *Fermi* bubbles (Ackermann et al., 2014) and microwave haze (Dobler & Finkbeiner, 2008; Ade et al., 2013).

This paper is organized as follows. In Section 10, we describe the numerical techniques and initial conditions employed. In Section 11, we first present characteristics of our simulated Galactic bubbles, and then discuss how the disk affects the formation of the bubbles. We compare the morphology and profiles of the simulated eROSITA bubbles with the observed X-ray map in Section 11.2, and present the simulated and observed multi-wavelength spectra of the *Fermi* bubbles and microwave haze in Section 11.3. Finally, the summary and implications of our findings are given in Section 13.

# Chapter 10

## Methodology

We use the GPU-accelerated SRHD adaptive-mesh-refinement (AMR) code `GAMER-SR` developed at the National Taiwan University (Schive et al. 2010, 2018; Tseng et al. 2021) to carry out the simulations of the Galactic bubbles formed by CR and relativistic-fluid injections from the GC.

The governing equations solving the special relativistic ideal fluid including CR advection, and dynamical coupling between the thermal gas and CRs without CR diffusion can be written in a succinct form as

$$\partial_t D + \partial_j (D U^j / \gamma) = 0, \quad (10.1a)$$

$$\partial_t M^i + \partial_j (M^i U^j / \gamma + p_{\text{total}} \delta^{ij}) = -\rho \partial_i \Phi, \quad (10.1b)$$

$$\partial_t \tilde{E} + \partial_j [(\tilde{E} + p_{\text{gas}}) U^j / \gamma] = 0, \quad (10.1c)$$

$$\partial_t (\gamma e_{\text{cr}}) + \partial_j (e_{\text{cr}} U^j) = -p_{\text{cr}} \partial_j U^j, \quad (10.1d)$$

where the five conserved quantities of gas  $D$ ,  $M^i$ , and  $\tilde{E}$  are the mass density, the momentum densities, and the reduced energy density, respectively. The reduced energy density is defined by subtracting the rest mass energy density of gas from the total energy density of gas.  $\gamma$  and  $U^j$  are the temporal and spatial component of four-velocity of gas.  $\rho$  is the gas density in the local rest frame defined by  $D/\gamma$ .  $p_{\text{gas}}$  is the gas pressure.  $p_{\text{cr}}$  and  $e_{\text{cr}}$  are the CR pressure and CR energy density measured in the local rest frame.  $p_{\text{total}}$

is the sum of  $p_{\text{gas}}$  and  $p_{\text{cr}}$ . Note that we simply replace  $p_{\text{total}}$  by  $p_{\text{gas}}$  in this paper as we have assumed  $p_{\text{cr}} \ll p_{\text{gas}}$ .  $\Phi$  is a gravitational potential.  $c$  is the speed of light, and  $\delta^{ij}$  is the Kronecker delta notation. Throughout this paper, Latin indices run from 1 to 3, except when stated otherwise. The set of Eq. 10.1 is closed by using the Taub-Mathews equation of state (EoS; Taub, 1948; Mathews, 1971) that approximates the exact EoS (Synge, 1957) for ultra-relativistically hot gases coexisting with non-relativistically cold gases.

**GAMER-SR** adopts a new SRHD solver (Tseng et al., 2021), which significantly reduce numerical errors in non- and ultra-relativistic limits caused by catastrophic cancellations in the conversion between primitive ( $\rho$ ,  $U^j$ ,  $p$ ) and conserved variables ( $D$ ,  $M^j$ ,  $\tilde{E}$ ). **GAMER-SR** also adaptively and locally reduce the min-mod coefficient (Tseng et al., 2021) within the failed patch group rarely occurring in the SRHD solver, new patches allocations, and ghost-zone interpolations. In this manner, we provide an elegant approach to avoid the use of pressure/density floor, being unnatural but widely used in almost publicly available codes.

In order to track the evolution of CRs injected by the AGN jets and make predictions of the non-thermal radiation they produce, we adopt the CR hydrodynamic formalism and model the CRs as a second fluid (Zweibel, 2013). The approach is similar to previous works of Guo & Mathews (2012) and Yang et al. (2012), but generalized to CRs that couple with thermal gas moving with relativistic speeds. The detailed implementations in **GAMER-SR** and tests of the algorithm can be found in a forthcoming paper (Chen et al. in prep). In this approach, the CRs are treated as a single species without distinctions between CR electrons and protons, and the CR energy density  $e_{\text{cr}}$  is evolved according to Eq. 10.1d. The CRs are advected with the thermal gas and can have adiabatic compression and expansion with the gas. Also, we do not simulate the spectral evolution of the CRs and assume that the CR-to-gas pressure ratio is much less than 1 so that the contribution of CR pressure gradient to the momentum of the gas can be ignored (we will see that the ratio is around 0.1–0.2 throughout the simulations). Therefore, in the simulations we have neglected the cooling of CRs because it should have a negligible impact on the overall dynamics.

As stressed by Yang et al. (2012), CR diffusion with a canonical diffusion coefficient of  $\kappa \sim 3 \times 10^{28} \text{ cm}^2 \text{ s}^{-1}$  in the Galaxy has a minor effect on the overall morphology of the *Fermi* bubbles as it only acts to smooth the CR distributions on the scales of  $l \sim \sqrt{\kappa t} \sim 0.3 (t/1\text{Myr}) \text{ kpc}$ . Including anisotropic CR diffusion can also help to sharpen the edges of the bubbles due to interplay between the magnetic field and anisotropic CR diffusion with suppressed perpendicular diffusion across the bubble surface. As for the magnetic field, Yang et al. (2013) has found that the magnetic field within the *Fermi* bubbles needs to be amplified to comparable values to the ambient field in order to reproduce the microwave haze emission. We thus directly adopt the exponential model for the magnetic field distribution in our calculation for the haze (see descriptions in Section 10.1). For the above reasons, we have ignored CR diffusion and the magnetic field in the simulations.

## 10.1 The Galactic and Disk Models

As a proof-of-concept study, we approximate conventionally axisymmetric stellar potential of Milky Way by a plane-parallel potential that is symmetric about the Galactic plane,  $z = 0$ , in a simulation domain of  $14 \times 14 \times 28 \text{ kpc}$ , slightly larger than the size of eROISTA bubbles. The plane-parallel potential is fixed throughout our simulations and given by

$$\Phi_{\text{total}}(z) = \Phi_{\text{bulge}}(z) + \Phi_{\text{halo}}(z), \quad (10.2)$$

where

$$\Phi_{\text{bulge}}(z) = 2\sigma_{\text{bulge}}^2 \ln \cosh \left( z \sqrt{\frac{2\pi G \rho_{\text{bulge}}^{\text{peak}}}{\sigma_{\text{bulge}}^2}} \right) \quad (10.3)$$

is the potential of an isothermal slab mainly contributed by stars around the Galactic bulge, and  $\Phi_{\text{halo}}(z) = v_{\text{halo}}^2 \ln(z^2 + d_{\text{h}}^2)$  is a plane-parallel logarithmic dark halo potential.

With the isothermal assumption and the condition of hydrostatic equilibrium within the total potential of the disk and halo, as well as pressure equilibrium between the isothermal

disk and the halo gas, we can write down the steady-state gaseous density distribution as

$$\rho_{\text{isoDisk}}(z) = \rho_{\text{isoDisk}}^{\text{peak}} \exp \left[ -\frac{\Phi_{\text{total}}(z)}{k_B T_{\text{isoDisk}}/m_p} \right] \quad (10.4a)$$

, if  $|z| < z_0$ ,

$$\rho_{\text{atmp}}(z) = \rho_{\text{atmp}}^{\text{peak}} \exp \left[ -\frac{\Phi_{\text{total}}(z)}{k_B T_{\text{atmp}}/m_p} \right] \quad (10.4b)$$

, otherwise,

where  $m_p$  is the proton mass,  $T_{\text{isoDisk}}$  and  $T_{\text{atmp}}$  are the temperature of the isothermal disk and the ambient atmosphere, and  $\rho_{\text{isoDisk}}^{\text{peak}}$  and  $\rho_{\text{atmp}}^{\text{peak}}$  are the peak density of the disk and the atmosphere at  $z = 0$ , respectively.

We tabulate parameters adopted for the Galactic model in Table 10.1, except for  $\rho_{\text{atmp}}^{\text{peak}}$  that can be derived from the other known parameters and the pressure equilibrium condition at the interfaces ( $z = \pm z_0$ ) between the disk and the atmosphere. The density profile of Eq. 10.4 is shown in Fig. 10.1. Beyond the core radius ( $\sim 2$  kpc) the gas density decreases rapidly as a power-law.

To compute the predicted synchrotron radiation as a function of position, we adopt the default exponential magnetic field in **GALPROP** (Strong et al., 2007) that obeys the following spatial dependence:

$$|\mathbf{B}(R, z)| = B_0 \exp \left[ -\frac{z}{z_0} \right] \exp \left[ -\frac{R}{R_0} \right], \quad (10.5)$$

where  $R = \sqrt{x^2 + y^2}$ ,  $B_0$  is the average field strength at the GC, and  $z_0$  and  $R_0$  are the characteristic scales in the vertical and radial directions, respectively. We adopt  $z_0 = 2$  kpc and  $R_0 = 10$  kpc, which are best-fitting values in the **GALPROP** model to reproduce the observed large-scale 408 MHz synchrotron radiation in the Galaxy. We choose  $B_0 = 50$   $\mu\text{G}$  based on the observed field strength at the GC (Crocker et al., 2010).

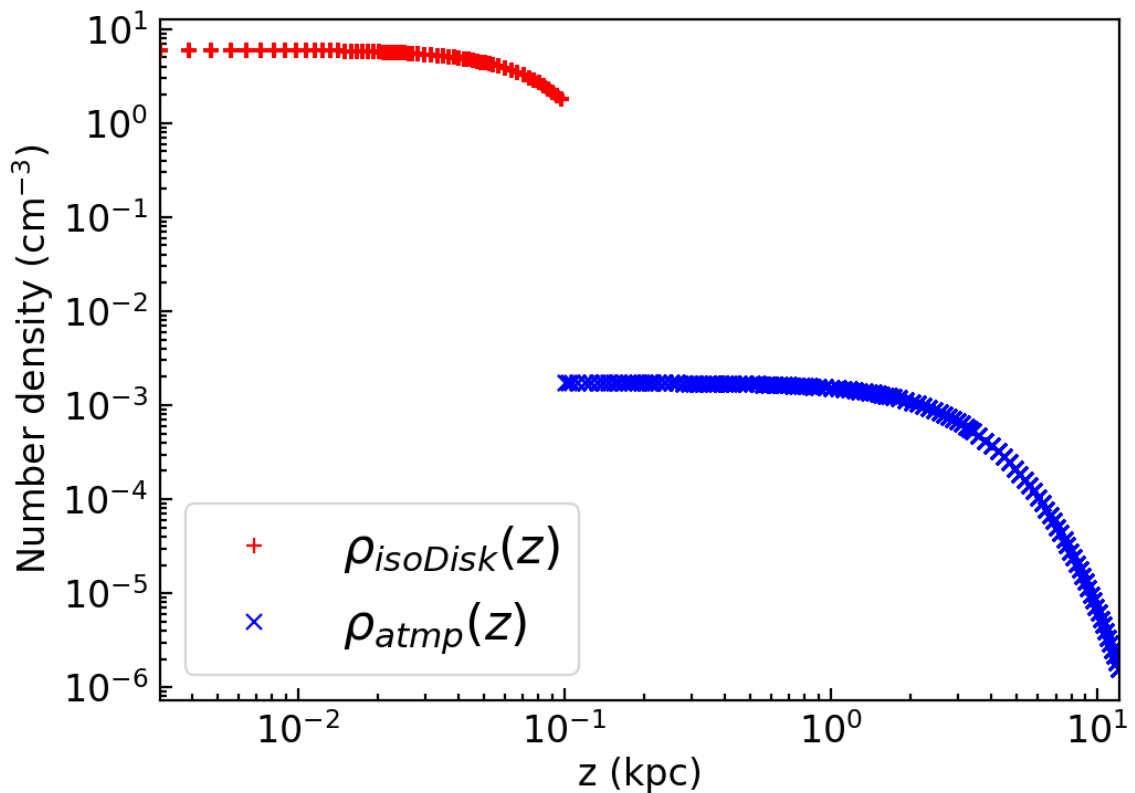


Figure 10.1: The density profile of the isothermal disk (red pluses) and the ambient atmosphere (blue crosses) along the positive  $z$ -axis. The density distribution is derived from the condition of hydrostatic equilibrium. The gas at the interface between the isothermal disk and the atmosphere at  $z = 0.1$  is in pressure equilibrium.

## 10.2 The Clumpy Multiphase Interstellar Medium

A crucial component in our work is the clumpy ISM disk initialized by the publicly available pyFC code <sup>1</sup>. pyFC randomly generates dimensionless 3D scalar field  $f(\mathbf{x})$  that obeys the log-normal probability distribution with mean  $\mu$  and dispersion  $\sigma$ , and follows the power-law Kolmogorov spectrum

$$D(\mathbf{k}) = \int k^2 \hat{f}(\mathbf{k}) \hat{f}^*(\mathbf{k}) d\Omega \propto k^{-\delta}, \quad (10.6)$$

where  $\hat{f}(\mathbf{k})$  is the Fourier transform of  $f(\mathbf{x})$ . The spectrum  $D(\mathbf{k})$  in the Fourier space is characterized by a power-law index  $\delta = 5/3$ , a Nyquist limit  $k_{\max}$ , and a lower cutoff wave number  $k_{\min}$ .  $k_{\max}$  is one-half of the spatial resolution within the disk, and  $k_{\min}$  is 375.0, corresponding to the maximum size of an individual clump of  $\sim 20$  pc. Lewis & Austin (2002) and Wagner et al. (2012) have outlined a detailed procedure for constructing a clumpy scalar field, and we refer the readers for more information.

The density of the clumpy disk can then be obtained by taking the scalar products of  $f(\mathbf{x})$  with  $\rho_{\text{isoDisk}}(z)$  over all cells within the disk, i.e.,  $\rho_{\text{ismDisk}}(\mathbf{x}) = f(\mathbf{x})\rho_{\text{isoDisk}}(z)$ . Also, the thermal pressure equilibrium within the clumpy disk implies that the temperature of the disk is  $T_{\text{ismDisk}}(\mathbf{x}) = T_{\text{isoDisk}}(z)\rho_{\text{isoDisk}}(z)/\rho_{\text{ismDisk}}(\mathbf{x})$ . The last category in Table 10.1 summarizes the parameters of the clumpy disk and their references.

On the basis of this setup, we cover the AMR base level with  $16 \times 16 \times 32$  root cells, refined progressively on the mid-plane at  $z = 0$  based on the gradient of density. We also restrict the refinement level at 7 within the disk so that a molecular cloud can be adequately resolved by approximately 30 cells along their diameter of 20 pc. We plot the volume filling factor as a function of initial number density within the disk without the jet source in Fig. 10.2, and show a close-up view of the pressure, temperature, and number density slices in the  $y - z$  plane through the center of the disk in Fig. 10.3.

---

<sup>1</sup><https://pypi.python.org/pypi/pyFC>

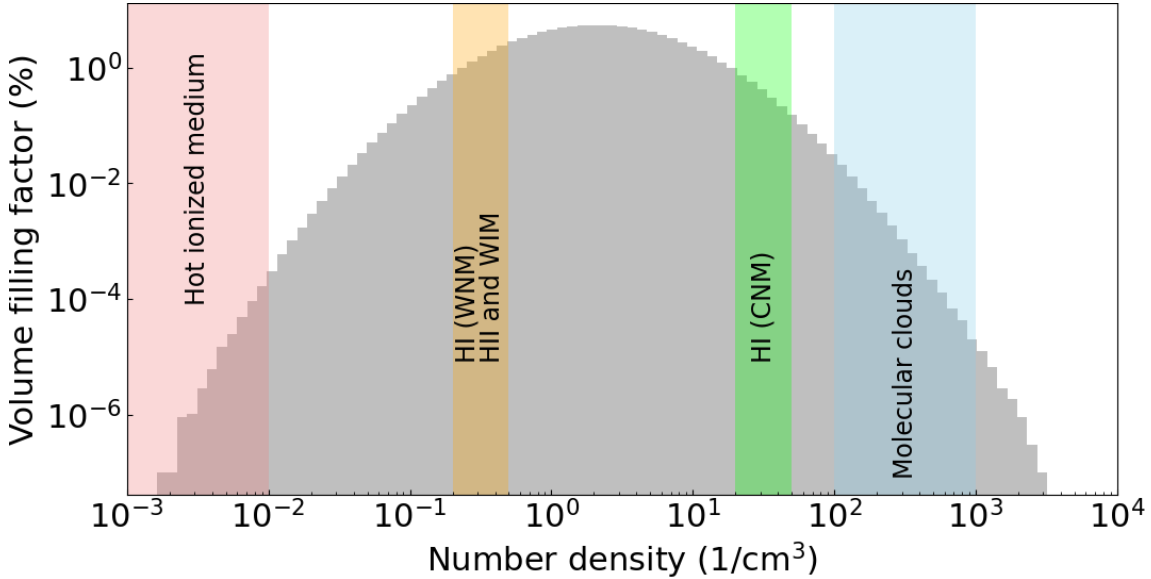


Figure 10.2: The volume filling factor as a function of initial number density within the disk without the jet source. The vertical bands from left to right depict the allowable number densities (Ferrière, 2001) for hot ionized, warm neutral (WNM), warm ionized (WIM), cold neutral mediums (CNM), and molecular clouds.

Table 10.1: Parameters of the disk, atmosphere, and gravitational potential in the simulations.

Parameter	Description	Value	Reference
<b>Static stellar potential</b>			
$\sigma_{\text{bulge}}^{\text{peak}}$	Velocity dispersion of bulge	100 km s <sup>-1</sup>	(Valenti et al., 2018)
$\rho_{\text{bulge}}^{\text{peak}}$	Peak average density of bulge	$4 \times 10^{-24}$ g cm <sup>-3</sup>	N/A
<b>Static dark halo potential</b>			
$v_{\text{halo}}$	Characteristic velocity	131.5 km s <sup>-1</sup>	(Johnston et al., 1995)
$d_h$	Core radius	12 kpc	"
<b>Atmosphere</b>			
$T_{\text{atmp}}$	Temperature of atmosphere	$10^6$ K	(Tepper-García et al., 2018)
<b>Isothermal disk</b>			
$z_0$	Scale height of disk	100 pc	(Ferrière, 2001)
$T_{\text{isoDisk}}$	Temperature of disk	$10^3$ K	"
$\rho_{\text{isoDisk}}^{\text{peak}}$	Peak density of disk	$10^{-23}$ g cm <sup>-3</sup>	"
<b>Clumpy disk</b>			
$k_{\min}^{\dagger}$	Cutoff wave number	375.0	(Ferrière, 2001)
$\mu$	Mean of scalar field	1.0	N/A
$\sigma^{\ddagger}$	Dispersion of scalar field	5.0	(Federrath et al., 2010)
$\delta$	Power law index	-5/3	N/A

†  $k_{\min} = 375.0$  leads to the size of an individual molecular cloud of  $\sim 100$  pc.

‡ In numerical simulations of turbulence, Federrath et al. (2010) find  $\sigma \sim 3.6$  and 35 for solenoidal (divergence-free) and compressive (curl-free) driving force, respectively, so that our adopted value of 5 is closer to their solenoidal result.

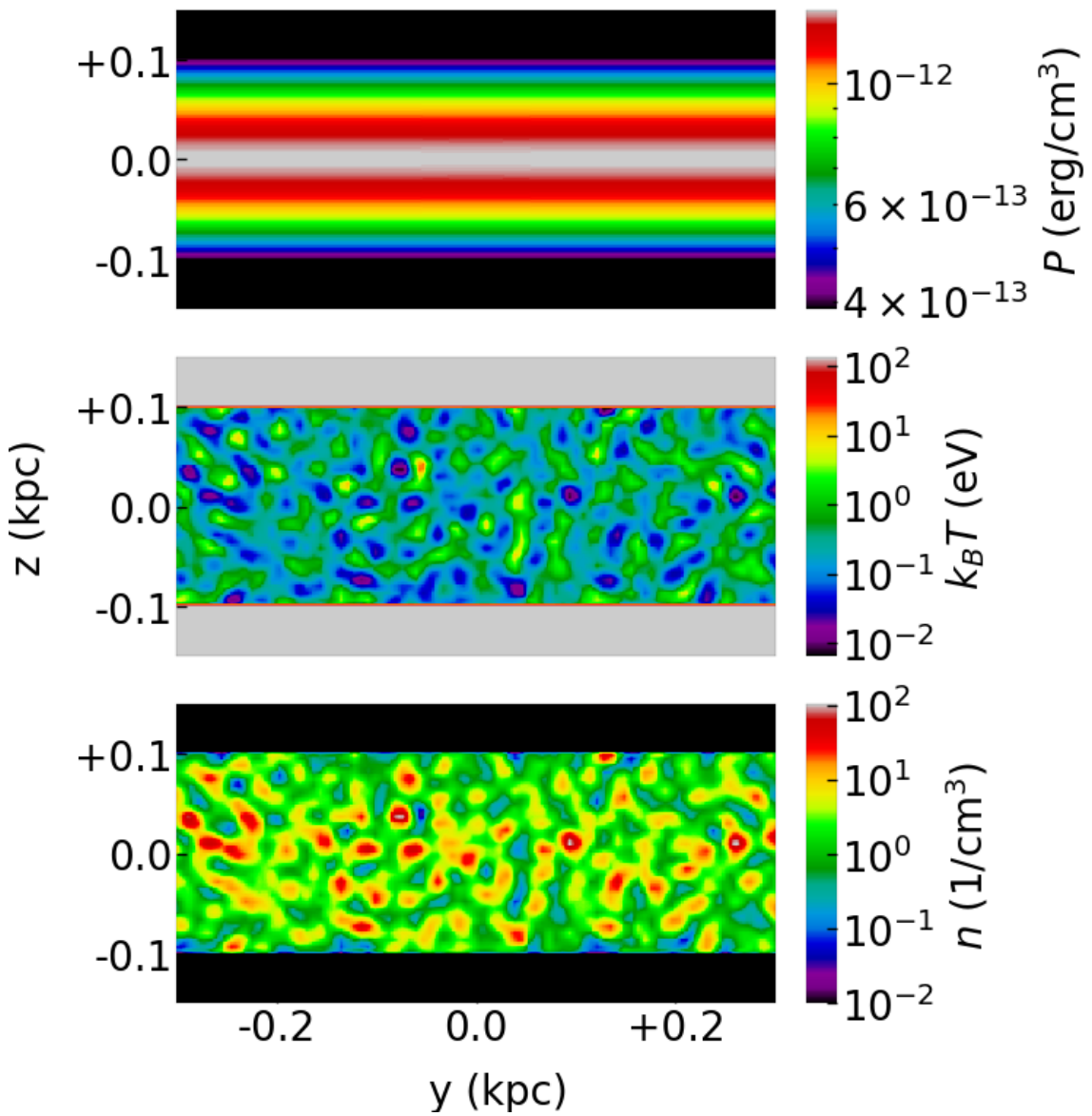


Figure 10.3: Close-up view of the initial pressure (top), temperature (middle), and number density (bottom) slices in the  $y - z$  plane through the center of the disk.

## 10.3 Oblique jets

We simulate the jets emanating from the GC with an inclination angle  $45^\circ$  with respect to the Galactic plane in order to alleviate the constraint that the jet direction must be perpendicular to the Galactic plane, and in particular to investigate how the dense disk affects the bubble formation.

We use the following quantities to characterize the jets: the density contrast between the thermal gas contained in the jet source and the ambient gas,  $\rho_{\text{jet}}/\rho_{\text{amb}} = 10^{-3}$ , the temperature contrast,  $T_{\text{jet}}/T_{\text{amb}} = 2 \times 10^4$ , the CR-to-gas pressure ratio of 0.18, and the flow 4-velocity ( $\beta\gamma = 0.6$ ) inside the jet source along the jet axis. The jet power is thus  $3.2 \times 10^{42} \text{ erg s}^{-1}$ , resulting in an Eddington ratio of 0.008. Note that since we inject the jets at the center of the clumpy disk, we define the atmosphere gas density by the peak density of the isothermal disk on the mid-plane  $z = 0$  (i.e.  $\rho_{\text{isoDisk}}^{\text{peak}}$ ), as opposed to the *clumpy* density around the jet source.

The bipolar jets are constantly ejected from a cylindrical source starting from the beginning of simulation ( $t = 0$ ) and suddenly quenched at  $t = 1.2 \text{ Myr}$  before fully breaking out the disk. Without quenching, the Galactic bubbles at the present time would be asymmetric about the Galactic plane. The jet duration allows the total ejected energy to be  $1.2 \times 10^{56} \text{ erg}$ , within the range of enclosed energy estimated by Predehl et al. (2020) between  $8 \times 10^{55} \text{ erg}$  and  $1.3 \times 10^{56} \text{ erg}$ .

The diameter and height of cylindrical source are 4 pc, leading to a source volume ( $\sim 50 \text{ pc}^3$ ) much smaller than that of an individual clump by a factor of  $\sim 83$ . By intentionally reducing the volume ratio of the jet source to an individual clump, we can mitigate the effect of the randomness of the clumps on the bubbles. Moreover, we resolve the jet source with the highest refinement level of 11, bringing the finest spatial resolution up to 0.4 pc.



# Chapter 11

## Results

### 11.1 Morphology and properties of Galactic bubbles

Fig. 11.5 shows the slices of pressure (top), temperature (middle), number density (bottom) at the end of simulation  $t = 12.39$  Myr. The slices pass through the bipolar jet source injecting along  $z = -y$  direction.

The fiducial run (Fig. 11.1) with the initial condition specified in Section 10 shows that the edge of the outermost bubbles is a forward shock, expanding to 12.5 kpc above and below the Galactic plane, with a semiminor axis about 6.8 kpc on the plane. The overall extent of the outermost bubbles is comparable to the two spherical objects of a radius of 6-7 kpc estimated by Predehl et al. (2020) for modeling the eROSITA bubbles. The temperature profile (left middle panel in Fig. 11.6) along the positive  $z$ -axis in Fig. 11.5 indicates that the temperature of the smooth region (purple band in Fig. 11.6) is around 0.3-0.5 keV, similar to 0.3 keV observed by Miller & Bregman (2016) and Kataoka et al. (2018a).

Followed by the forward shock is a turbulent and hot plasma extending to a height of  $\sim 8$  kpc (Fig. 11.6). The extent of the turbulent plasma approximately agrees with that of the observed *Fermi* bubbles (Su et al., 2010). Also, the temperature of the plasma is around 2 keV, comparable to few keV inside the *Fermi* bubbles estimated by observing X-ray absorption lines through the hot gaseous halo along many different sight lines in the sky (Miller & Bregman, 2013). We also note that the turbulent, hot plasma is in pressure

balance with the external medium, suggesting the outer edge of the *Fermi* bubbles is a contact discontinuity rather than a shock (Zhang & Guo, 2020).

An interesting feature found in our simulations is that there are a pair of innermost bubbles (dashed box in the top panel of Fig. 11.1) extending out from the GC on either side of the thin disk. The innermost bubbles are cold (1–10 eV), dense ( $10^{-4}$ – $10^{-2}$  cm $^{-3}$ ), and underpressured with respect to the turbulent plasma but probably not related to the X-ray chimneys (Ponti et al., 2019) and radio bubbles (Heywood et al., 2019) due to their enormous difference in length (the total major-axis length of the X-ray chimneys and radio bubbles is 320 pc and 430 pc, respectively; however, the innermost bubbles is up to 4 kpc in length). The close-up view (right column in Fig. 11.6) of the vertical profiles and slices (Fig. 11.7) demonstrate that there is a sharp pressure jump at the edge of the innermost bubbles at  $z = 3.62$  kpc, indicating that the innermost bubbles are an expanding reverse shock. The high-density upstream of the reverse shock requires an even higher density downstream. Continuing outward, there exists a dense shell before the gas density drops to values further downstream. The turbulent plasma is therefore bracketed between the downstream of reverse shock and of the outermost forward shock, thus heating the turbulent plasma up considerably.

We stress that either the outermost shock, turbulent plasma, or innermost bubbles are symmetric about the Galactic plane despite that the jets are tilted to the disk normal at an angle of 45°.

In addition to the fiducial run, in Fig. 11.5 we also show the slices of various gas properties at  $t = 12.39$  Myr in different Galactic environments. We compare the clumpy disk (Fig. 11.1) with the smooth disk in a stratified atmosphere (Fig. 11.2; the initial density profile is shown in Fig. 10.1). The results show that the clumpiness of the dense disk has an insignificant effect on the overall dynamics of bubbles. However, the outermost bubbles arising from the smooth disk in a uniform atmosphere (Fig. 11.3) is quasi-spherical, suggesting that the stratification facilitates the elongation of the outermost bubbles significantly. Fig. 11.3 and 11.4 reveal that the development of the innermost bubbles is always associated with the disk. Also, without the disk (Fig. 11.4), the

outermost bubbles and the turbulent plasma would be oblique, indicating that the dense disk is crucial for the production of symmetric Galactic bubbles.

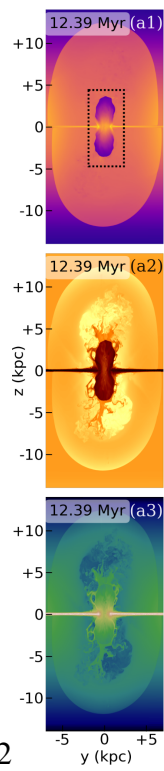
## 11.2 Morphology and Profiles in X-ray

The X-ray emissivity is computed for each computational cell using the MEKAL model (Mewe et al., 1985; Kaastra & Mewe, 1993; Liedahl et al., 1995) implemented in the utility XSPEC (Arnaud, 1996), assuming solar metallicity. The X-ray intensity map is then generated by projecting the emissivities along lines of sight pointing away from the solar position at  $(R_\odot, 0, 0) = (8, 0, 0)$  kpc with angular resolutions of 0.5 degrees, where  $R_\odot$  is the Sun-GC distance.

We point out that the projections used throughout this paper are ‘perspective’, which has the effect of making a distant object appear smaller than the same object in a closer distance, in order to facilitate a reliable interpretation of simulated all-sky map. Also, the observed X-ray emission is contributed by all the gas in the Milky Way halo, which likely extends to a radius of  $\sim 250$  kpc (Blitz & Robishaw, 2000; Grcevich & Putman, 2009), much bigger than our simulation box. Therefore, we first compute the X-ray emissivity from the simulated gas within a radius of 25 kpc away from the GC. Then, beyond 25 kpc the gas is assumed to be isothermal with  $T = 10^6$  K and follows the observed density profile of (Tepper-García et al., 2015) out to a radius of 250 kpc.

Fig. 11.8 shows the comparison between the simulated (top) and observed (bottom) all-sky map in the range 0.6–1.0 keV. In the simulated map, the red arrow at the center represents the direction of the bipolar jets, constantly ejecting at an angle of  $45^\circ$  to the disk normal between 0–1.2 Myr. Fig. 11.9 displays the simulated X-ray photon count rates as a function of Galactic longitudes (red) in the same energy band as in Fig. 11.8 cut at various Galactic latitudes (as labelled), compared with the observed profiles (black).

First, as shown in Fig. 11.1, the half-width of the outermost bubbles is around 7 kpc, corresponding to an half angular width  $\sin^{-1}(7 \text{ kpc}/R_\odot) \sim 122^\circ$ , which is as wide as the eROSITA bubbles in the simulated X-ray map (top panel in Fig. 11.8). We therefore suggest that the eROSITA bubble shells are a signature of compressed forward shocks that



[subfigure]labelformat=simple 0.2

(a)  
b

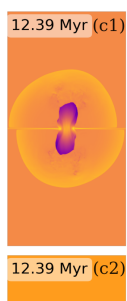
Figure 11.1:



0.2

(a)  
b

Figure 11.2:



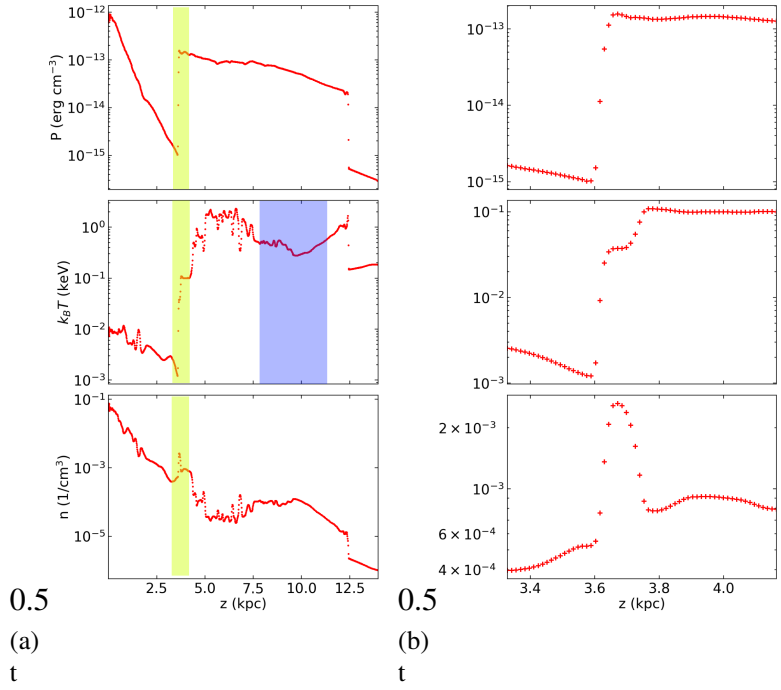


Figure 11.6: Left: the profiles of pressure (top), temperature (middle), and number density (bottom) along the positive  $z$ -axis in Fig. 11.5. Right: the close-up view of the profiles in the yellow band. The sharp pressure jump at  $z = 3.62$  kpc indicates that the innermost bubbles (dashed box in the top panel in Fig. 11.1) are an expanding reverse shock.

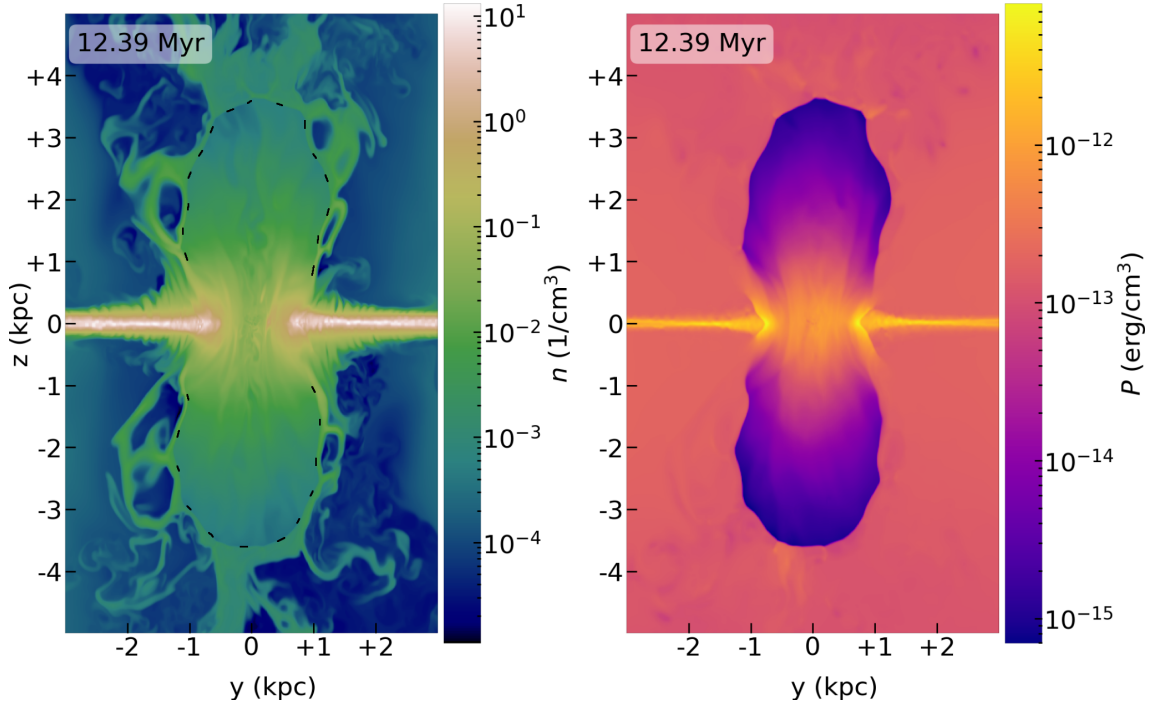


Figure 11.7: Zoom-in images of the density (left) and pressure (right) slices of the innermost bubbles. The high density upstream of the reverse shock requires an even higher density downstream. Continuing outward, the higher density must match with low density further downstream; thus there exists a dense shell (the turbulent region outside the black dashed line in the left panel).

have been driven into the northern and the southern Galactic halo, as previously proposed by Predehl et al. (2020) and Yang et al. (2022). The broad agreement between simulated and observed X-ray maps hints that the full vertical extent of the eROSITA bubbles can be properly formed by an oblique jet within a thin disk of dense ISM.

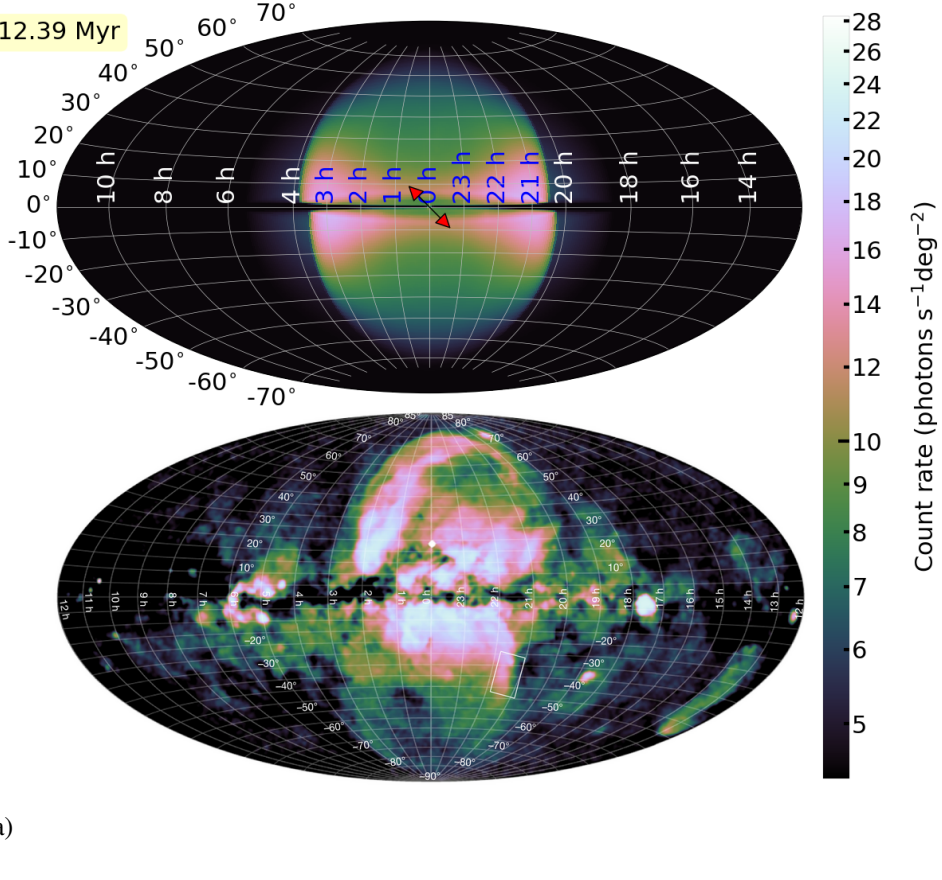
Second, we observe that the simulated eROSITA bubbles are not as limb-brightened as the observation. A possibility to enhance the X-ray emission is to include shock-accelerated CRs near the shock, in which CRs could increase the compressibility of the fluid, resulting in the enhanced thermal Bremsstrahlung emissivity that is proportional to density squared. Also, the disagreement of the northeastern bubble is expected as the North Polar Spur, which is a giant ridge of bright X-ray emission that rises roughly perpendicularly out of the plane of the galaxy, might be a superposition of the GC structure and a remnant of the local supernova (Berkhuijsen et al., 1971; Das et al., 2020; Panopoulou et al., 2021), which is not included in our simulations, whereas analyses based on X-ray data tend to suggest a GC origin (Kataoka et al., 2018b; Sofue, 2000; LaRocca et al., 2020).

Third, the innermost bubbles shown in Fig. 11.5, even though with high column density, are invisible in the simulated X-ray map as the temperature of the innermost bubbles is around 1–10 eV (see the temperature profile in Fig. 11.6). Consequently, the X-ray emission within the innermost bubbles is severely suppressed by the cutoff  $\exp[-h\nu/k_B T]$  in the thermal Bremsstrahlung emissivity. This is the reason why the innermost bubbles are unseen in the X-ray observation.

### 11.3 Gamma-ray and microwave spectra: constraint on the CRe spectral index

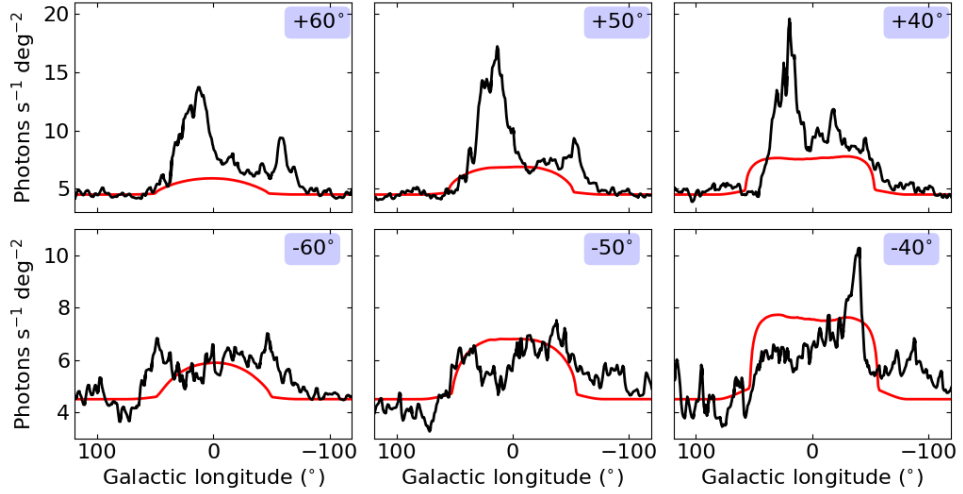
In this section, we obtain the constraint on the CRe spectral index by comparing the simulated gamma-ray and microwave spectra with the observed spectra of the Fermi bubbles (Ackermann et al., 2014) and the microwave haze (Dobler & Finkbeiner, 2008), respectively.

We assume the leptonic model for the gamma-ray and microwave emission as previous



(a)  
t

Figure 11.8: Simulated (top) and observed (bottom; Predehl et al. 2020) count rate ( $\text{photons s}^{-1} \text{deg}^{-2}$ ) in the 0.6–1.0 keV range. Throughout this paper we show sky maps in Galactic coordinates centered on the Galactic center using a Hammer-Aitoff projection. The red arrow at the center of the top panel depicts the direction of the bipolar jets, constantly ejecting at an angle of  $45^\circ$  to the disk normal for the first 1.2 Myr.



(a)  
t

Figure 11.9: Comparison of the simulated (red) and observed (black; Predehl et al. 2020) one-dimensional photon count-rate profiles in the same energy band as in Fig. 11.8, cut at various Galactic latitudes (as labelled).

Figure 11.10:

studies have shown that the bubble and haze spectra can be simultaneously produced by the same population of CRe (Su et al., 2010; Ackermann et al., 2014; Yang et al., 2022). In the leptonic scenario, the gamma-ray and microwave emission come from IC scattering of the ISRF and synchrotron radiation, respectively. Because the evolution of CR spectrum is not modelled in the simulations, we assume that the CRe spectrum is spatially uniform and follows a power-law distribution ranging from 0.5 MeV ( $\sim m_e c^2$ ) to 562.1 GeV. The choice of 562.1 GeV is motivated by the observed cutoff gamma-ray energy shown in Fig. 11.11 as most of the CRe energy is carried away by the up-scattered photons in the Klein-Nishina limit.

The IC emissivity of the upscattered photons at the energy  $\epsilon_1$  is computed for each computational cell in our simulations using the Klein-Nishina IC cross-section (Jones, 1968; Blumenthal & Gould, 1970) to handle the scattering between ultra-relativistic CRe and photons in the ISRF:

$$\frac{dE}{dtd\epsilon_1 dV} = \frac{3}{4}\sigma_T c \mathbb{C}\epsilon_1 \int_{\epsilon_{\min}}^{\epsilon_{\max}} \frac{n(\epsilon)}{\epsilon} d\epsilon \int_{\gamma_{e,\min}(\epsilon)}^{\gamma_{e,\max}} \gamma_e^{-(p+2)} f(q, \Gamma) d\gamma_e, \quad (11.1a)$$

$$f(q, \Gamma) = 2q \ln q + (1+2q)(1-q) + 0.5(1-q) \frac{(\Gamma q)^2}{1+\Gamma q}, \quad (11.1b)$$

$$q = \frac{\epsilon_1/\gamma_e m_e c^2}{\Gamma(1 - \epsilon_1/\gamma_e m_e c^2)}, \quad (11.1c)$$

$$\Gamma = \frac{4\epsilon\gamma_e}{m_e c^2}, \quad (11.1d)$$

$$\gamma_{e,\min}(\epsilon) = 0.5 \left( \frac{\epsilon_1}{m_e c^2} + \sqrt{\left( \frac{\epsilon_1}{m_e c^2} \right)^2 + \frac{\epsilon_1}{\epsilon}} \right), \quad (11.1e)$$

where  $\sigma_T$  is the Thomson cross section,  $c$  is the speed of light,  $m_e$  is the electron mass,  $n(\epsilon)$  is the energy distribution of the photon number density in the ISRF given by Porter

et al. (2017),  $\gamma_e$  is the Lorentz factor of CRe, and  $\mathbb{C}$  and  $p$  are the normalization constant and spectral index of the CRe power-law spectrum.  $\gamma_{e,\min}(\epsilon)$  is the minimum Lorentz factor of CRe that allows the incident photons to be scattered from energy  $\epsilon$  to  $\epsilon_1$ , and  $\gamma_{e,\max}$  is the maximum CRe Lorentz factor in the spectrum. To obtain the simulated IC emissivities, we perform the double integration in Eq. 11.1 on each cell over the range of the CRe Lorentz factor and the range of incident photon energy between  $\epsilon_{\min} = 1.13 \times 10^{-4}$  eV (cosmic microwave background) and  $\epsilon_{\max} = 13.59$  eV (optical starlight).

The synchrotron emissivity with an isotropic electron pitch angle distribution is given by Blumenthal & Gould (1970):

$$\frac{dE}{dtd\nu dV} = \frac{4\pi\mathbb{C}e^3B^{0.5(p+1)}}{m_ec^2} \left( \frac{3e}{4\pi m_ec} \right)^{0.5(p-1)} a(p)\nu^{-0.5(p-1)}, \quad (11.2a)$$

$$a(p) = \frac{2^{0.5(p-1)}\sqrt{3}\Gamma[(3p-1)/12]\Gamma[(3p+9)/12]\Gamma[(p+5)/4]}{8\sqrt{\pi}(p+1)\Gamma[(p+7)/4]}, \quad (11.2b)$$

where  $\Gamma$  is the gamma function, and  $B$  is the magnetic field strength defined in Eq. 10.5. For a given longitude and latitude range, the simulated spectra are computed by projecting emissivities as we project X-ray emissivities in Section 11.2, and then we average the spectra over all the sight lines within the region on the sky.

Fig. 11.11 shows the simulated microwave (left) and gamma-ray (right) spectra averaged over the different patches (shown in the legends) of the sky. The rows from top to bottom show the spectra with different assumptions of the CRe spectral index, 2.2, 2.4 and 2.6. We highlight our findings as follows.

First, we find that, among the three values of the CR spectral indices assumed, a CRe spectral index of 2.4 (the middle row) provides the best fits for both the the simulated gamma-ray spectra as well as the microwave spectra. This value is slightly steeper than the best-fit spectral index of  $\sim 2.17$  found by Ackermann et al. (2014). However, we note

that our calculation takes into account the 3D variations of the ISRF, whereas the previous constraint was based on the ISRF at a fixed height of 5 kpc away from the Galactic plane.

Second, the simulated gamma-ray spectra are nearly latitude independent. Note that we have assumed spatially uniform spectrum for the underlying CRe, and hence the simulated gamma-ray spectra at different latitudes mainly reflect how the 3D distribution of the simulated CR number density (see Fig. 11.13) is projected into different latitude bins. Overall we find good agreement between the simulated and observed spectra (Ackermann et al., 2014); only the simulated spectrum at high latitudes tends to be slightly dimmer than the lower-latitude spectrum because the optical intensity in the ISRF decays with increasing latitudes.

Third, our assumed range for the CRe spectrum (0.5 MeV to 562.1 GeV) produces gamma-ray spectra with a high-energy cutoff around energies 400–500 GeV, consistent with the observed cutoff energy. This is expected since the upscattered high-energy photons ( $\epsilon_1 \sim 450$  GeV) mainly arise from the scattering between the relativistic CRe ( $\gtrapprox 408$  GeV) and optical starlight ( $\epsilon \sim 10$  eV). Thus, Eq. 11.1e can be reduced to  $\epsilon_1 \sim \gamma m_e c^2$  in the Klein–Nishina limit (i.e.  $\epsilon_1 \epsilon \gg (m_e c^2)^2$ ), implying most of the CRe energy is carried away by the upscattered photons.

Finally, the good agreement between the simulated and observed gamma-ray/microwave spectra implies that, in the presence of ISRF and magnetic fields, the emission of the Fermi bubbles and the microwave haze can be produced by the same high-energy electrons via IC scattering and synchrotron radiation, respectively. Our results thus provide further support for the leptonic model as previously suggested (Su et al., 2010; Ackermann et al., 2014; Yang et al., 2013, 2022).

Fig. 11.12 shows the simulated gamma-ray photon flux with a CRe power-law index 2.4 compared with the observed one in the energy bin 76.8 – 153.6 GeV. As the eROSITA bubbles, one can see that the symmetric *Fermi* bubbles can also be realized by oblique jets. The extent of the simulated gamma-ray bubbles is also comparable to the observed ones. However, we find that the simulated bubble surface is not as smooth as the observed bubbles. The instabilities at the bubble surface may be suppressed by the magnetic

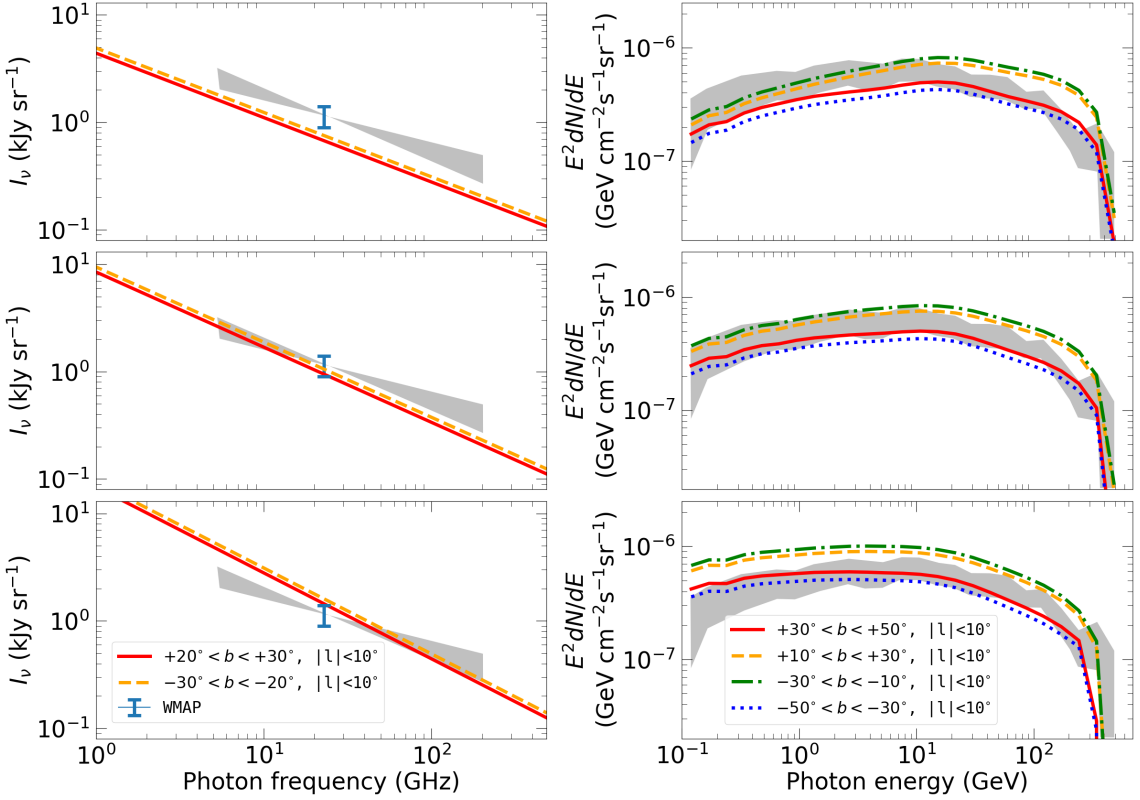


Figure 11.11: Simulated microwave spectra (colored lines in left) averaged over  $20^\circ < |b| < 30^\circ$ ,  $|l| < 10^\circ$ . The data point represents the *WMAP* data in the 23 GHz K band and the shaded bow-tie area indicates the range of synchrotron spectral indices allowed for the *WMAP* haze (Dobler & Finkbeiner, 2008). Simulated gamma-ray spectra (colored lines in right column) of the *Fermi* bubbles calculated for a longitude range of  $|l| < 10^\circ$  for different latitude bins. The gray band represents the observational data of Ackermann et al. (2014). The row from top to bottom shows the microwave (left) and gamma-ray (right) spectra with CRe spectral index 2.2, 2.4 and 2.6, respectively. The CRe cutoff energy is 562.1 GeV in all cases.

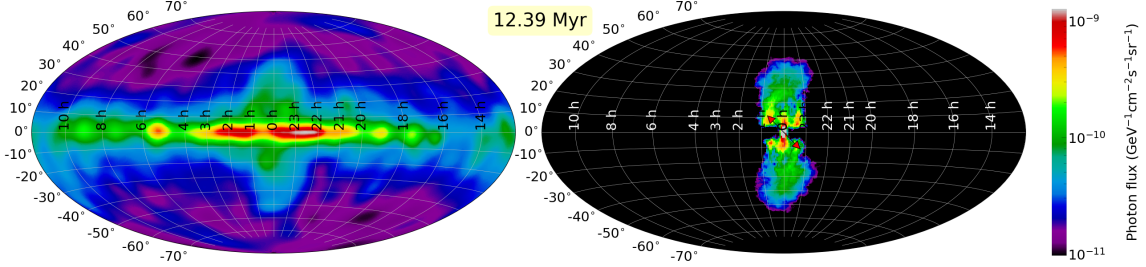


Figure 11.12: The observed (left; Selig et al. 2015) and simulated (right) photon flux in the energy bin  $76.8 - 153.6$  GeV. Note that the left panel is the photon flux of the diffuse component reconstructed by the D<sup>3</sup>PO algorithm (Selig et al., 2015) that analyzes the photon data from the *Fermi* Large Area Telescope (Atwood et al., 2009) and removes the contribution from point-like component. The red arrow at the center of the right panel depicts the direction of the bipolar jet, constantly ejecting at an angle of  $45^\circ$  to the disk normal in 1.2 Myr.

draping effect (Lyutikov, 2006; Yang et al., 2012) if magnetic fields were included in the simulations. With magnetic draping, the sharp edges of the observed bubbles (Su et al., 2010; Ackermann et al., 2014) could also be explained by anisotropic CR diffusion along field lines (Yang et al., 2013).

The simulated gamma-ray intensity distribution is shown in Fig. 11.12. Though the overall size of the simulated gamma-ray bubbles is comparable to that of the observed ones, the gamma-ray intensity does not appear to be as uniform as originally found in Su & Finkbeiner (2012). As discussed above, the gamma-ray intensity is slightly higher close to the Galactic plane due to the stronger radiation field at lower latitudes. However, this level of brightness variations appears to be consistent with the later observational data of Ackermann et al. (2014) and Selig et al. (2015), which shows that there are some substructures in the gamma-ray intensity distribution within the bubbles.

For completeness, we show the simulated CR energy density at 12.39 Myr in Fig. 11.13. The comparison between Fig. 11.5 and Fig. 11.13 shows that the CR pressure is around  $5 \times 10^{-15} - 8 \times 10^{-15}$  erg cm<sup>-3</sup>, bringing the CR-to-gas pressure ratio is 0.1–0.2, similar to 0.18 at the beginning of the simulation. We therefore stress that ignoring the contribution of CR pressure gradient to the momentum of the gas in Eq. 10.1 is reasonable.

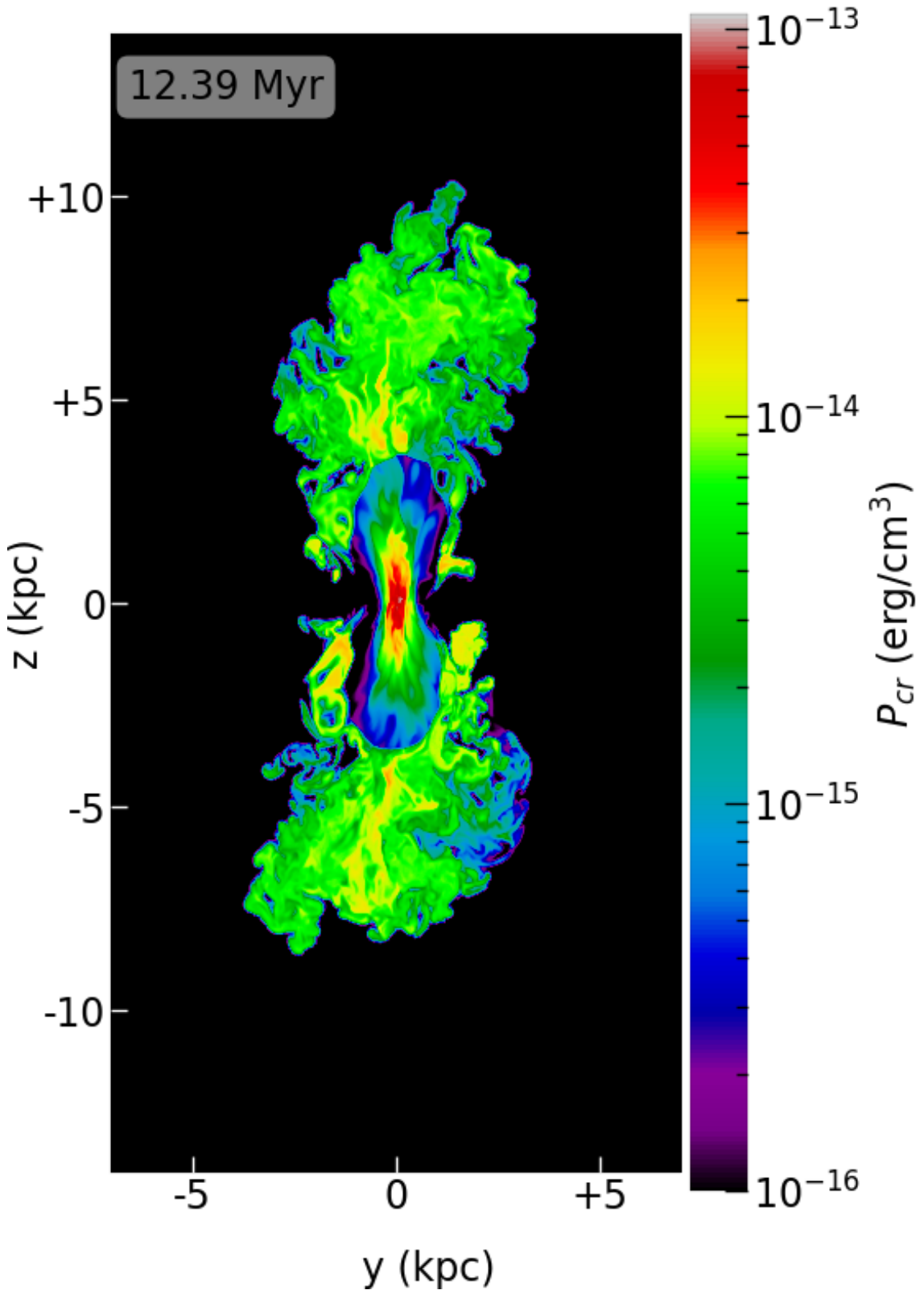


Figure 11.13: The CR pressure slice passing through the jet source at 12.39 Myr. Comparison between gas pressure (Fig. 11.5) and cosmic ray pressure shows that the CR pressure is around  $5 \times 10^{-15}$ – $8 \times 10^{-15}$  erg/cm<sup>3</sup>, bringing the CR-to-gas pressure ratio is 0.1–0.2, similar to 0.18 at the beginning of the simulation. We therefore stress that ignoring the contribution of CR pressure gradient to the momentum of the gas in Eq. 10.1 is reasonable.



# Chapter 12

## Discussion

As a past violent event at the GC must destroy the Central Molecular Zone (CMZ) but the CMZ is currently either in a quasi-steady state or presently increasing (Crocker, 2012; Krumholz & Kruijssen, 2015; Sormani & Barnes, 2019); we conclude that the time since the violent event must be “slightly” shorter than the reconstruction time of CMZ on a timescale of  $M_{\text{CMZ}}/\dot{M}_{\text{inflow}}$ , where  $M_{\text{CMZ}}$  is the total mass of molecular gas within  $R \sim 300$  pc, and  $\dot{M}_{\text{inflow}}$  is the gas inflow rate from the Galactic disc at  $R \sim 3$  kpc down to the outskirts of the CMZ. Since  $M_{\text{CMZ}}$  and  $\dot{M}_{\text{inflow}}$  have been reported to be in the range  $2 - 6 \times 10^7 M_\odot$  (Dahmén et al., 1998; Ferrière et al., 2007) and  $0.4 - 2.7 M_\odot \text{ yr}^{-1}$  (Crocker, 2012; Sormani & Barnes, 2019), respectively; we estimate that the CMZ formation is about a couple of 10 Myrs, similar to 12 Myr required for our simulated bubbles to reach the desired morphology.

On the other hand, our modeled gamma-ray and microwave spectra assumed that the underlying CRe spectrum is spatially uniform with hard spectral index 2.4; however, the high energy CRe severely suffer from synchrotron and IC losses, during their passage through the magnetic and radiation fields, respectively, within the Galaxy.

The typical synchrotron and IC cooling time scale of high energy ( $\sim 100$  GeV) CRe in Milky Way is  $\sim 1$  Myr (Yang & Ruszkowski, 2017), ten times shorter than 12 Myr suggested by our simulation. Therefore, the CRe generating the gamma-ray emission would need to be re-accelerated by in-situ acceleration mechanisms such as shocks or turbulence. Since the forward shock is rather far away from the gamma-ray bubbles, re-

acceleration is more likely associated with turbulence (Mertsch & Sarkar, 2011; Mertsch & Petrosian, 2019), possibly in balance with the IC and synchrotron cooling. We will investigate the competition between stochastic acceleration and radiative cooling in future work.

Overall, our results imply that in the oblique-jet scenario, whatever the true re-acceleration and cooling mechanisms are, the CRe spectrum at the present time has to be spatially uniform with a spectral index of 2.4 in order to fit the observed spectra.

# Chapter 13

## Conclusions for part 2

In this work, we introduce a thin, dense disk composed of clumpy ISM to stall and thermalize the oblique jets for an outburst event from the central SMBH in the Milky Way Galaxy 12 Myrs ago. We investigate the properties of the Galactic bubbles and the microwave haze using 3D SRHD simulations of CR jet injections from the SMBH assuming the leptonic model. The important findings are summarized as follows.

- The development of the expanding forward-reverse shock pair is always associated with the dense disk. In the absence of the disk, the reverse shock is absent, indicating the inclusion of the disk is critical for forming the innermost bubbles.
- The forward-reverse shock pair heats the turbulent plasma considerably ( $\sim 2$  keV). There exists a dense shell immediately downstream of the reverse shock, a situation reminiscent of a supernova shell.
- eROSITA bubbles coincide with the forward shock front originally driven by short-lived bipolar jets for a duration of 1.2 Myr, where the bubbles later significantly expanded into the stratified atmosphere to reach the present 12kpc height. The overall extent of the simulated X-ray bubbles is comparable to that of the eROSITA bubbles, though not as limb-brightened. Future models including shock-accelerated CRs may help to resolve this issue by increasing the compressibility of the fluid and enhancing the thermal Bremsstrahlung emissivity at the edge of the X-ray bubbles.

- Downstream of the reverse shock is filled with hot ( $\sim 2$  keV) and highly turbulent plasma brought from the disk. The interface between the downstream materials of reverse and forward shocks lies a contact discontinuity, which defines the edge of the Fermi bubble. The surface of the simulated bubbles is not as smooth as the observed ones; inclusion of magnetic fields in the future may help suppress the instabilities at the bubble surface due to the mangetic draping effect.
- Assuming a power-law CRe energy spectrum ranging from 0.5 MeV to 560 GeV, where the spectrum is space-independent, we showed that the observed gamma-ray and microwave spectra can simultaneously reproduced. The best-fit CRe power-law index is found to be 2.4.
- The elapsed time of 12 Myr is required for the simulated bubbles to reach the desired morphology. This time scale is appropriate for the observed Central Molecular Zone, 200 pc in radius surrounding the GC, to form. However, it is 10 times longer than the typical synchrotron and IC cooling time scale of high energy ( $\sim 100$  GeV) CRe. Thus, re-acceleration of CRe by shocks or turbulence must be considered in this model. Since the forward shock is rather far away from the gamma-ray bubbles, stochastic acceleration of CRs by turbulence appears to be more plausible. We will investigate the competition between stochastic acceleration and radiative cooling in a future work.
- The Galactic bubbles are observed nearly symmetric about the Galactic plane albeit the bipolar jets are oblique with respect to the disk normal. We showed that inclusion of the dense ISM disk (regardless of its clumpiness) is an essential ingredient for producing the symmetric Galactic bubbles when the jets are oblique. The broad agreement between the simulated and observed multi-wavelength features demonstrates that oblique failed jets are a plausible scenario for the formation of the Galactic bubbles, which relieve the caveat of earlier jet models where jets need to be vertical.

# Chapter 14

## Appendix for part 2

It is instructive to compare the simulation results (Fig. 14.1) using exactly same parameters except for the density ( $\rho$ ), temperature ( $k_B T$ ), and four-velocity ( $\beta\gamma$ ) within the jet source. The parameters of jet source, including the fiducial run (C), covered in this appendix are given in Table 14.1.

We observe that either higher density (F→C→E) or higher velocity (G→C→A) of the source can enhance the intensity of the shocks driven into the atmosphere, and makes the post-shock region hotter, as well as leads the bubbles to be more asymmetric about the GC. This is because the denser/faster jets are more likely to break through the thin disk in a short time, so that the jets have insufficient time to interact with the disk to change their orientations and then be vertically elongated by the stratified atmosphere.

Finally, we find that increasing the source temperature (B→C→D) not only improves the symmetry of the bubbles but also increases the temperature inside the bubbles at the present time. This result implies that a high-temperature source helps the jets ablate the clumpy dense gas away and pours into the atmosphere through the intercloud channels of the clumpy disk. In contrast, if source temperature is not high enough, the jets cannot effectively ablate the high-density clouds within 12 Myr, resulting in the formation of asymmetric bubbles (case B).

Table 14.1: The list of runs showing different injected jet parameters. The fiducial run (C) has been pointed out by an asterisk in the list.

	A	B	C*	D	E	F	G
$k_B T$ (MeV)	1.720	0.034	1.720	86.100	1.720	1.720	1.720
$\rho$ (g/cm <sup>3</sup> )	$10^{-26}$	$10^{-26}$	$10^{-26}$	$10^{-26}$	$10^{-25}$	$10^{-27}$	$10^{-26}$
$\beta\gamma$	1.20	0.60	0.60	0.60	0.60	0.60	0.3

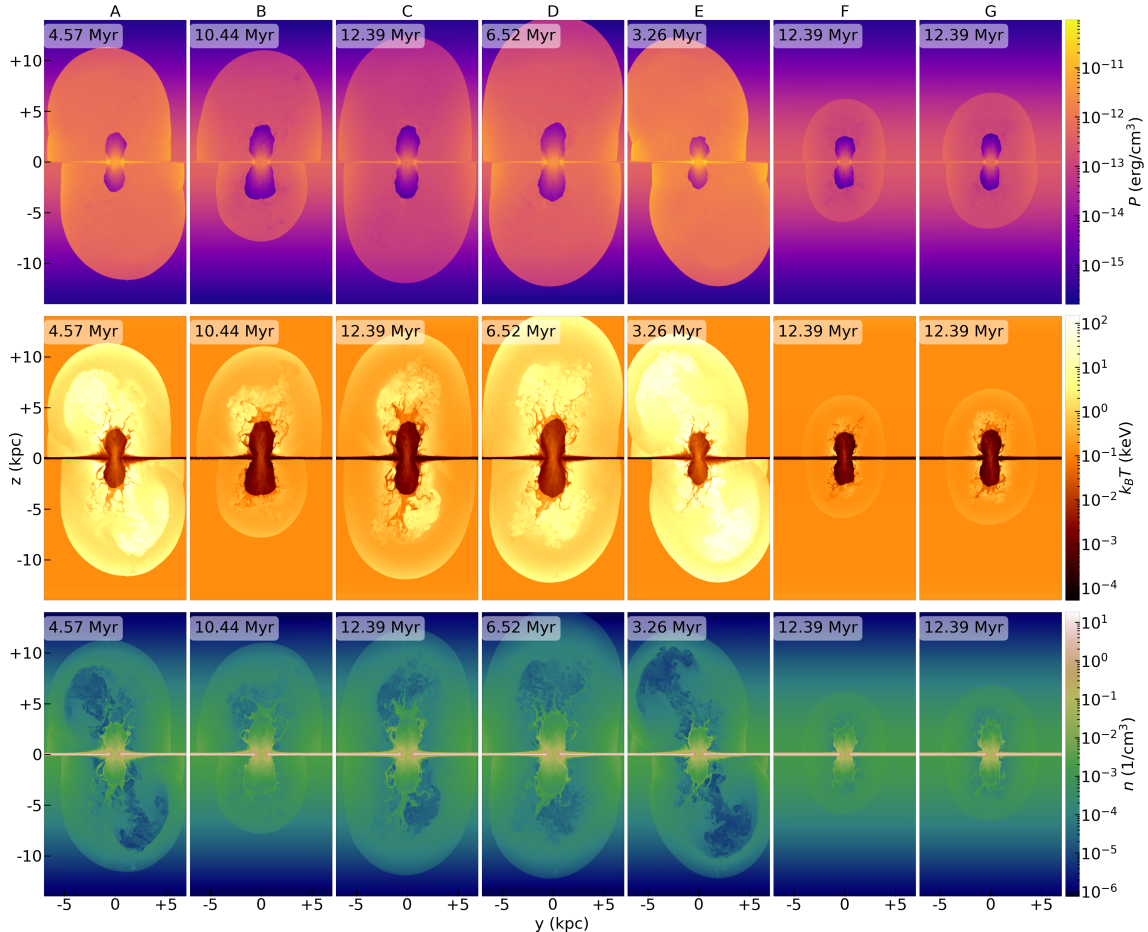


Figure 14.1: Simulation results based on the jets parameters in Table. 14.1.

# Bibliography

Ackermann M., et al., 2014, The Astrophysical Journal, 793, 64

Ade P. A. R., et al., 2013, Astronomy & Astrophysics, 554, A139

Arnaud K. A., 1996, in Jacoby G. H., Barnes J., eds, Astronomical Society of the Pacific Conference Series Vol. 101, Astronomical Data Analysis Software and Systems V. p. 17

Asada K., Nakamura M., 2012, The Astrophysical Journal, 745, L28

Atwood W. B., et al., 2009, The Astrophysical Journal, 697, 1071

Berkhuijsen E. M., Haslam C., Salter C., 1971, Astronomy and Astrophysics, 14, 252

Blandford R. D., Payne D. G., 1982, Monthly Notices of the Royal Astronomical Society, 199, 883

Blandford R., Meier D., Readhead A., 2019, Annual Review of Astronomy and Astrophysics, 57, 467

Blitz L., Robishaw T., 2000, ] 10.1086/309457, 541, 675

Blumenthal G. R., Gould R. J., 1970, Reviews of Modern Physics, 42, 237

Boccardi B., Krichbaum T. P., Bach U., Mertens F., Ros E., Alef W., Zensus J. A., 2015, A and A, 585, A33

Carretti E., et al., 2013, Nature, 493, 66

Cecil G., Bland-Hawthorn J., Veilleux S., Filippenko A. V., 2001, The Astrophysical Journal, 555, 338

- Chiueh T., 1989, Phys. Rev. Lett., 63, 113
- Chiueh T., Li Z.-Y., Begelman M. C., 1991, , 377, 462
- Chiueh T., Li Z.-Y., Begelman M. C., 1998, The Astrophysical Journal, 505, 835
- Crocker R. M., 2012, Monthly Notices of the Royal Astronomical Society, 423, 3512
- Crocker R. M., Aharonian F., 2011, Phys. Rev. Lett., 106, 101102
- Crocker R. M., Jones D. I., Melia F., Ott J., Protheroe R. J., 2010, Nature, 463, 65
- Crocker R. M., Bicknell G. V., Taylor A. M., Carretti E., 2015, , 808, 107
- Dahmén G., et al., 1998, <http://dx.doi.org/10.1051/aas:1997389>
- Das K. K., Zucker C., Speagle J. S., Goodman A., Green G. M., Alves J., 2020, Monthly Notices of the Royal Astronomical Society, 498, 5863
- Dobler G., Finkbeiner D. P., 2008, The Astrophysical Journal, 680, 1222
- Dopita M. A., et al., 2015, The Astrophysical Journal Supplement Series, 217, 12
- Falle S. A. E. G., 1991, Monthly Notices of the Royal Astronomical Society, 250, 581
- Federrath C., Roman-Duval J., Klessen R. S., Schmidt W., Low M.-M. M., 2010, Astronomy and Astrophysics, 512, A81
- Ferrière K. M., 2001, Rev. Mod. Phys., 73, 1031
- Ferrière K., Gillard W., Jean P., 2007, Astronomy and Astrophysics, 467, 611
- Fong W., et al., 2019, , 883, L1
- Fryxell B., et al., 2000, The Astrophysical Journal Supplement Series, 131, 273
- Gallimore J. F., Axon D. J., O'Dea C. P., Baum S. A., Pedlar A., 2006, The Astronomical Journal, 132, 546
- Ghirlanda G., et al., 2019, Science, 363, 968

- Giovannini G., et al., 2018, *Nature Astronomy*, 2, 472
- Giroletti M., et al., 2004, *The Astrophysical Journal*, 600, 127
- Gourgouliatos K. N., Komissarov S. S., 2017, *Nature Astronomy*, 2, 167
- Grcevich J., Putman M. E., 2009, ] 10.1088/0004-637x/696/1/385, 696, 385
- Guo F., Mathews W. G., 2012, *The Astrophysical Journal*, 756, 181
- Guo F., Mathews W. G., Dobler G., Oh S. P., 2012, , 756, 182
- Heywood I., et al., 2019, *Nature*, 573, 235
- Higham N. J., 2002, *Accuracy and Stability of Numerical Algorithms*, 2nd edn. Society for Industrial and Applied Mathematics, USA
- Johnston K. V., Spergel D. N., Hernquist L., 1995, *The Astrophysical Journal*, 451, 598
- Jones F. C., 1968, *Physical Review*, 167, 1159
- Jüttner F., 1911, *Annalen der Physik*, 339, 856
- Kaastra J. S., Mewe R., 1993, , 97, 443
- Kataoka J., Sofue Y., Inoue Y., Akita M., Nakashima S., Totani T., 2018a, *Galaxies*, 6, 27
- Kataoka J., Sofue Y., Inoue Y., Akita M., Nakashima S., Totani T., 2018b, *Galaxies*, 6, 27
- Kennel C. F., Coroniti F. V., 1984a, , 283, 694
- Kennel C. F., Coroniti F. V., 1984b, , 283, 710
- Kim J.-Y., et al., 2018, *A&A*, 616
- Krumholz M. R., Kruijssen J. M. D., 2015, *Monthly Notices of the Royal Astronomical Society*, 453, 739
- LaRocca D. M., Kaaret P., Kuntz K., Hodges-Kluck E., Zajczyk A., Bluem J., Ringuette R., Jahoda K. M., 2020, *The Astrophysical Journal*, 904, 54

- Lewis G. M., Austin P. H., 2002, 1th Conference on AtmosphericRadiation
- Li Z.-Y., Chiueh T., Begelman M. C., 1992, , 394, 459
- Li Z., Morris M. R., Baganoff F. K., 2013, , 779, 154
- Liedahl D. A., Osterheld A. L., Goldstein W. H., 1995, , 438, L115
- Lora-Clavijo F. D., Cruz-Osorio A., Guzmán F. S., 2015, The Astrophysical Journal Supplement Series, 218, 24
- Lyutikov M., 2006, Monthly Notices of the Royal Astronomical Society, 367, 1594
- Martí J. M., Müller E., 1994, Journal of Fluid Mechanics, 258, 317
- Mathews W. G., 1971, , 165, 147
- Mertsch P., Petrosian V., 2019, Astronomy & Astrophysics, 622, A203
- Mertsch P., Sarkar S., 2011, Phys. Rev. Lett., 107, 091101
- Mewe R., Gronenschild E. H. B. M., van den Oord G. H. J., 1985, , 62, 197
- Mignone A., Bodo G., 2005, Monthly Notices of the Royal Astronomical Society, 364, 126
- Mignone A., Bodo G., 2006, Monthly Notices of the Royal Astronomical Society, 368, 1040
- Mignone A., McKinney J. C., 2007, Monthly Notices of the Royal Astronomical Society, 378, 1118
- Mignone A., Plewa T., Bodo G., 2005, The Astrophysical Journal Supplement Series, 160
- Miller M. J., Bregman J. N., 2013, The Astrophysical Journal, 770, 118
- Miller M. J., Bregman J. N., 2016, The Astrophysical Journal, 829, 9
- Mooley K. P., et al., 2018a, , 554, 207

- Mooley K. P., et al., 2018b, , 561, 355
- Morganti R., Oosterloo T., Oonk J. B. R., Frieswijk W., Tadhunter C., 2015, *Astronomy & Astrophysics*, 580, A1
- Mou G., Yuan F., Bu D., Sun M., Su M., 2014, , 790, 109
- Nagai H., et al., 2014, *The Astrophysical Journal*, 785, 53
- Narayanan S. A., Slatyer T. R., 2017, *Monthly Notices of the Royal Astronomical Society*, 468, 3051
- Noble S. C., Gammie C. F., McKinney J. C., Zanna L. D., 2006, *The Astrophysical Journal*, 641, 626
- Núñez-de la Rosa J., Munz C.-D., 2016, , 460, 535
- Panopoulou G. V., Dickinson C., Readhead A. C. S., Pearson T. J., Peel M. W., 2021, *The Astrophysical Journal*, 922, 210
- Ponti G., et al., 2019, *Nature*, 567, 347
- Porter T. A., Jóhannesson G., Moskalenko I. V., 2017, *The Astrophysical Journal*, 846, 67
- Predehl P., et al., 2020, *Nature*, 588, 227
- Predehl P., et al., 2021, *Astronomy & Astrophysics*, 647, A1
- Rezzolla L., Zanotti O., 2018, *Relativistic hydrodynamics*. Oxford University Press
- Rezzolla L., Zanotti O., Pons J. A., 2001, *Journal of Fluid Mechanics*, 449, 395
- Ryu D., Chattopadhyay I., Choi E., 2006, *The Astrophysical Journal Supplement Series*, 166, 410
- Sarkar K. C., Nath B. B., Sharma P., 2015, *Monthly Notices of the Royal Astronomical Society*, 453, 3828

Schive H.-Y., Tsai Y.-C., Chiueh T., 2010, The Astrophysical Journal Supplement Series, 186, 457

Schive H.-Y., ZuHone J. A., Goldbaum N. J., Turk M. J., Gaspari M., Cheng C.-Y., 2018, Monthly Notices of the Royal Astronomical Society, 481, 4815

Selig M., Vacca V., Oppermann N., Enßlin T. A., 2015, Astronomy & Astrophysics, 581, A126

Sod G. A., 1978, Journal of Computational Physics, 27, 1

Sofue Y., 2000, The Astrophysical Journal, 540, 224

Sormani M. C., Barnes A. T., 2019, Monthly Notices of the Royal Astronomical Society, 484, 1213

Stone J. M., Tomida K., White C. J., Felker K. G., 2020, The Astrophysical Journal Supplement Series, 249, 4

Strong A. W., Moskalenko I. V., Ptuskin V. S., 2007, Annual Review of Nuclear and Particle Science, 57, 285

Su M., Finkbeiner D. P., 2012, The Astrophysical Journal, 753, 61

Su M., Slatyer T. R., Finkbeiner D. P., 2010, The Astrophysical Journal, 724, 1044

Synge J. L., 1957, North-Holland Pub. Co.; Interscience Publishers

Taub A. H., 1948, Physical Review, 74, 328

Tepper-García T., Bland-Hawthorn J., Sutherland R. S., 2015, The Astrophysical Journal, 813, 94

Toro E. F., 2011, Riemann solvers and numerical methods for fluid dynamics : a practical introduction. Springer, Berlin

Tseng P.-H., Schive H.-Y., Chiueh T., 2021, Monthly Notices of the Royal Astronomical Society, 504, 3298

Turk M. J., Smith B. D., Oishi J. S., Skory S., Skillman S. W., Abel T., Norman M. L.,  
2011, *The Astrophysical Journal Supplement Series*, 192, 9

Valenti E., et al., 2018, , 616, A83

Wagner A. Y., Bicknell G. V., Umemura M., 2012, *The Astrophysical Journal*, 757, 136

Woodward P., Colella P., 1984, *Journal of Computational Physics*, 54, 115

Woosley S. E., 1993, , 405, 273

Yang H.-Y. K., Ruszkowski M., 2017, *The Astrophysical Journal*, 850, 2

Yang H.-Y. K., Ruszkowski M., Ricker P. M., Zweibel E., Lee D., 2012, *The Astrophysical Journal*, 761, 185

Yang H.-Y. K., Ruszkowski M., Zweibel E., 2013, *Monthly Notices of the Royal Astronomical Society*, 436, 2734

Yang H.-Y., Ruszkowski M., Zweibel E., 2018, *Galaxies*, 6, 29

Yang H.-Y. K., Ruszkowski M., Zweibel E. G., 2022, *Nature Astronomy*

Zhang R., Guo F., 2020, *The Astrophysical Journal*, 894, 117

Zhu Z., Li Z., Morris M. R., Zhang S., Liu S., 2019, , 875, 44

Zweibel E. G., 2013, *Physics of Plasmas*, 20, 055501

van Leer B., 1979, *Journal of Computational Physics*, 32, 101

van Leer B., 2006, pp 192–206